Università degli Studi di Ferrara

DOTTORATO DI RICERCA IN SCIENZE DELL'INGEGNERIA

CICLO XXV

COORDINATORE Prof. Stefano Trillo

Geostatistical modelling of PM$_{10}$ mass concentrations with satellite imagery from MODIS sensor

Settore Scientifico Disciplinare ING-INF/03

Dottorando	**Tutore**
Dott. Campalani Piero	Prof. Mazzini Gianluca

_____   _____
(firma)   *(firma)*

Anni 2010/2012

Acknowledgements

A first heartfelt thanks goes to all the people who helped me getting the research activity started, going through it and progressing until the final accomplishment. These are for sure my supervisors — Prof. Gianluca Mazzini, Dr. Simone Mantovani and Prof. Peter Baumann — who made it all possible; all my daily colleagues from MEEO Srl who made it all enjoyable and constructive; my research companion Thi Nhat Thanh Nguyen for the precious discussions and cooperations; Prof. Klaus Schäfer (IMK-IFU) and Dr. Angela Benedetti (ECMWF) for the review and assessment of this thesis; Prof. Edzer Pebesma (IFGI) and Prof. Roger Bivand (NHH) for their superb activity as community mentors inside and outside the R-Sig-Geo world; last and expected, my whole family and friends.

<center>ᕦ·~</center>

Technically speaking, my studies could not be possible without being fed with *data*. Further acknowledgements are due:

Pm Mapper AOT products, for allowing high-resolution aerosols information inputs, which were possible thanks to the various MODIS software development and support teams for the production and distribution of the MODIS data.

Nasa software development and support teams for the production and distribution of the MODIS data.

<center>i</center>

The **Aeronet** teams for collecting, processing, and making available ground-based aerosol observations around the world.

The **Umweltbundesamt** and **Arpa Emilia Romagna** monitoring networks for the provision of PM_{10} ground measurements.

The **Ifs** (Integrated Forecast System) of the **Ecmwf** (European Centre for Medium-Range Weather Forecasts) and **Zamg** (Zentralanstalt für Meteorologie und Geodynamik) for the meteorological maps over Austria.

Contents

List of Figures

List of Tables

Chapter 1

Introduction

The purpose of the research activity carried out in these last three years puts its roots when the Earth Observing Systems (EOS) Terra satellite (originally called EOS-AM-1 because of its morning crossing time through the equator, Levy et al. 2009) was successfully launched in 1999[1] by NASA, and began collecting data on February 24$^{\text{th}}$, 2000. The scientific data retrieved by the instruments onboard this satellite is made available to the public via Web sites and FTP archives then used in several disciplines, including oceanography, biology, and atmospheric modelling.

Several remote sensors were put onboard the Terra satellite and among these, due to its wide spectral range and good spatial resolution, the Moderate-resolution Imaging Spectroradiometer (MODIS) got very popular for research applications in different fields. Amid the long list of MODIS products (see http://modis.gsfc.nasa.gov/data/dataprod/index.php) a strong scientific interest originated from the MOD04 Aerosol Product (somehow surprisingly[2]), and a huge amount of linked publications were written more

---

[1] Its companion – EOS Aqua – will follow in 2002.

[2] "The use of the MODIS aerosol products has far exceeded nearly everyone's imagination." (Levy et al., 2009)
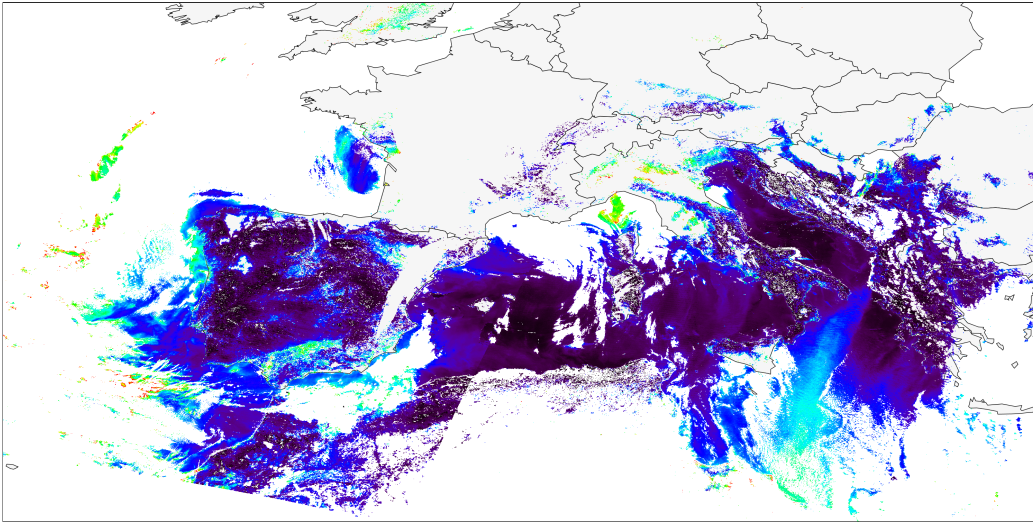
Fig. 1.1 – Example of composite of MODIS-derived AOT observations (granules) on January 29th, 2008.

and more often, as demonstrated by Yoram Janusz Kaufman — Project Scientist for the *Terra* mission, outstanding scientist and Senior Fellow in the NASA Goddard Earth-Sun Exploration Division — in a search on the ISI citation Web site (`climate.gsfc.nasa.gov`).

Regarding the aerosol *validated* (Remer et al., 2005) products of the MODIS sensor (see Fig. 1.1 for an example), they opened a new horizon in the field of atmospheric modelling: the opportunity to deal with *daily* observations of the atmosphere in the form of bidimensional maps, together with the quick development of more and more powerful FOSS GIS systems and software packages for spatial data management and analysis (e.g. Baumann et al. 1998; Bock et al. 2008; Caldeweyher 2011; R Development Core Team 2011), pushed an enthusiastic reaction of the scientific world, seeing in the remote monitoring a practical way to guard several aspects of our Earth, including climate change, radiative budget and, of course, air pollution.

This last task, which is the focus of this thesis, is however very challenging, up to the point that still after more than a decade of research publications, it is unclear when, where and whether the spaceborne aerosol maps are offering a

strong and reliable advantage. This key point has been the drawing power of my studies, which aimed at putting more light on this unanswered question, by evaluating different geostatistical techniques on several datasets which were made available thanks to many private and public research centres (see p.), with different combinations of sources and scales.

This introductory chapter will prepare a ground of knowledge for those who are still unfamiliar with the concepts of remote sensing, particulate matter and aerosol optical thickness. I will be explaining, in a general understandable manner, the main problematics that arise when modelling Air Quality (AQ) concentrations at the ground level by means of spaceborne maps. A final section will describe the current guidelines with regards to the air quality risk assessment and management, with a focus on the current status on the use of models for support to air quality policy in Europe.

1.1   Remote sensing from satellites

Monitoring the Earth with satellites gave rise to an increasing hope in understanding what actually is behind harmful factors like climate warming, rising sea level, deforestation, desertification, ozone depletion, and so on. Satellites would help us assess current state, forecast the future impacts and take proper actions to preserve our planet.

This hope prompted the launch of a plenty of Earth-observing sensors in either the low (LEO), medium (MEO) and geosynchronous (GEO) orbits, totaling up to approximately 900 satellites orbiting above us, as currently tracked NASA (NASA, 2008). Dozens of them are currently in orbit for air quality purposes including the monitoring of sulfur dioxide (SO_2), carbon monoxide (CO), nitrogen dioxide (NO_2) and ozone (O_3).

Some of these sensors have been designed in terms of spatial, spectral and

temporal resolutions for *aerosols* detection, specifically. OMI from Aura Polar Sun-synchronous (PS) satellite (NASA) or SCIAMACHY from Envisat PS satellite (ESA), GOME-2 from METOP PS satellite and MISR from Terra itself are some examples. The unique combination of characteristics offered by MODIS determined its success in the scientific community:

- Terra and Aqua platforms, both hosting a MODIS sensor, follow respectively a descending and ascending polar orbit from a vantage about 700 km above the surface. Although this implies a repeat cycle[3] of 16 days, the MODIS sensor, with its wide view ($\pm 55\,^\circ$) and consequent large swath[4] (around 2330 km), is able to scan almost the whole planet on a daily basis. To better appreciate this, Fig. 1.2 shows the orbit track of Terra. MISR sensor, onboard Terra itself, is also able to retrieve aerosol information with comparable (if not better) quality (Liu et al., 2007b,a) but its temporal resolution up to 9 days inhibits its usage for comprehensive monitoring over an area, and it may rather be used in conjunction with MODIS, which offers more frequent overpasses.

- The spatial resolution of MODIS observations is from 250 to 1000 m at nadir, depending on the spectral channel, allowing for final aerosol retrievals on 10×10 km^2 boxes (the next chapter will clarify the constraints that cause this loss). Though not optimal for small scale analysis, this resolution is still pretty high with respect to other available aerosol products: SCIAMACHY nadir-view products reach a 30×30 km^2 horizontal resolution; GOME-2 80×40 km^2 and OMI 13×25 km^2, for instance (The World Data Center For Remote Sensing Of The Atmosphere, 2002). Moreover, while e.g. OMI aerosol retrievals must assume aerosol layer height, MODIS is not sensitive to it and with its smaller pixel size is less affected by subpixel clouds (Satheesh et al., 2009).

---

[3]The time a satellite spends to cross the same spot on the Earth.
[4]The spatial width of the strip seen by a remote sensor.

- The MODIS scanner has an excellent spectral width and resolution, with 36 channels covering from visible to infrared wavelengths. The aerosol retrieval algorithm makes use of 7 frequency channels and yields thorough estimates of the amounts of aerosols release into the atmosphere (the algorithm of the MOD04 aerosol product will be described in more detail later on).

- As a final crucial factor, MODIS data are made available to the public for free download.

Although the combination of these features revealed to be highly fascinating for scientific studies, still MODIS data might not be enough for a comprehensible daily air monitoring: as for most spaceborne observations of aerosols, especially for passive sensors, the ability to see through clouds is prevented by the scanner wavelengths, while the horizontal resolution is still not optimal.

This last issue is what really concerns the use of the polar-orbiting MODIS retrievals for air monitoring: the regulations, as will be examined in Sec. 1.4, call for specific temporal averages and frequency of occurrence of concentration levels for criteria pollutants. Exceedances estimations would require hourly observations throughout the day, which cannot be derived from MODIS imagery. Geostationary satellites like GOES (Paciorek et al., 2008) or MeteoSat (Popp et al., 2007), provide aerosol products with high temporal resolution and this would allow both the visualization of aerosol fronts movement and the evaluation timing of exceedances. Their view is however fixed and still they don't have the accuracy of aerosol estimation which MODIS has: by 2015, NOAA proposes to launch the GOES-R series of satellites, which will allow retrievals of precise aerosol products every 5—30 min (Hoff and Christopher, 2009) using MODIS-like channels. This might lead to new increased importance of satellites in the air quality monitoring system.
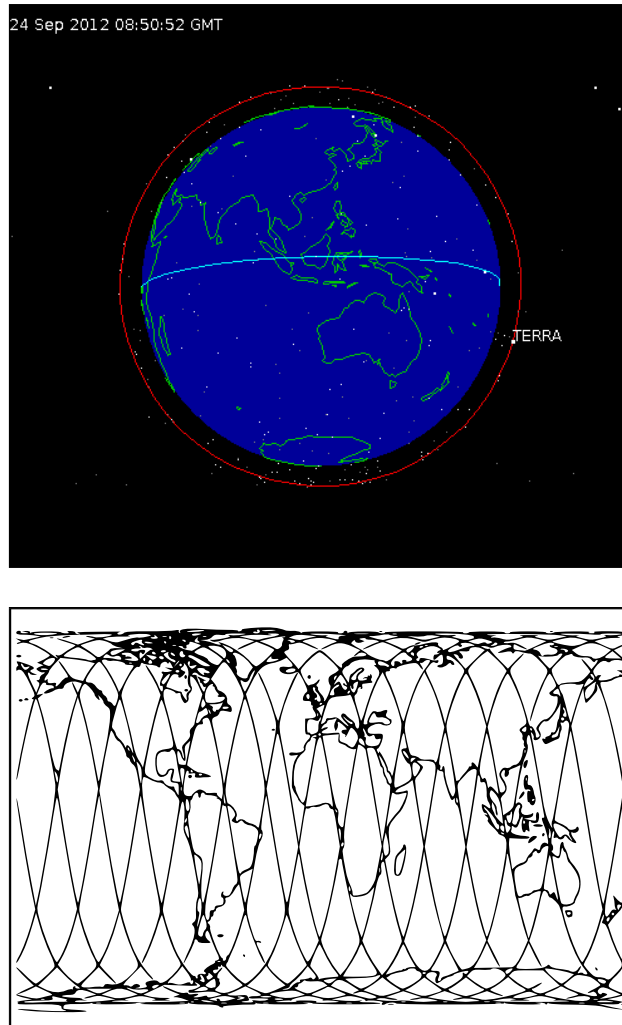
Fig. 1.2 – Global orbit tracks of *Terra* satellite.

1.1.1 The physics of the problem

The AOT products which are available from sensors onboard satellites like MODIS and others are not a direct measurement, but they are obtained from a retrieval based on a physical model. Direct measurements are proportional to the reflected solar radiation that is perceived by the sensor for a certain spectral band; the contribution of aerosols to this incoming reflectance is only partial, as we will see in more detail in this section.

Earth observations are made at wavelengths from 260 nm in the ultraviolet (UV) through radar wavelengths (0.1—10 cm): the ability to see through clouds and probe down to surface exists only at radar wavelengths, thus clouds heavily condition satellite observations for air quality. The strong absorption of energy of the ozone layer (which is about 20—30 km above the surface) inhibits to see UV absorbing gases below it, in the lower troposphere. Bright surfaces like desert or snow can also mislead the sensor: the scattered radiance is too high on those areas and hence the satellite cannot discern the contribution of scattering along the atmosphere from the contribution of the surface.

To better figure out the different parts of electromagnetic radiation which contribute to the received satellite measurement, Fig. 1.3 will now be explained. The incoming flux of solar radiation is scattered (and absorbed as well) by the gases and aerosol particles in the atmosphere; these rays can either be scattered somewhere on different directions, or either be directed (directly or by means of multi-scattering deviations) in the field of view of the satellite (cases 2 and 3 in the figure). The surface then reflects the incoming radiation (components 1 and 3) back to the atmosphere which in turn will be filtered by other gases and suspended particles along the path before reaching the Top Of the Atmosphere (TOA). Other contributions of scattered light are received by the satellite sensor, i.e. the beams coming from neighbouring areas/pixels (component 4 in Fig. 1.3), and the upwelling In-
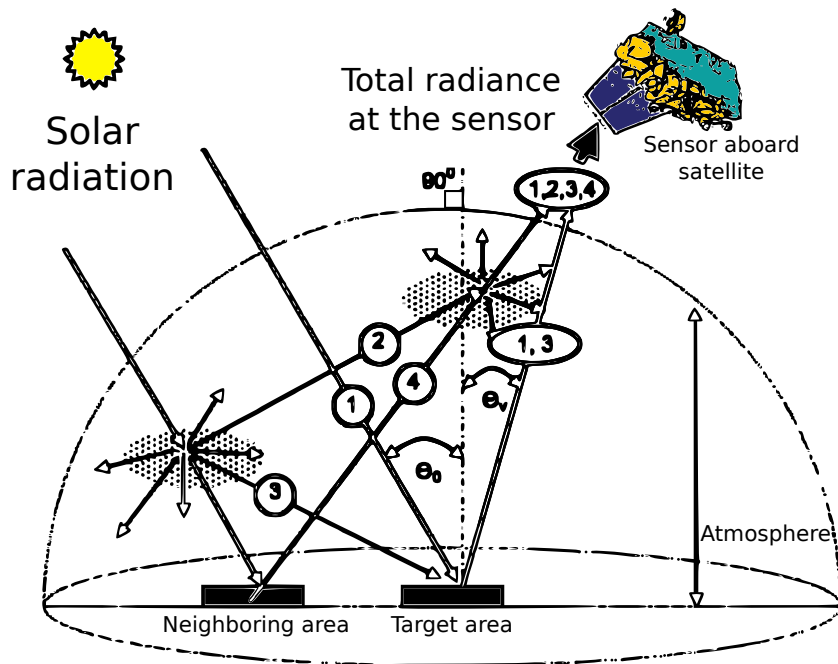
Fig. 1.3 – Components of solar radiation perceived by a satellite.

fraRed (IR) radiance from the surface (not highlighted in the picture) which represents the largest source of background radiation for IR channels. These last wavelengths are however very important in cloud screening because the temperature of high, thin clouds (cirrus) are much colder than the underlying surface, clouds, and aerosols below.

In general, the radiation reflected from the surface (component 1 in the picture) is the main term of comparison with the radiation directly scattered by the particle and gases in the atmosphere, and that is indeed used by Earth-viewing satellites to extract aerosol features. The radiative transfer equation is generally written separately for the visible (dominated by the solar input and scattered light) and the IR atmosphere, where absorption and surface contribute the most. For further details refer to Thomas and Stamnes (2002).

The acquisition of aerosol features depends on physical models to account for the particle characteristics and the underlying surface reflectivity, as well.

Indeed, Husar (2011) points out the inherent limitations of deriving aerosol properties from the measured scattering of solar radiation, so that there is an intrinsic not negligible level of uncertainty in these data. Satellite observations should not be used as unique drivers for deriving air quality information; they rather should be used in combination with models and vertical profiles coming from active profilers (lidars) to really obtain improved estimations of pollutant concentrations. The ultimate system for air quality modelling would be a collection of integrated measurement systems using geostationary passive imagers (for hourly resolution) combined with lidar rangers (vertical profiling) and integrated with ground based pollutant concentrations (Hidy et al., 2009). Sec 1.3 will go through these issues in more detail.

1.2 Aerosols and aerosol optical thickness

In this section you will be introduced to the physics of the aerosol particles, their role in Earth balance and the different features that can be used to describe their nature and presence in the atmosphere. Being of absolute primary importance for both the studies carried out in this thesis and in the literature, a special remark will be given to the Aerosol Optical Thickness (AOT).

Technically, aerosols are tiny solid and liquid particles and are present throughout the atmosphere. The *primary* particles are introduced directly into the atmosphere, while the *secondary* particles are formed by chemical reactions, like gas-to-particle conversion for instance which can happen by either nucleation, condensation or reaction in liquid droplets (Breslow, 2002).

Key aerosol groups include sulfates, organic carbon, black carbon, nitrates, mineral dust, and sea salt (Tie et al., 2005). In practice, aerosols often bunch up together to form complex mixtures, and are mainly responsible for hazy skies (see Fig. 1.4).
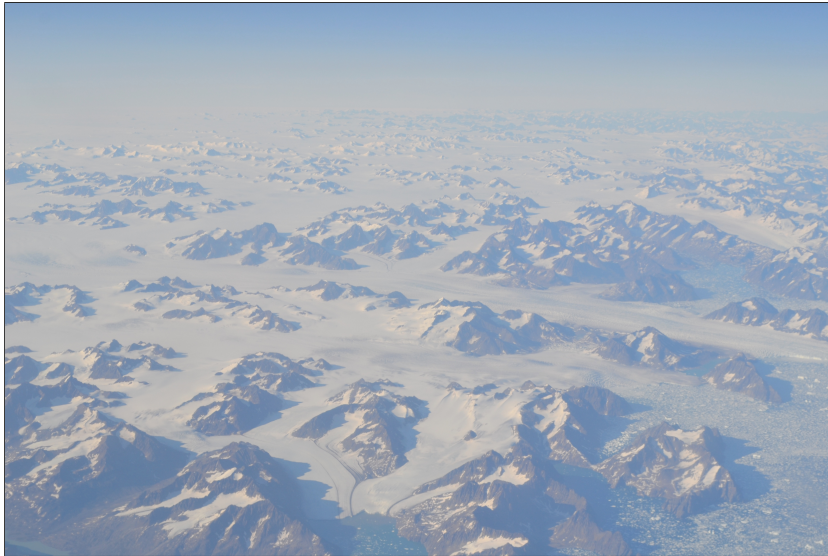
Fig. 1.4 – Hazy sky caused by tiny aerosols in the low troposphere (Greenland).

Aerosols can either occur naturally due to wildfires, volcanic eruptions, dust storms, suspended salts from sea spray, and plant respiration; or either they are produced by humans, from cars emissions, factories, biomass burning, and agricultural dust. Regulatory agencies use to call them Particulate Matter (PM), identifying the measured dry-mass aerosols concentrations at ground level, and usually adopted as a hint of soot, smoke and ash. Although about 90% of the aerosols in the atmosphere have natural origins, it is actually the remaining anthropogenic 10% that dominates the urban and industrial areas (NASA Earth Observatory, 2010).

Aerosols are so important because they represent an area of uncertainty within Earth's climate system. They are like a 'wild card', Kaufman once explained. "They are hard to predict because they act like double agents in the system." His point was that aerosols can cause warming — by absorbing more light than they reflect (e.g. black carbon) — or cooling — by scattering sunlight back to space (as sulfates or nitrates do) — of the Earth's surface, depending upon their size, type, and location (http://earthobservatory.nasa.gov/). Aerosols can enhance cloud formations or they can suppress them by interfering with the process of convection. They
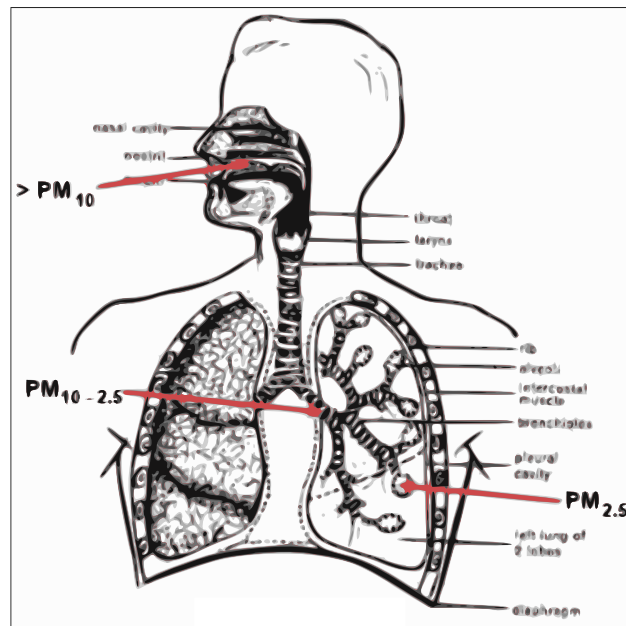
Fig. 1.5 – Particle hazards for human health: below a diameter of 10 µm of size they are inhaled, while finer particles below 2.5 µm can reach the alveoli.

can intensify precipitation, or they can suppress it. What makes it highly challenging to model is its high spatial and temporal variation, as well as its capacity to be transported for even thousand of kilometers, despite deposition and cloud formation along the path (Slanina, 1997).

Aerosols have caught large attention especially for their impact on human-health: when inhaled into the lungs, particles can be a health hazard to humans, and long exposures have been linked to asthma, poor lung development in children, cancer, and in general they cause an increase in cardiac and respiratory morbidity[5] and mortality (Nel, 2005). Fig. 1.5 depicts the different levels of inhalation of aerosol particles through the mouth based upon their size. Head and tracheobronchial deposition increase with increasing particle size, whereas alveolar depositions decrease for particles larger than 4 microns (Lippmann and Albert, 1969).

A convenient way to estimate the presence of aerosols in the atmosphere

---

[5]The rate of incidence of a disease.

is the Aerosol Optical Thickness (AOT), sometimes called Aerosol Optical Depth (AOD), or simply τ. It is a unitless measure and it is defined as the integral of the atmospheric extinction coefficient from surface to space. In other words it is the degree to which aerosols prevent the transmission of light by absorption or scattering. According to the Beer–Lambert–Bouguer Law, being I_0 the radiation emitted by the Sun, and I the radiation received by the passive sensor, the total atmospheric optical thickness τ is defined as follows:

$$I/I_0 = e^{-m\tau} \tag{1.1}$$

where m is the relative airmass[6]. The atmospheric optical thickness can be divided into several components: Rayleigh scattering, aerosols, and gaseous absorption. A more technical insight on the AOT inversion from measured reflectance will be treated in the next chapter, whereas for further details on atmospheric extinction and optical depths see Biggar et al. (1990).

AOT has proved to correlate with ground pollution concentrations, namely PM_{10} and $PM_{2.5}$: a consistent body of literature shows that air quality can be assessed from this columnar satellite product (Wang and Christopher 2003; Engel-Cox et al. 2004; Gupta et al. 2006 for example), however there are several aspects that needs to be accounted to: AOT is indeed *not* equivalent to PM, and this will be better explained in the next section.

---

[6]In astronomy, air mass (or airmass) is the optical path length through Earth's atmosphere for light from a celestial source, i.e. the Sun in our case. It is usually intended as *relative* air mass, so that it is normalized to the air mass at the zenith (at sea level).

1.3 The relationship between PM and AOT

A monitoring of PM_{10} by remote-sensing observations would be perfectly possible if we could build some unique relationship between AOT measurements and the particle mass concentrations, which however depends on many factors such as the size, chemical composition and shape of the particles. Neither is this relationship clear and straightforward, nor it is fixed: it actually strongly relies on the geographical location under study, and on the meteorological conditions (Pelletier et al., 2007). As an example, previous studies showed promising correlations of 1-month time-series of AOT and $PM_{2.5}$ for many stations in the Eastern and Midwest USA, whereas other stations, particularly in the Western USA, did not show almost any correlation at all (Koelemeijer et al., 2006). Again, a comparison of AOT and PM measurements over the Fresno Supersite in California (Watson et al., 2012), showed clearly different empirical AOT-$PM_{2.5}$ relationships by season: because AOT was actually lowest in winter, this might have suggested that surface $PM_{2.5}$ concentrations were also lowest in winter, which was however not the case!

In addition to these difficulties, both the observations have intrinsic measurement errors and, more important, the spatial *and* temporal samplings highly differ: on one side we have temporal averages of PM dry mass concentrations over a single location, on the other side we have semi-instantaneous columnar averages of aerosol particles over several square kilometers of area (Yahi et al., 2011): although "human-breathing-zone" monitoring is what mostly concerns us, most pollutants reside vertically above the surface stations.

To understand which factors can influence the relationship between AOT and surface PM, we can derive an analytical expression of it. Assuming a homogeneous atmospheric layer with spherical aerosols of density ρ, then the dry mass of sampled PM at the surface can be written as[7]:

---

[7]Recalling that the volume of a sphere of radius r is defined as $(4/3) \cdot \pi \cdot r^3$

$$\text{PM} = \frac{4}{3}\pi\rho \int r^3 n(r)\,\mathrm{d}r \qquad (1.2)$$

where $n(r)$ represents the distribution of aerosol sizes in the column. Equation 1.2 simply defines the sum of the weights of each single aerosol particle in the atmospheric volume (Koelemeijer et al., 2006).

It should be pointed out that aerosol particles are subject to hygroscopic growth due to humidity in the atmosphere, thus increasing the scattering power of the particles while keeping the PM *dry* weight fixed. The AOT at height H can then be expressed as (Hansen and Travis, 1974):

$$\text{AOT} = \pi \int_0^{\text{H}}\int_0^{\infty} r^2 Q_{ext}^{amb}(r) n^{amb}(r)\,\mathrm{d}r\,\mathrm{d}z \qquad (1.3)$$

which, under dry conditions (so that we can include the PM definition), and solving the integral over the height, turns into:

$$\text{AOT} \approx \pi\text{H}\cdot f(\text{RH})\int_0^{\infty} r^2 Q_{ext}^{dry}(r) n(r)\,\mathrm{d}r \qquad (1.4)$$

$$\approx \frac{3\cdot\text{PM}\cdot\text{H}\cdot f(\text{RH})}{4\rho\cdot\int r^3 n(r)\,\mathrm{d}r}\int_0^{\infty} r^2 Q_{ext}^{dry}(r) n(r)\,\mathrm{d}r \cdot \frac{\int r^2 n(r)\,\mathrm{d}r}{\int r^2 n(r)\,\mathrm{d}r} \qquad (1.5)$$

$$\approx \frac{3}{4\rho}\text{PM}\cdot\text{H}\cdot f(\text{RH})\frac{\langle Q_{ext}^{dry}\rangle}{r_{eff}} \qquad (1.6)$$

where $f(\text{RH})$ is then the function that defines the ratio of the extinction efficiencies respectively under ambient relative humidity conditions $Q_{ext}^{amb}(r)$ and under dry conditions $Q_{ext}^{dry}(r)$; $\langle Q_{ext}^{dry}\rangle$ is the averaged size-distribution integrated extinction efficiency under dry conditions; and r_{eff} is the so-called effective radius, namely an area weighted mean radius of the aerosol particles,

and defined as $\int r^3 n(r)\, \mathrm{d}r\, /\, \int r^2 n(r)\, \mathrm{d}r$.

Eq. 1.6 clearly shows how the AOT should better represent the surface dry particulate in case the scattering efficiencies changes due to humidity ($f(\mathrm{RH})$) and the height of the atmospheric layer (H), are taken into account. This can be understood by the dilution effects of the vertical mixing of the aerosols and the fact that satellites measure aerosols under humid conditions, which is not the case of the ground measuring stations of PM which derive dry-mass densities.

A further element that controls the concentration of particles in the air is temperature. On one side it can enhance the photochemical reactions in the atmosphere and hence the production of PM particles; on the other hand strong temperature inversions can keep the mixing layer at low elevations hence keeping the aerosols at surface level, inhibiting vertical mixing (Gupta and Christopher, 2009b).

In conclusion, there are premises for "gap-filling" the surface-based networks, especially during well-mixed conditions with stable pressure systems where usually atmospheric aerosols correlate well with the surface. Nonetheless, the opportunity of using satellite observations to fill in surface measurements is still weakened with an understanding of the limitations of space-based measurements in adequately characterizing lower-troposphere conditions. In spite of this, it is still true that satellite observations, especially on long-term records (Van Donkelaar et al., 2009), clearly provide valuable knowledge of concentration distributions and can assist the air quality community (e.g. NASA-NOAA partnership).

1.4   Air quality guidelines

The World Health Organization (WHO, http://www.who.int/) is the reference organization for several health-related guidelines which are offered principally to policy-makers of any developed/developing country throughout the world. Amongst these, air quality guidelines are provided: national standards can then vary, according to own local circumstances and local health risk management, linked mainly to technological, economical, political and social factors.

Guidelines for air quality are given separately for particulate matter, ozone, nitrogen dioxide and sulfur dioxide. There is still an acknowledged intrinsic limitation in giving distinct guidelines for these pollutants, due to the complexity of air pollution mixture: nitrogen dioxide (NO_2) for example is known to be associated to UltraFine (UF) particles (i.e. $PM_{0.1}$) and to be a precursor of ozone and other toxic pollutants.

Based on the currently (Global Update 2005) available scientific evidence (Dockery et al., 1993; Pope III et al., 2002; Jerrett et al., 2005), the following guidelines for PM are suggested:

$$
\begin{array}{ll}
\mathbf{PM_{2.5}:} & 10\ \mu g/m^3 \text{ annual mean} \\
& 25\ \mu g/m^3 \text{ 24-hour mean} \\
\mathbf{PM_{10}:} & 20\ \mu g/m^3 \text{ annual mean} \\
& 50\ \mu g/m^3 \text{ 24-hour mean}
\end{array}
$$

Although the majority of epidemiological studies refer to PM_{10}, simply because PM_{10} routine monitoring stations are far more widespread, there are some cases in which the distribution between the *coarse* (particle size between 2.5 and 10 µm) and *fine* (particles smaller than 2.5 µm) is not equally distributed. Whereas the former are mainly produced by mechanical processes like construction activities or road dust, the latter mainly comes from

combustion: hence, $PM_{2.5}$ guidelines are also provided for areas where the fine mode dominates, which are simply derived from typical fine/coarse ratios found in urban areas (0.5—0.8).

Though the annual average constraints tend to take the precedence for being more restrictive, it is however over true that short-term peaks of PM concentrations can lead to equivalently dangerous effects on human health, as reported by several studies (Katsouyanni et al., 2001; Samet et al., 2000; Ezzati et al., 2004). For this need, as well as for fining exceedances, 24-hour mean thresholds also suggested along with the annual ones.

In areas with high levels of pollution, other *interim* targets are proposed to encourage a gradual achievement of the final reported guidelines. Even though critical concentrations of pollutants in the air can clearly have serious health consequences on the population, it should be stressed that still research has not identified thresholds *below* which some harmful effect does not occur, so that there is no full protection that can be ensured in any case. This is especially true for airborne particulate matter (World Health Organization, 2006).

In Europe, Air Quality Directives (AQD) are still unclear regarding the use of models for the support of AQ policies (European Commission, 2012): they simply state that *"the results of modelling and/or indicative measurement shall be taken into account for the assessment of air quality with respect to the limit values"*, but their role is not further explained.

The FAIRMODE group (European Environment Agency (EEA) and European Commission Joint Research Centre (JRC), 2008) — a forum of AQ experts which is trying to harmonize the modelling techniques and to give inputs to the European legislation — has identified the major applications of models within the AQD, namely exceedances assessment, forecasting, source allocation and control measures assessment. This forum is trying to push changes in the current directives in order to clarify the roles of models in

the AQ policies and increase the importance of modelling estimates, up to their mandatory use. Models do not only serve as tool for assessing and handling the risk on certain areas, but as well can have impact on the number and optimal design of future monitoring stations, and should be used for regulatory purposes, once they have shown to fulfill some required quality objective. Still these recommendations are waiting for official responses from the European Parliament.

This section concludes the first introductory chapter. Next chapter will have a closer look at the datasets which were used in the models: feature description, measurement instrumentation and algorithmics.

Chapter 2

Input Data Description

Different models for PM_{10} spatial filling have been tested during this research activity, over two areas of interest — Emilia Romagna and Austria — and with different input datasets. This section is going to describe the whole set of data sources which have been used for both modelling and validation analysis.

The chapter will start with the description of the different AOT observations that were available and used, with a focus on the MODIS inversion algorithm to let the reader understand which kind of uncertainties and approximations can arise on this product, and for different levels of spatial resolutions; secondly the description will move to the ground measurements of particulate matter in Emilia Romagna and Austria, and finally to the auxiliary variables that were included in the models for further explanatory purposes.

2.1 Aerosol optical thickness retrieval

The widely used way of describing the columnar loading of aerosols in the atmosphere is by evaluating its optical thickness. Sec. 1.2 initialized the reader to the concept of AOT: in this section instead a description of two different ways of observing AOT will be proposed, namely uplooking from the ground (the ground *truth*) and downlooking from satellites, along with pros and cons of both measurements.

2.1.1 AERONET uplooking sunphotometers

Generally, instruments measuring the optical depth of a particular gas or substance from the ground are extremely useful mostly as they act as reference for the remote-sensed observations: a means of validation of the satellite products.

The optical thickness of the aerosols is usually measured on the ground by photometers pointing to the Sun: the atmospheric effect (see component 3 in Fig. 1.3), hence the reduction of the solar flux by scattering and absorption in the atmosphere, can be removed with the so-called Langley extrapolation method: in absence of clouds and with a constant aerosols layer (at high altitudes) one can assume a linear relationship between the received direct-Sun radiance and the airmass, that can be inferred by repeated measurements. Extrapolating at a null airmass, the extraterrestrial Sun radiance can be measured. This can be easily observed by taking the logarithm of Eq. 2.1:

$$\ln I = \ln I_0 - m\tau \tag{2.1}$$

Once I_0 is known, hence the sunphotometer is calibrated, than the optical

depth of the atmospheric can be determined.

Several networks of uplooking sunphotometry are available globally nowadays, AErosol RObotic NETwork (AERONET) being the largest. This network, established by NASA and PHOTONS, was set up initially ∼20 years ago and now counts almost 600 sunphotometers equally spread over the Earth. Aerosol (not only optical) properties are acquired then freely distributed via either Web download tool or FTP transfer.

Measurements are taken at eight different wavelengths, namely from 340 to 1020 nm, on a preprogrammed temporal sequence starting at an air mass of 7 in the morning and ending at an air mass of 7 in the evening. Each observation is meant as a triplet of measurements over 30 seconds of time, in order to screen out clouds which usually show a much higher variance in time in their optical depth. Thanks to the wide spectrum of measurements, the contribute of the aerosols particles can be isolated by removing the attenuation of the smaller particles (Rayleigh scattering) and the absorption of ozone and other gaseous pollutants (NASA, 1993). The zero air mass radiation for the calibration is inferred to an accuracy of approximately 0.2 to 0.5% thus resulting in an uncertainty of optical depths of 0.002 to 0.005. AOT products are then distributed at three quality levels: Level 1.0 (unscreened) and Level 1.5 (cloud-screened) data in near real-time; Level 2.0 quality-assured data after a longer delay for manual inspection and final calibration.

2.1.2 MODIS AOT algorithm

This section will describe the principles behind the AOT algorithms for the MODIS sensor. Specifically, Collection 005 is considered, being it the one including spectral inputs of the AOT information used in this study.

The MODIS imager onboard Terra and Aqua satellites (see Sec. 1.1 for de-

tails) provides a long series of products, from raw radiances to more sophisticated products related to atmosphere, land, ocean and crysosphere.

The aerosol products, called either MOD04 (Terra), MYD04 (Aqua) or M?D04 (both), rely on the calibrated georeferenced perceived reflectances, called Level 1B, L1B or M?D02 products. Possible errors can be associated to these raw measurements upon radiometric noise, digitization, and possible calibration nonlinearities, as discussed in Ignatov et al. (2005). Further 'Level 2' datasets are then used in the algorithm, like the cloud mask (MYD35) and the atmospheric profile (MYD07), as will be described in the following paragraphs.

As a first distinction, due to the different radiative properties, two independent algorithms are applied over land pixels and over ocean pixels[1]. Both of them are based on a 'look-up table' (LUT) approach, which stores precomputed radiative transfer calculations for a finite set of *aerosol* and *surface* parameters: spectral reflectance from the LUT is compared with the measured spectral reflectance to find the optimal (least-squares) fit. The models in the table take into account all the factors that influence the radiative transfer, including observation geometries, the surface type, the elevation of land and Sun. Although the input reflectances reach a resolution of 250 m, the final output maps of AOT are then distributed at an horizontal resolution of 10 km at Nadir, in order to reduce the noise in the inversion.

The first step in deriving the aerosol optical thickness is to collect spectral reflectances over different bands (for the complete set of bands used in the aerosol retrieval, see Tab. 2.1) so as to be able to screen out pixels over cloud and critical surfaces like ocean and heavy dust glints, snow and ice, which cause a high uncertainty in the AOT retrieval. These reflectances are corrected for water vapor, ozone, and carbon dioxide before the algorithm proceeds.

---

[1]The algorithm over land is selected when at least one pixel in a 10×10 box is not considered water.

Table 2.1 – The seven MODIS channels that are used in the AOT inversion algorithms.

Band #	Bandwidth (µm)	Weighted Central Wavelength (µm)	Resolution (m)
1	0.620—0.670	0.646	250
2	0.841—0.876	0.855	250
3	0.459—0.479	0.466	500
4	0.545—0.565	0.553	500
5	1.230—1.250	1.243	500
6	1.628—1.652	1.632	500
7	2.105—2.155	2.119	500

Only the *dark pixels* are considered good for the algorithm, and if there are enough pixels in the current box, then the algorithm continues with a further screening of the brightest and darkest pixels left: this is a sort of precautionary measure in order to remove remaining pixels which might have been possibly contaminated by cloud shadows, residual cloud contamination and odd surfaces at either the bright or dark end.

Once the uncertain pixels are filtered out, the retrieval estimates (over land) the contribute of the surface in the reflectance (Tanré et al., 1997): this is then used as in input in the LUT along with the total reflectance, to retrieve the AOT. A weighting parameter is also computed in order to balance the fine and coarse components of the aerosol model. As output of the LUT, the optical depth is finally retrieved at 0.55 µm, which is often used as reference in global climate modelling.

Actually, the algorithm over land retrieves the AOT at two different channels (#1 and #3) which have an established relationship with the surface reflectance (at 2.13 µm), and which is instead missing at the target wavelength of 0.55 µm and which partly define the models in the LUT. Fig. 2.1 shows the empirical linear relationships used in the MODIS algorithm (further variables of the regression are considered to refine the relationship, Levy et al. 2009).
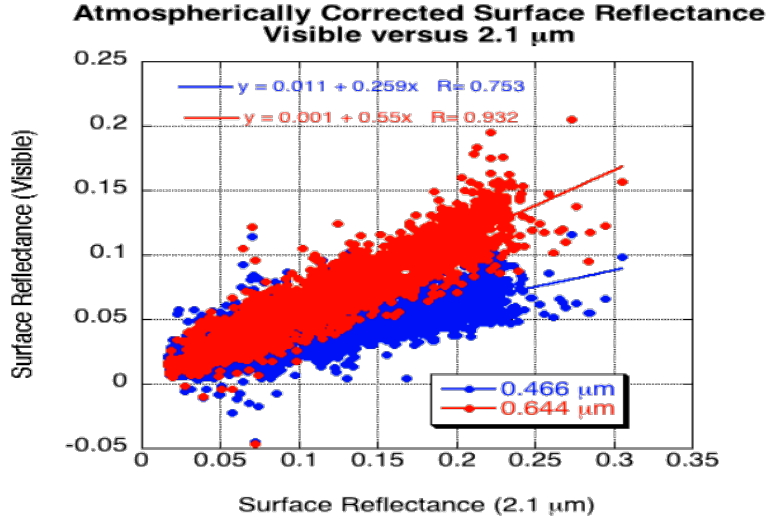
Fig. 2.1 – Linear regression between surface reflectances in the visible (0.47 and 0.66 µm channels) and the 2.12 µm SWIR channel. Image courtesy of L.A. Remer et al.

AOT is therefore interpolated by using the Ångström exponent α, which drives the relationship between spectral AOT and the wavelength:

$$\alpha = -\frac{\log \frac{\tau_{\lambda_1}}{\tau_{\lambda_2}}}{\log \frac{\lambda_1}{\lambda_2}} \tag{2.2}$$

These were the general principles behind the AOT inversion; for details on the algorithms over both land and ocean, refer to Remer et al. (2005).

The expected uncertainty for the optical thickness τ was found to be:

$$\Delta\tau = \pm 0.03 \pm 0.05\tau \quad \text{over ocean}$$
$$\Delta\tau = \pm 0.05 \pm 0.15\tau \quad \text{over land}$$

which generally holds independently of the output wavelength. There are only some particular conditions under which the expected accuracy of the retrieval might not be met, e.g. whit non-spherical dust over ocean or over coastal areas.

During aerosol retrieval on a particular 10 km box, the algorithm may encounter either non-fatal or fatal errors: quality flags are associated to each single AOT pixel, mainly to constrain out less confident data in the quality-assured OPTICAL_DEPTH_LAND_AND_OCEAN product (NASA, 1999).

Inversion algorithms for MODIS are organized in *Collections*, the current being collection 005. Collections are meant as products that are generated by similar, but not necessarily the same, versions of the algorithms. A history of changes that were applied from the initial pre-launch AOT algorithms can be found in Remer et al. (2006). The forthcoming collection 6 will include (though a first version was included already in C005) the *Deep Blue* algorithm (Hsu et al., 2004, 2006) which will increase the capabilities to extract data over bright surfaces (e.g. deserts), will improve the cloud screening, the aerosol physical models and the calibration.

2.1.3 PM MAPPER AOT

PM MAPPER is a software system for air quality monitoring applications from global- to local-scale. It consists of a two-steps cascade process, capable of handling the multispectral data input acquired by the MODIS sensors. The input and output details of the processing are shown in Fig. 2.2: the first part is a tuned version of MODIS data from IMAPP software (HUANG et al., 2004), so as to achieve AOT products with higher spatial resolution and higher availability (Nguyen et al., 2010a; Nguyen, 2012); the second part aims at the deduction of air quality maps from the original aerosol data.

A first version of the inversion algorithm retrieved AOT data at 3×3 km^2 of spatial resolution, to allow for local scale/urban areas monitoring. Validation of these product has been carried out with success by Nguyen et al. (2010b), with overall good comparison with MODIS standard products and a higher capacity in retrieving AOT information over land areas, especially coastlines
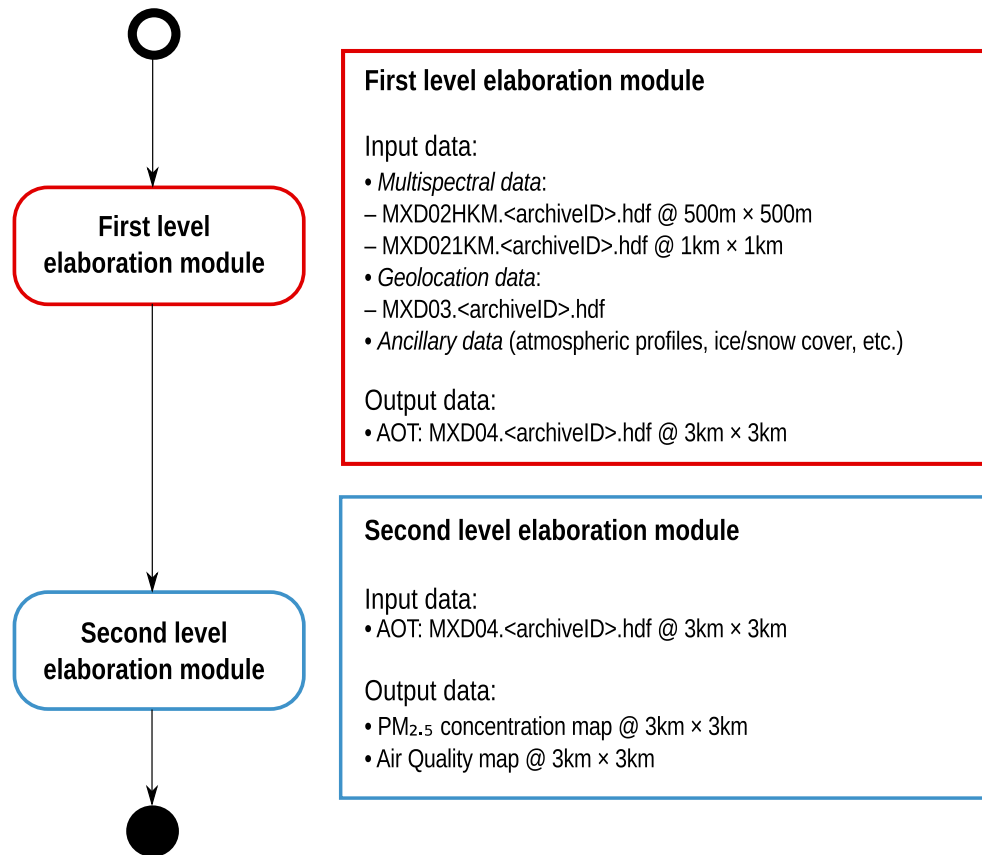
Fig. 2.2 – The two-step cascade architecture of PM MAPPER.

where original MODIS products lack. Further proceedings in the algorithm could lead the retrieval up to a resolution of 1×1 km^2, with increased capabilities of retrieval over bright and dark surfaces: this validated product (Campalani et al., 2011a) was actually used in the PM$_{10}$ models described in the next chapters.

The algorithm flow is analogous to the one described in the previous section, hence essentially tries to isolate the radiative contribute of aerosols by means of several auxiliary information from surface, geometry and spectral reflectances, screening out clouds and overly bright (and overly dark) pixels. The details of the algorithm are described in MEEO Srl (2009). To perceive the kind of detail that can be expressed with a 1×1 km^2 product, a sample map is shown in Fig. 2.3.
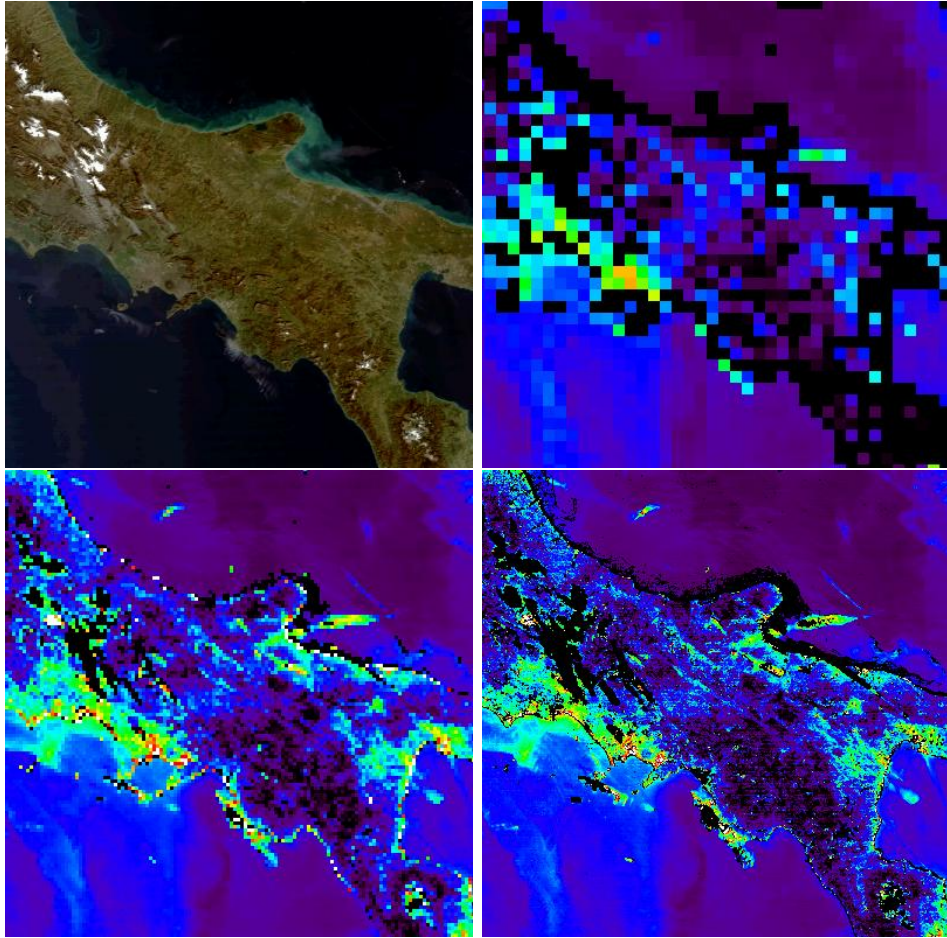
Fig. 2.3 – PM MAPPER AOT product samples at different resolution levels: 10×10 km^2 (upper-right), 3×3 km^2 (lower-left) and 1×1 km^2 (lower-right) over Southern Italy.

2.2 Ground measurements of PM

Two networks of air quality ground stations were used: the first one is the network managed by ARPA (`www.arpa.emr.it`), the Regional Environmental Agency in Emilia Romagna (Italy); the second one is the Austrian Air Quality network managed by the Umweltbundesamt (`www.umweltbundesamt.at`), the state environmental protection agency in Austria.
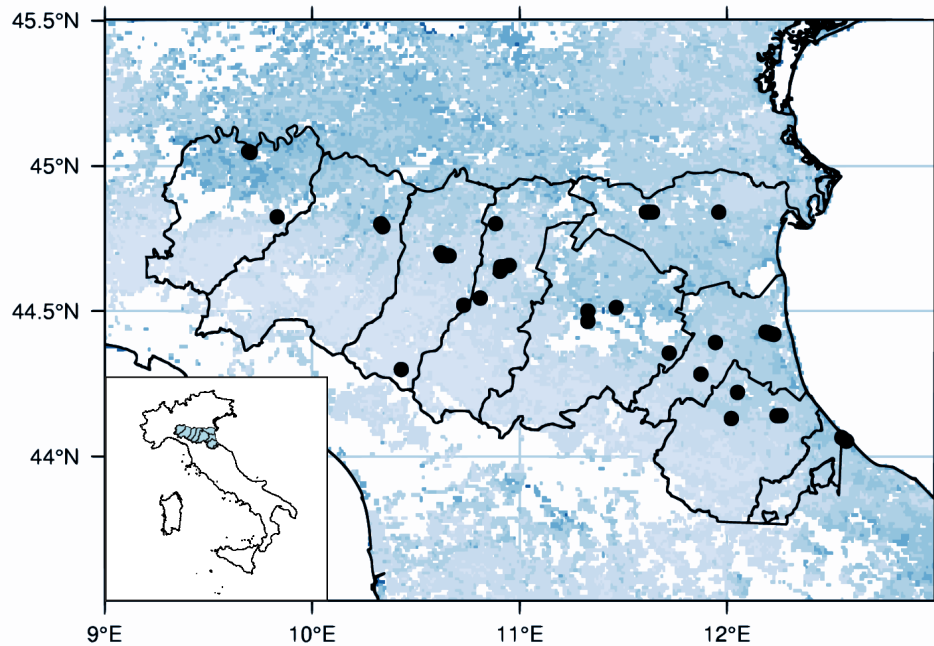
Fig. 2.4 – Layout of ARPA ER air quality ground stations (black points).

2.2.1   ARPA Emilia Romagna network

ARPA Emilia-Romagna (ARPA ER) is the regional agency for prevention and environment in Emilia Romagna (Italy). It is operative since 1996 and has institutional duties for:

- monitoring environmental components;

- controlling and overseeing the territory and the anthropic activities;

- supporting the evaluation of the environmental impact of plans and projects;

- realizing and managing the regional informative system of the environment.

ARPA ER is delivering daily charts of PM_{10} and $PM_{2.5}$ over the whole region by means of about 60 ground stations (May 2010). The charts contain the 24-hours mean of the measured particulate of one day, almost continuously during the period of activity of each station. Their location is visualized in Fig. 2.4: clearly there is a relatively high clustering in the pattern of the stations, inevitably because of the higher interest in measuring high polluted industrial/urban traffic areas. Exhaustive metadata on single stations can be found in Campalani and Pasetti (2010a).

For further details and technical reports, see ARPA Emilia Romagna (1995).

2.2.2   Austrian network

The measurements of PM_{10} for the models over Austria were taken from the Austrian Air Quality, which currently comprises $\sim$160 . The data was kindly provided by the regional Austrian administrations and extracted from IDV (Immissions Daten Verbund) which is a database containing all measurements from the operational Austrian Air Quality network.

The Umweltbundesamt is the expert authority of the federal government for environmental protection and thus responsible for writing the State-of-the-Environment Reports, involving different areas of interest, like soil and water waste, biological diversity protection, forest use, industrial plants, etc. And of course, air. The last available report (01-2007 to 12-2009) states that the PM_{10} emissions have increased from 2006 to 2008 by 0.5 percent from 35,400 tons to 35,600 tons; the $PM_{2.5}$ emissions have instead decreased by 2 percent from 21,500 tons to 21,100 tons. Prominent source sectors of PM_{10} and $PM_{2.5}$ emissions are industry (27% and 17%), lower consumption (29% and 44%), transportation (23% and 25%) and farmers transport community (15% and 6%).

Table 2.2 – Exceedances rate of PM_{10} in Austria from 2006 to 2008.

Year #	Exceedances rate	Measuring Points
2006	64%	111
2007	20%	127
2008	12%	134

With regards to PM_{10} specifically, in 2006 the limit values (Sec. 1.4) were passed to up to two thirds of all sites, with more stress over urban areas, inner-alpine valleys and basins. The decrease in exposure from 2006 to 2007 and 2008 (see Tab. 2.2) was primarily related to the less frequent occurrence of meteorological conditions which were favorable for the air pollution: e.g. the mild winter months in 2007 and 2008 have shown less temperature inversions overall.

The Umweltbundesamt does not publish reports with technical descriptions of the monitoring methods used. For further details see Umweltbundesamt (1999).

2.3   Auxiliary data

As underlined in Ch. 1, the aerosols atmospheric information observed by satellites is generally not enough for a direct translation to ground concentrations. Recalling Eq. 1.6, it is clear how the relationship linking the AOT and the dry particulate is involving further meteorological and topographical information which should be embedded in the model of PM. The auxiliary variables that were included in our models are described in the next subsections, namely the meteorological variables in Sec. 2.3.1, the Digital Elevation Model (DEM) in Sec. 2.3.2 and the yearly averages of Night Lights (NL) in Sec. 2.3.3.
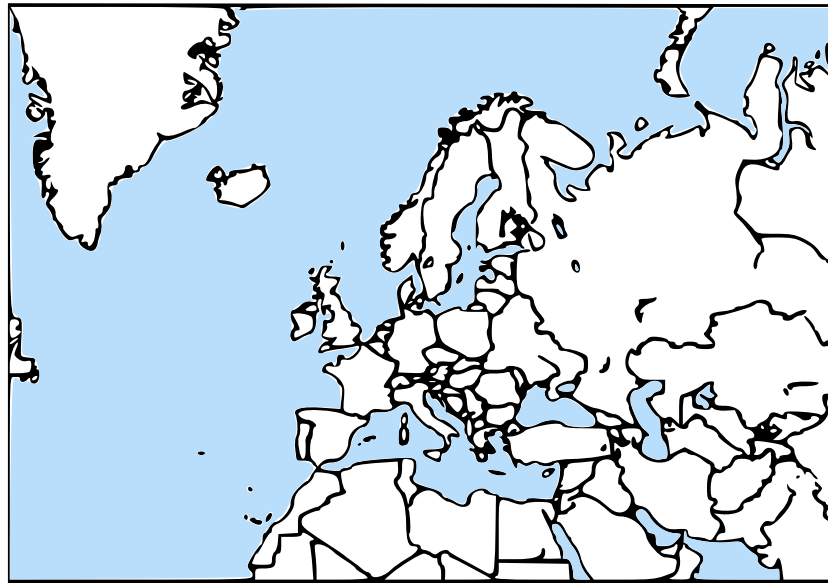
Fig. 2.5 – Mother domain of the WRF simulations for meteorological fields (Lambert-conformal grid, $dx = dy = 27$ km).

2.3.1   Meteorological data

Simulated meteorological fields of wind, temperature, pressure, relative humidity and planetary boundary layer height were provided on a 3-dimensional grid by ZAMG (Zentralanstalt für Meteorologie und Geodynamik), the national agency of meteorological and geophysical services in Austria.

The model simulations are based on the world leading 16 km global forecasts provided by the IFS (Integrated Forecast System) of the ECMWF (European Centre for Medium-Range Weather Forecasts). This data is further processed by the Weather Research and Forecasting (WRF) Model, which uses thies fields as initial and boundary conditions, to provide forecasts of meteorology on an hourly basis. The temporal resolution of the ECMWF forecasts is 3 hours. The data is extracted on 16 pressure levels (between 10—1000 hPa) with a spatial resolution of 0.5° in each horizontal direction. These fields are used as initial and boundary conditions by WRF, which conducts forecasts of meteorology on an hourly basis and on 43 model levels. To obtain the
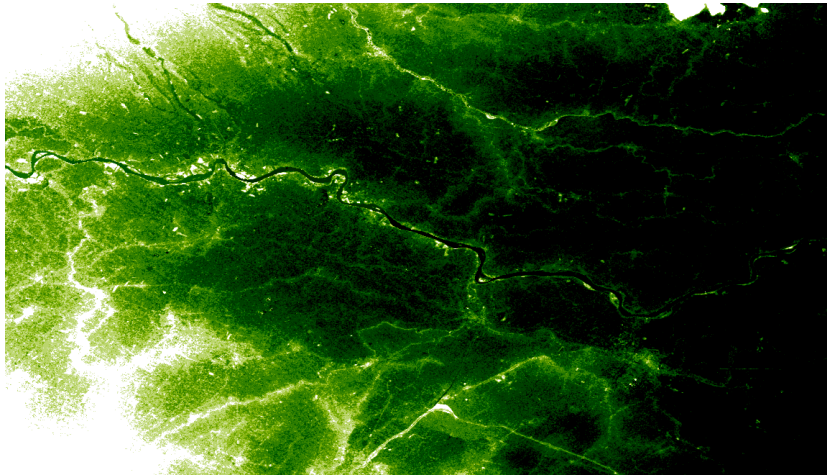
Fig. 2.6 – Examples of original 3 arcsec DEM from SRTM: a cutout over the river Po in Emilia Romagna (Italy).

data set the modelling system is setup to provide forecasts on a resolution of 27 km over the whole European domain (see Fig. 2.5).

For air quality mapping purposes, the surface-level forecasts (1000 hPa) were interpolated to at 1×1 km of spatial resolution with a cubic spline interpolator to meet the resolution of the PM MAPPER products. The 2D grids at surface were extracted to vertically co-locate the meteorological datasets with the PM measurements, so that they could be representative of the meteorological conditions perceived by the ground monitoring stations.

2.3.2   Digital Elevation Model (DEM)

Elevation data was taken from the NASA Shuttle Radar Topographic Mission (SRTM) whose DEM covers over 80% of the globe. The data is distributed free of charge by U.S. Geological Survey (USGS) governmental company, available for download over a mosaiced 5×5 degree tiling scheme, in both ArcInfo ASCII and GeoTIFF formats (The CGAR Consortium for Spatial Information, 1999).
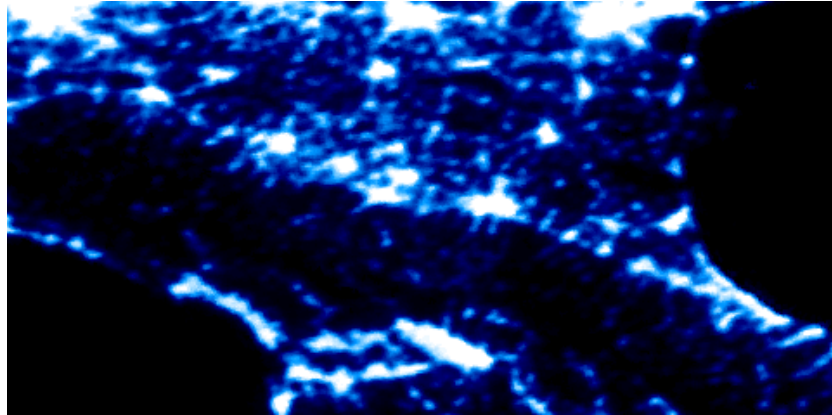
Fig. 2.7 – Cutout of NOAA 30 arcsec nighttime lights average over Emilia Romagna ($9\,°E - 43.5\,°N$ to $13\,°E - 45.5\,°N$).

The SRTM data is available as 3 arcsec ($\sim$90 m resolution) DEMs, with a reported vertical error of less than 16 m, but it was aggregated to the resolution of 1×1 km^2 as input for the models, being it the target resolution of the predictions. Fig. 2.6 shows a small styled cutout over Northern Italy.

2.3.3 Night lights

Yearly averages of remote-sensed night lights are available free of charge thanks to the Earth Observation Group (EOG) of NOAA Federal Agency of the U.S., by means of GeoTIFF archives.

The files are cloud-free composites made using the available archived "smooth" (quality assessed) resolution data of the Operational Linescan System (OLS) instruments onboard the several Defense Meteorological Satellite Program (DMSP) satellites which are orbiting continuously (often two satellites at the same time) from 1992. Each DMSP satellite has a 101 minute, sun-synchronous near-polar orbit at an altitude of 830 km above the surface of the Earth; the final products are 30 arcsec grids, spanning the whole globe within -65 and 75 degrees of latitude. A number of constraints are used to select the highest quality data for entry into the composites, for details refer

to NOAA – Earth Observation Group (1970).

Chapter 3

Spatial Modelling and Online Analytics

This chapter is dedicated to an analytical description of the geostatistical estimation and visualization tools that have been used for the assessment of PM_{10} concentrations over the two areas of interest we focused on: Emilia Romagna and Austria.

Sec. 3.1 will offer an overview of the most widely used model techniques adopted in literature, explaining our decision to choose geostatistical interpolation and, in particular, kriging. Sec. 3.2 will describe the statistical model behind a kriging interpolation, from a simple univariate case up to more complex situations involving multiple variables as well as spatio-temporal interactions. Finally, Sec. 3.3 will show the solutions and design choices which were made for the access of the final predictions in a Web-based scenario.

3.1   Review of modelling techniques

Before describing the mathematical and statistical basis of kriging, an overview on the different modelling solutions and research trends is proposed, along with an explanation on why kriging was chosen as estimator.

Kriging — or better said the kriging suite of geostatistical techniques — is a choice amongst the family of stochastic (least squares) interpolators; although, as we will see, it is an optimal estimator and is widely used in research for air quality assessment, it must be carefully considered before its adoption as it is not the best (nor unique) technique, in an absolute sense.

Zooming out, the geostatistical interpolation only represents a single category among the wider range of models that can be chosen for air pollution assessment. In Jerrett et al. (2004), different classes of exposure models are identified[1], from simple mechanical interpolator and proximity models, to land use regressions, to more advanced dispersion models, up to hybrid models (e.g. personal monitoring + other models). Geostatistical interpolation is then an other solution, which offers advantages and disadvantages: context-specific decisions must be made to correctly optimize the available resources, research time, software, hardware and data.

The best way to measure individual exposure to air pollutants would be to use personal air monitors: the majority of the people passes around 90% of the time indoors, where usually are different concentration levels than in outdoors environments (e.g. Mukala et al. 2000; Liu et al. 1997). However, the use of this method can be prohibitive for large-scale analysis. Proximity models, i.e. risk assessment proportional to the proximity to pollution sources (e.g. Langholz et al. 2002; Maheswaran and Elliott 2003), are the most basic modelling solution but it can still be considered for a first sensitivity analysis, as a driver for further more sophisticated and costly solutions.

---

[1]For intraurban-scale analysis, specifically.

Land use regression models (e.g. Lebret et al. 2000; Brauer et al. 2003), which predict air pollution based on surrounding land use and traffic characteristics with least square regression, is able to produce statistically reliable results and also has a fair *transferability*[2], but is mainly applied for intraurban analysis and do not really account for distances of the locations and measurements.

Dispersion models (e.g. Walker et al. 1999; Potoglou and Kanaroglou 2005) can offer a more realistic fit of the theory structure by including topography, traffic observations, meteorology and pollution: the stationary and mobile emissions sources are then used as starting point to model the dispersion of pollutants. The most widely used is the Gaussian model, which assumes a (pretty unrealistic) Gaussian dispersion of the pollutants. These models require a strong cross-validation process with monitoring data, being prone to errors; they also require high-level GIS and programming expertise, and expensive hardware.

Even more complex models cascade a meteorological module to a chemical one: at every time step the atmospheric conditions are modeled by the meteorological component and sent as input to the chemical dispersion modeler. These models are not widely used actually, having an extremely high implementation and data cost: computational requirements are huge, and high-level programming, meteorology and climatology expertise is preferred. Different types of these so-called Integrated Meteorological-Emission (IME) models exist: from the most accessible *diagnostic* models (e.g. ATMOS1 by Davis et al. 1984); to the *dynamical* models (e.g. MM5 by Grell et al. 1994), which can simulate a much wider set of exposure scenarios; up to the most complex *Four-Dimensional Data Assimilation* (FDDA) models which reduce the propagation of errors (e.g. CALPUFF by Scire et al. 2000).

Jerrett et al. in 2004 correctly pointed out the promising improvement in air quality modelling upon integration of remote sensing satellite systems

---

[2]The capability and ease to transfer the model to other locations.

data with ground monitoring network data. And actually there has been a clear trend in the last years of air quality research in the use of aerosol optical properties. With the increasing role of satellite observations — mainly from MODIS (Terra and Aqua) and MISR (Terra) sensors for these applications — remote sensing data started to be included in the models to detect/ track particulate matter plumes from major events (e.g. dust storms, volcanic emissions, and fires) and to fill the temporal and spatial gaps found with ground-level monitor data, the latter representing the specific context of this thesis.

After a first successful correlation study between PM_{10} and AOT over a single station in Italy ($r = 0.82$) by Chu et al. in 2003, several studies aimed at developing linear regression models for estimating PM concentrations from AOT, either as a direct affine transformation or with multivariate (generalized) linear models.

Wang and Christopher (2003) discovered very good correlations between AOT and $PM_{2.5}$ in Alabama using MODIS data (r of 0.7 with the 1-hour averages, and even 0.98 for 24-hour averages); Kacenelenbogen et al. (2006) found good correlation too using near-polar orbiting ADEOS-2 AOT product with fine particles ($PM_{2.5}$) in France.

Engel-Cox et al. in 2004 analysed the MODIS-AOT/PM ratio over the US, finding variable correlations in the East/Mid-West areas and in the West side; the author hypothesizes this could be caused by wider variety of aerosol types (nitrate/sulfates ratios), increased presence of black carbon (soot), and higher surface reflectivities in the western US, making the AOT retrieval more difficult and more prone to uncertainty.

Gupta et al. — in 2006, 2007 and 2008 for example — developed linear regression models over several different locations, generally finding a good association between PM ground observations and AOT, with a general weaker correlation in Winter and with a strong effect of meteorological conditions due

to **relative humidity** and **mixing layer height**[3] in primis; in particular, the author identifies ideal conditions for a stronger PM-AOT match with a 40—50% of relative humidity and a mixing layer of 100 to 200 m (in a study over global cities). Other studies confirmed the usefulness of humidity and planetary boundary layer height[4], like Paciorek et al. (2008) with GOES-12 AOT products over the US or like Tsai et al. (2011) with MODIS data over Taiwan (the latter underlining how the *haze* layer height[5] was actually better for the normalization of the AOT columnar loading, due to the abundance of aerosols aloft above boundary layer). Fig. 3.1 shows the visible difference in atmospheric conditions below and above the boundary layer.

Hutchison made several study on how to correlate MODIS AOT to the ground-measured PM in Texas (2003, 2004, 2005 and 2008), on both the evaluation of air quality and the detection of aerosol transport; the author describes one of the first cases of joint use of AOT and aerosols **vertical profiles** from CALIPSO (Winker et al., 2006) lidar measurements to assess the air pollution: knowing the vertical structure of aerosol loadings actually is a key information to infer the aerosol concentrations on the ground level. Van Donkelaar et al. has included (model-based) aerosol profiles along with aerosol size and relative humidity to proxy MODIS AOT for air quality assessment over Moscow (2011).

Liu et al. (2007b) built up regression models with MISR AOT data, but using separate AOT model components (fractional AOT) to predict the ground particulate (as well as sulfates and nitrates), and finding overall better regression fit than with total-column AOT.

---

[3]The mixing layer height determines the volume in which turbulence is active and into which fine particles, which are emitted near the surface, are dispersed. The mixing layer shows (approximately) constant potential temperature (temperature failing at a rate of approximately $10\,°C/km$).

[4]Layer that divides the lower *turbulent* atmosphere to the *free* nonturbulent (geostrophic) atmosphere: it can be used as surrogate of the mixing layer.

[5]A layer of haze in the atmosphere, usually bounded at the top by a temperature inversion and frequently extending downward to the ground: it is the sum of boundary and scale height, the latter being the height of a uniform extinction layer above the boundary layer, namely where the aerosol extinction coefficient decreases to $1/e$.

Fig. 3.1 – The planetary boundary layer keeping the aerosol on the low (mixing) atmosphere over Berlin: above the layer the air is cleaner, thus the city lights are (almost) not scattered towards the viewer. Photo courtesy of Ralf Steikert.

Some studies went beyond linear regression models, by using more sophisticated methods like Bayesian hierarchical space-time models (Garcia et al., 2006), recently-developed Partial-Least-Square (PLS) regression techniques (Porter et al., 2012), hierarchical dynamical coregionalisation models (Fassò et al., 2009), or neural networks (Gupta and Christopher, 2009a). A more recent study in 2009 by Liu et al. applied geostationary GOES aerosol/ smoke AOD products in conjunction with land use and meteorological fields to feed a two-stage generalized additive model in Massachusetts, concluding how AOT was actually contributing actively to the prediction power of the model (even though the meteorological seemed to play a major role).

Geostationary products were used as well in recent studies by Emili et al. (2010; 2011) who investigated the predictive power of SEVIRI AOT for PM_{10} over the Alpine region, which showed higher correlations coefficients than MODIS for the year 2008 (0.7 against 0.6) and higher data availability (but with coarser spatial resolution); the planetary boundary layer height was also

found to be of key importance, whereas the role of relative humidity did not strongly influence the regression; the author finally points out the problem of accuracy in the satellite observations for complex terrains, up to the point that inverse distance interpolation could yield more accurate maps of PM_{10}.

In conclusion, these last decade of research on air quality modelling, especially by jointly exploiting the ground measurements with satellite data, produced a myriad of different results (refer to Jerrett et al. 2004 and Hoff and Christopher 2009 for an exhaustive review), and still — as pointed out in Kumar (2010) — there are important spatio-temporal mismatches in the datasets that are not addressed and compromise the modeled maps. Shared results can be extrapolated overall: spaceborne AOT can be potentially used to help assessing the air quality risk, though usually needs either explanatory meteorological variables or vertical profiles to better translate the optical properties to ground-level PM concentrations.

Kriging techniques for PM assessment have also been explored recently (see Denby et al. 2008; Kloog et al. 2011; de Kassteele and Velders 2006; Pearce et al. 2009, for instance), but the results are context-specific and the performances of kriging geostatistics still need to be further analysed, especially for daily mapping with high-resolution remote sensing, and over different topography profiles. They offer higher capabilities of prediction for spatial phenomena with respect to the simple regression models, and still do not require such expensive hardware resources as more complex dispersion models would.

3.2 Kriging predictions

Kriging interpolation represents a good trade-off between the theory match with reality, data inputs, hardware resources and expert personnel required. It creates a statistical model on the available pollution and (possibly) ex-

planatory variables with knowledge of their geographic location and their (cross-)correlations, then predicts the filled map (see Fig. 3.2), assigning statistical uncertainty to each estimated location.
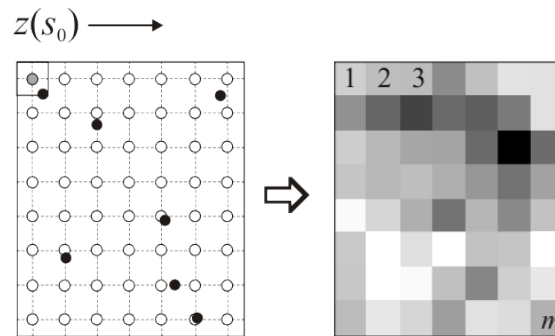
Fig. 3.2 – Kriging interpolates input measurements (black points) modeled as a stochastic variable $Z \sim \mathcal{N}$ onto a regular grid (white points) which are then usually visualized as pixels of a map; the resolution of the pixels might be different from their support. Picture courtesy of Tomislav Hengl.

Giving the error structure of the estimates is actually a feature which distinguishes kriging (and model-based geostatistics in general) from both empirical interpolators and more complex dispersion models; it can be useful to either compute confidence intervals for threshold exceedances, or to visually see which areas of the output prediction are less certain (intuitively areas far away from the available inputs).

With respect to simple mechanical interpolator — like inverse distance weighting, nearest neighbour, splines, Thiessen polygons — kriging estimates the value at the new unobserved location in an objective way, following probability theory. Validation or cross-validation procedures can also be easily computed against the input concentrations measurements.

Kriging can be run in ordinary machines with relative low computational resources[6] and with free software, as with `R` packages like `geoR` (Ribeiro Jr and Diggle, 2001) and `gstat` (Pebesma, 2004).

---

[6]Few minutes of computation on Intel(R) Core(TM)2 Duo CPU P8600@2.40GHz with 6 GB of RAM, for a kriging prediction onto a grid of $\sim$ 8e+04 points.

Kriging interpolation works well in case the statistical assumptions are met, and in case there is a sufficient number of unclustered target observations, so that the spatial pattern (covariances) can be described with statistical significance and with sufficient level of detail relatively to the spatial gradients of variation of the target variable, PM_{10} in our case. It should be noted that a small sample size may result in poor variogram models which might even produces worse estimates than simpler methods; moreover, depending on the layout of the inputs and on the statistical assumptions, kriging improvement in accuracy over other weighting methods can also be insignificant (Mulugeta, 1996).

As many other interpolation techniques, kriging involves linear combinations of neighbouring measurements, sharing thus the inherent limitations of such methods, i.e. weaker performances at the edges of the area of interest, adverse affection of both clustered input data, whose statistics may not be representative of the exhaustive dataset (population parameters), and outliers (Genton, 1998).

Following the universal model of spatial variation (Matheron, 1969), the target random *stationary* process Z can be modeled as the sum of a global trend μ (first-order effects), measuring broad trends in the data over the entire study, and a local stochastic variation (second-order effects) ϵ, possibly autocorrelated in space:

$$Z(\mathbf{s}) = \mu(\mathbf{s}) + \epsilon(\mathbf{s}) \tag{3.1}$$

being $\mathbf{s}$ the vector of spatial coordinates. Different assumptions on the global trend μ determine different type of kriging methods: *simple* kriging assumes $\mu = 0$, *ordinary* kriging assumes unknown constant mean, *universal* kriging assumes a general polynomial trend. The single prediction $\hat{z}_{s_0}$ at location s_0 can be expressed as:

$$\text{estimate} = \hat{z}_{s_0} = \sum_{i=1}^{N} w_{s_i} \cdot z_{s_i} \tag{3.2}$$

being z_{s_i} the N neighbouring observed values of the target variable (outcomes of Z) at locations s_i, each having its associated weight w_{s_i}, which are usually standardised so that they sum to 1.

What differentiates kriging from ordinary interpolators is the statistical theory behind the assignment of the weights w_{s_i}, which are computed in order to minimize the estimated variance of the residuals σ_r^2 — or *kriging error* — of the prediction (not to be confused with the variance of the prediction$s$). The following equations show the value and first derivative equation of σ_r^2 (minimization via Fermat's theorem):

$$\sigma_r^2 = \text{Var}\left(\hat{z}_{s_0} - z_{s_0}\right) \tag{3.3}$$

$$= \sigma^2 + \sum_{i=1}^{N} \sum_{j=1}^{N} w_{s_i} w_{s_j} \tilde{C}_{s_{ij}} - 2 \sum_{i=1}^{N} w_{s_i} \tilde{C}_{s_{i0}} \tag{3.4}$$

$$\frac{\partial \sigma_r^2}{\partial w_{s_{\tilde{i}}}} = 2 \sum_{j=1}^{N} w_{s_j} \tilde{C}_{s_{\tilde{i}j}} - 2 w_{s_{\tilde{i}}} \tilde{C}_{s_{\tilde{i}j}} = 0 \tag{3.5}$$

where $\tilde{C}_{s_{ij}}$ is the covariance between two samples ($\text{E}[(z_{s_i} - \mu)(z_{s_j} - \mu)]$). Minimization of the variance of the errors, together with the unbiasedness constraint on the residuals ($\sum_i w_{s_i} = 0$), is what makes kriging the Best Linear Unbiased Estimator (BLUE). From Eq. 3.4 we can then derive the so-called kriging system:

$$\mathbf{D} = \mathbf{C} \cdot \mathbf{w} \tag{3.6}$$

$$\begin{bmatrix} \tilde{C}_{s_{10}} \\ \tilde{C}_{s_{20}} \\ \vdots \\ \tilde{C}_{s_{N0}} \\ 1 \end{bmatrix} = \begin{bmatrix} \tilde{C}_{s_{11}} & \tilde{C}_{s_{12}} & \cdots & \tilde{C}_{s_{1N}} & 1 \\ \tilde{C}_{s_{21}} & \tilde{C}_{s_{22}} & \cdots & \tilde{C}_{s_{2N}} & 1 \\ \vdots & \vdots & \ddots & \vdots & \vdots \\ \tilde{C}_{s_{N1}} & \tilde{C}_{s_{N2}} & \cdots & \tilde{C}_{s_{NN}} & 1 \\ 1 & 1 & \cdots & 1 & 0 \end{bmatrix} \cdot \begin{bmatrix} w_{s_1} \\ w_{s_2} \\ \vdots \\ w_{s_N} \\ \lambda \end{bmatrix} \tag{3.7}$$

from which then the kriging weights w_{s_i} are determined ($\mathbf{w} = \mathbf{C}^{-1} \cdot \mathbf{D}$). Note the Lagrange parameter λ that constraints the minimization of the error to unbiasedness. Taken by itself, the $\mathbf{D}$ vector provides a weighting scheme which is similar to that of the inverse distance method: as the covariance decreases as the samples gets further away, $\mathbf{D}$ replaces the geometric distance with statistical distance instead. The role of $\mathbf{C}$ on the other hand is to adjust the inverse distance scheme in $\mathbf{D}$ to account for clustering in the available sample data, therefore customizing the estimation procedure to the particular pattern of spatial continuity.

The covariances are retrieved from a **variogram**, which models the spatial autocorrelation of the target variable — in terms of *semivariances*[7] $\gamma_{s_{ij}} = \sigma^2 - \tilde{C}_{s_{ij}}$ — by the relative distance h between locations s_i and s_j:

$$\gamma(h) = \frac{1}{2}\mathrm{E}\left[(z_{s_i} - z_{s_i+h})^2\right] \tag{3.8}$$

The variogram model (see Fig. 3.3a) is described by: the *nugget* (C_0), representing the measurements error and short-distance spatial variations; the

---

[7]Covariances are used in place of the semivariances for the weights computation (remember Eq. 3.7) because this way the largest elements of the $\mathbf{C}$ matrix will be on the diagonal, thus avoiding pivoting on Gaussian elimination for $\mathbf{C}$ inversion.

(total) *sill*[8], i.e. the variance of the variable of interest; the *range*, which defines the distance up to which there is spatial autocorrelation, which is usually defined as the lag distance at which semivariance is close to 95% of the total sill: $\gamma(h) \approx 0.95 \cdot \gamma(\infty)$.
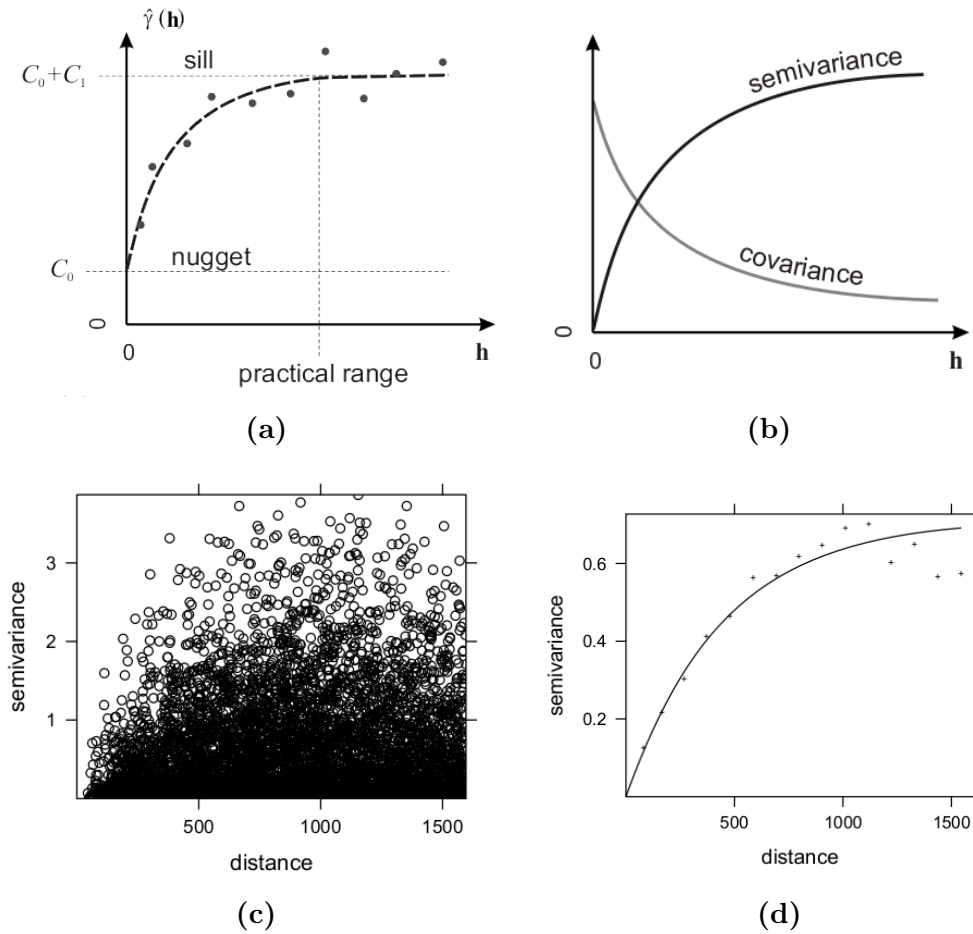
Fig. 3.3 – Different concepts of the variogram: (a) variogram's parameters visual definition; (b) the relationship between semivariances and covariances; (c) the variogram cloud showing semivariances for all pairs of input points; (d) the variogram model fitted over the lagged averages (+) of the variogram cloud. Pictures courtesy of Tomislav Hengl.

The estimation of the variogram models starts with the computation of the semivariance between every possible pair of values in the area of interest (variogram cloud, Fig. 3.3c), whose values are then averaged over spatial bins or

---

[8]Which is the sum of the nugget and the *partial* sill (C_1).

lags (sample variogram) and then fitted (variogram model, Fig. 3.3d). To
ensure that the kriging system has unique and numerically stable solution we
must observe the positive-definiteness constraints[9], which in practice guar-
antees that the random variable at any unobserved location s_0 computed
by linear combinations of the other random variables, has positive variance.
This means that the variogram model cannot be fitted with a simple inter-
polation of the points, but there is a set of allowed models (e.g. Gaussian,
spherical, exponential); refer to Armstrong and Jabin (1981) and Cressie
(1985) for further details.

Summarizing, the variogram model is computed a priori of the prediction,
and serves as mapping function to derive covariances between the available
points[10], and as well between them and the unobserved location; these co-
variances fill the matrices $\mathbf{C}$ and $\mathbf{D}$ (Eq. 3.6) which then are used to find the
weighting scheme of the linear combination (Eq. 3.2). The prediction repre-
sents the optimal value of a stochastic variable — its mean — which actually
is shaped by a probability function: sometimes, when a possible *reality* is to
be generated in place of the smoothed model, then stochastic Gaussian sim-
ulations are usually run over the data, by choosing a random value along the
density function of the predicted value. This procedure allows to visualize
more realistic estimations, though it requires much longer prediction times.

As a final note on the kriging estimation, in order to coherently represent
an output map it is usually preferred to match the output resolution to the
support which the prediction represents: this means that the spatial area
associated with a prediction by the model should be equal to the actual
area of the pixel. Until now, the sample data were *points* of the target
variable (namely, the PM concentrations measured by the ground stations),

---

[9]Being $\mathbf{K}$ the $(N+1)\times(N+1)$ matrix of the whole set of covariances between the point
at the unobserved location and the neighbouring available points, the positive-definiteness
constraint ensures that $\mathbf{w}^T\mathbf{K}\mathbf{w} > 0$, for any $(N+1)$-dimensional vector $\mathbf{w}$.

[10]The search radius is usually limited to a certain *cutoff* distance, for lighter matrices
inversions, and as well to exclude from the prediction samples which are too far away and
may not be appropriate under stationary assumptions.

and the estimations had point support too: the very correct visualization of such predictions would be by means of points, and not of pixels. An areal estimation is instead done by computing **point-to-block covariances**, which under stationarity assumptions are expressed as:

$$\tilde{C}_{s_{iA}} = \frac{1}{|A|} \sum_{j \in A} \tilde{C}_{s_{ij}} \tag{3.9}$$

being A the block of area $|A|$. Thus, by estimating predictions averages over square (*blocks*) then we can achieve the desired support/resolution match. Averaging values together over larger areas generally has the effect of reducing the variance the data, along with associated uncertainty, especially when there is a strong nugget effect: near-distance noise is indeed diluted into the block.

For an exhaustive introduction to kriging interpolation see Isaaks and Srivastava (1989) or Diggle et al. (2002). For the application of kriging in R, refer to Pebesma (2004). Until now, kriging has involved the one target variable: the ground measurements of PM_{10}. In order to include the AOT information from satellite we must extend the interpolation to a multivariate case: the following sections (Sec. 3.2.1 and Sec. 3.2.2) will describe how to manage such situations by means of kriging techniques.

3.2.1   Cokriging

Whereas kriging interpolation takes the input values of the target *primary* variable, cokriging allows to insert one or more *secondary* variables into the weighting process, being able to bring considerable predicting gain with respect to ordinary kriging (Ver Hoef and Barry, 1998). It is especially designed for cases in which the secondary variables are not available throughout the

output grid of prediction, and yet are sampled more intensely than the target measurements (Stein and Corsten, 1991).

Using cokriging obviously makes sense when the secondary variables are somehow *explanatory*, so that their inclusion can help to reduce the variance of the kriging error. The estimate in this case extends Eq. 3.2 to include the T auxiliary variables $v^{(t)}$:

$$\text{estimate} = \hat{z}_{s_0} = \sum_{i=1}^{N} w_{s_i} \cdot z_{s_i} + \sum_{j=1}^{M_1} \beta_{s_j}^{(1)} \cdot v_{s_j}^{(1)} + \ldots + \sum_{k=1}^{M_T} \beta_{s_k}^{(t)} \cdot v_{s_k}^{(t)} \quad (3.10)$$

The system then must be able to compute the weighting coefficients $\beta^{(t)}$ associated with the variables v, in addition to the coefficients w_{s_i} which refer to the primary variable z. It should be noted that the secondary variables can have their own independent spatial layout, allowing cokriging to effectively "add apples and oranges" (Cressie and Wikle, 1998).

The underlying statistical model is now based on the $t + 1$ variograms for each of the variables involved, and on the $\binom{t+1}{2}$ cross-variograms, which intuitively describe the semivariance of a variable with respect to a second variable, with increasing distance. Fitting the (cross-)variograms' models altogether simultaneously (under positive-definiteness conditions) is known as *coregionalisation*. This is not done univocally, there are different methods: usually the easiest (though less flexible) is the *linear* model of coregionalisation, which fits the sills and nuggets while assuming the same model and range for all the variograms. The cokriging system can then be extended from Eq. 3.7 this way (simple case $T = 1$, then $v^{(1)} = v$ and $M_1 = M$):

$$\begin{bmatrix} \mathbf{D}_z \\ \mathbf{D}_{zv} \\ \mathbf{1}_N \\ \mathbf{0} \end{bmatrix} = \begin{bmatrix} \mathbf{C}_z & \mathbf{C}_{zv} & \mathbf{1}_N & \mathbf{0} \\ \mathbf{C}_{zv}^T & \mathbf{C}_v & \mathbf{0} & \mathbf{1}_M \\ \mathbf{1}_N^T & \mathbf{0} & \mathbf{0} & \mathbf{0} \\ \mathbf{0} & \mathbf{1}_M^T & \mathbf{0} & \mathbf{0} \end{bmatrix} \cdot \begin{bmatrix} \mathbf{\Omega} \\ \mathbf{\Theta} \\ \mathbf{\Lambda}_z \\ \mathbf{\Lambda}_v \end{bmatrix} \tag{3.11}$$

where $\mathbf{C}_z$ and $\mathbf{C}_v$ are the $N \times N$ and $M \times M$ matrices of the covariances, $\mathbf{C}_{zv}$ is the $N \times M$ matrix of the cross-covariances, $\mathbf{D}_z$ and $\mathbf{D}_{zv}$ are the N- and M-dimensional column vectors of the (cross-)covariances with respect to the unobserved location. $\mathbf{1}$ and $\mathbf{0}$ are column vectors, and, as similarly done in Eq. 3.7, they are required to include the unbiasedness conditions in the system by means of the Lagrangian multipliers $\mathbf{\Lambda}_z$ and $\mathbf{\Lambda}_v$, which are[11]:

$$\begin{cases} \sum_{i=1}^{N} w_i = 1 \\ \\ \sum_{j=1}^{M} \beta_j = 0 \end{cases} \tag{3.12}$$

For in-depth material on cokriging, refer to Myers (1982); for the implementation of cokriging in R, see Rossiter (2007).

3.2.2 Kriging with regression

A key factor in a cokriging system relies in the coregionalisation of the statistical models of the different variables. The linear model of coregionalisation (see Sec. 3.2.1) can be limiting when the direct- and cross-variograms need *different* models for an optimal fit, or when the variables show different ranges of spatial variation. In addition, the mathematical constraints of the

---

[11]Eq. 3.12 shows the most commonly used unbiasedness conditions for 2-variate cokriging, but other analogous conditions might be used as well, e.g. $\sum_i w_i + \sum_j \beta_j = 1$.

coregionalisation for a positive-definite system might shift the fitted models away from the experimental points in the sample variograms.

When the auxiliary variables are available on the whole grid of output predictions, then universal kriging — also known as kriging with external drift, regression-kriging or kriging combined with regression[12] — is generally preferred (Knotters et al., 1995). Universal kriging establishes the deterministic part of the variation of Z ($\mu(\mathbf{s})$, see Eq. 3.1) by means of regression, then adjusts the trend surface by modelling the spatial pattern of the residual with a variogram, as explained in Fig. 3.4.
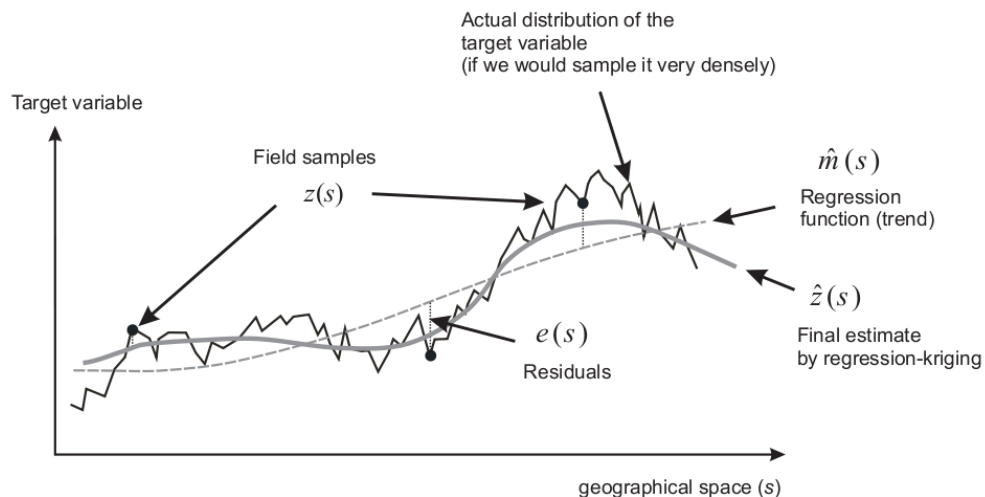
Fig. 3.4 – 1D example schema of kriging with regression. Picture courtesy of Tomislav Hengl.

The kriging system then is again univariate, but it is evaluated on the stochastic residuals of the random target variable: the auxiliary variables are instead moved into the regression model, thus into a linear combination with least square weighting:

---

[12]Many authors agree that *universal kriging* should be used in case the trend is modeled as a function of the coordinates, whereas *kriging with external drift* is used when the trend is defined externally through some auxiliary variables (Wackernagel, 1996). *Regression-kriging* implies to fit trend and residuals separately, then summed together: mathematically these methods are equivalent (Hengl et al., 2003).

$$\text{estimate} = \hat{z}_{s_0} = \mu(\mathbf{s}) + \epsilon(\mathbf{s}) \tag{3.13}$$

$$= \sum_{k=1}^{M} \beta_k \cdot v_{s_0}^{(k)} + \sum_{i=1}^{N} \alpha_i \cdot e_{s_i} \tag{3.14}$$

where β_k are the M regression coefficients for the M explanatory variables $v^{(k)}$, and α_i are the kriging coefficients of the regression residuals e_{s_i}. Where in cokriging the information of the covariates was induced by combining the kriging-weighted neighbouring observations, in regression-kriging the observations of secondary variables are selected only in s_0, to define the expected value which will be then adjusted by the spatial autocorrelation of the neighbouring residuals.

These concepts could be applied in a practical prediction of PM by means of AOT as a regressor $v^{(k)}$, even though there is an important consideration to be done first: the availability of AOT data is very rarely complete on a certain area of interest (e.g. due to clouds); thus using the maps of spaceborne AOT to feed a regression on the PM concentrations is still undoable provided that a preliminary interpolation is carried out. This way the uncertainty on the input is increased and the applicability of the model is limited to those days where unavailability of the data is prohibitively high.

For further reading on kriging combined with regression and its implementation in `R`, see Hengl (2009) and Hengl et al. (2004).

3.2.3   Spatio-temporal kriging

Methods analysed until now are involving pure spatial analysis, with no memory in time: particulate matter can have however also a temporal correlation

([Turner and Allen](#), 2008), for example in case of prolonged and fixed sources of emission, independently of the gradient of spatial heterogeneity.

From a statistical point of view, dealing with time series of datasets observations in time present different representational issues from those in space and need special treatment. The complexity of the predictor increases as well, since *mixed* spatio-temporal processes are not easily accessible, and several different models can be used to approximate the phenomenon. Additional care on the different supports of the data must be taken as well ([Gotway and Young](#), 2002).

Time has the special property of one directional flow: clearly the state of a process in a certain moment in time cannot affect what already happened before. Additionally temporal processes usually show a different pattern forward than backward in time: e.g. in case of a sudden exposure of some toxic, its concentration would suddenly rise but the decay would proceed slowly. In this case the probability of observing a low value followed by a high one is higher than the probability of observing a low one after a high one ([Gräler et al.](#), 2012).

Extending Eq. [3.1](#) to a spatio-temporal process, in the most general case the situation could be represented this way:

$$Z(\mathbf{s}, \mathbf{t}) = \mu_s + \mu_t + \mu_{st} + \epsilon \tag{3.15}$$

This means that generally there can be a spatio-temporal interactions (μ_{st}), and the spatial and temporal components might not be modeled separately. Additionally the metrics and, as said, the directionalities are different.

Similarly, the semi-variance which is observed within a spatio-temporal process can be extended from Eq. [3.16](#):

$$\gamma(h, \Delta) = \frac{1}{2}\mathrm{E}\left[(z_{s_i, t_i} - z_{s_i+h, t_i+\Delta})^2\right] \qquad (3.16)$$

being Δ the lag in time of the 3D variogram surface. Having a sequence of spatial observations in time, there are different ways to account for them and their interactions.

The method described in the previous section for instance already accounted for temporal evolution of the data by computing separate models for each day: this way the whole data available is used, but for each day the observations of *that* day were used, no interactions were incorporated.

As an additional sophistication, one could add an historical base to the variogram evaluation by basing the starting values of nugget, sill and range on the previous day model. In this case the variograms would roughly account for the temporal interaction, but would also result in a more stable variogram fit for the days with high noise (prevailing nugget effect).

Collecting the *whole* available data to reproduce a one **pooled** variogram is an other option: the model is fixed for a selected interval of time, but relies on more data; still spatio-temporal interactions are not modeled.

Alternatively, by properly scaling the time scale, one could extend the 2D geographical space to a 3D spatio-temporal one: this technique is called **metric kriging** and although on one side if merges the spatial and the temporal processes, on the other side it forces a unique variogram model (e.g. Gaussian) and treats all distances in the same statistical way, which as we discussed is unlikely. This method has been however successfully applied, as done in Hengl et al. (2012).

A real spatio-temporal variogram however must treat spatial and temporal distances (Hengl et al., 2012), by means of a spatio-temporal covariance

function which can be usually modeled as:

separable covariance function

> In this case the covariance can be expressed as the product of due distinct components which separately depend on the spatial distance and on the temporal distance: $C(h, \Delta) = C_S(h) \cdot C_T(\Delta)$;

product-sum covariance function

> Simplified assumptions of the separable model are here extended to a more complex but flexible one: $C(h, \Delta) = k_1 C_S(h) \cdot C_T(\Delta) + k_2 C_S(h) + k_3 C_T(\Delta)$, being k_1 not null.

Meshing space and time models is evidently a huge challenge: it gives the potential to capture day-by-day variance in the spatial surfaces, but the co-variances might be difficult to interpret conceptually (Liu et al., 2009). The `spacetime` package is showing more promise in the R scenario (Pebesma, 2012), and that was actually used to run the predictions. While the product-sum covariance model for spatio-temporal predictions is still under construction, all the other described kinds of analysis are possible within that package. More details on the adopted method and final results will be presented in Sec. 4.3.2.

3.3 Web mapping and Web-based analysis of the results

When treating spatial data, visualization is a key aspect of the whole frame-work, together with data collection and storage, geostatistical modelling and prediction. A flexible, Web-accessible visualization system can greatly help the geostatistician to analyse the performances of the adopted estimator, identify areas with higher uncertainties on customizable temporal intervals

(e.g. different seasons), or retrieve post-processed maps against the interpolated output data (which normally includes mean-value predictions and related uncertainty in the form of standard error or prediction variance, a full conditional probability distribution, or probabilities of exceeding a certain threshold).

In order to do so in a standardised and general way, a system has been designed to let an end-user store/access/process its input and output maps onto a proper architecture, depicted in Fig. 3.5, which includes:

- an open-source DataBase Management System (DBMS) for the storage of n-dimensional raster datasets as multidimensional indexed arrays, and for the retrieval and processing of the data with a SQL-style query language rasdaman, namely the `rasql` interface language for `rasdaman` (see RASter DAta MANager (rasdaman) 2009 and Baumann 2011);

- a Web interface of the above mentioned DBMS storage by means of an OGC[13]-compliant servlet application, namely PetaScope (Aiordăchioaie and Baumann, 2010), which can intermediate between the end-user geocoded request and the local pixel-based `rasql` query language;

- the GIS software (e.g. `R`) for the actual geostatistical estimation, which may take the data inputs from preliminary fetched rasters (or either directly from the Web service) and will produce the statistical output, which in turn can be added to the DBMS for the visual (Web-based) analysis.

There are multiple advantages that can derive by the adoption of such a framework. In first place, what more closely can involve the support to a geostatistician is the flexible visualization of the resulting maps: generally

---

[13]The Open Geospatial Consortium (OGC) is an international industry consortium of 472 companies, government agencies and universities participating in a consensus process to develop geo-enabling interface standards.
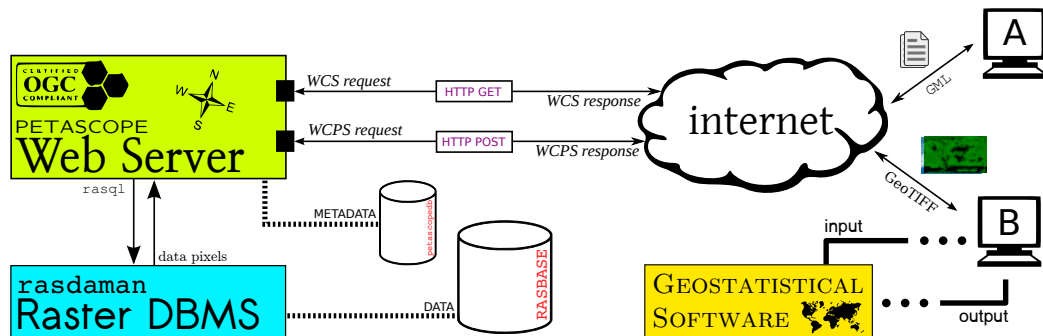
Fig. 3.5 – Framework of the proposed schema for geodata analysis and visualization, in a Web-based scenario: OGC services can be used to select subsets of interest within the datasets; in particular, WCPS extended capabilities could be used for spatial or temporal aggregation techniques of the inputs or to retrieve exceedances maps with custom confidence intervals of geostatistical predictions.

an interpolation technique for environmental modelling is run over a certain area of interest and for a specified interval of time, in order to test the method for different seasons, climatic and atmospheric, conditions, and so on; so as to evaluate the interpolation in an objective manner. For instance, by storing the output predictions as two spatio-temporal series of rasters — one for the predictions and one for the uncertainty — one could retrieve and visualize arbitrary subsets of the whole datasets, by using Web Coverage Service (WCS, OGC 2010) requests like to following:

```
http://<host>[:<port>]/petascope?
    service=WCS&
    version=2.0.0&
    request=GetCoverage&
    coverageid=PM10-latlon-Europe_KRIGING_ERROR&
    subset=Long(15,16)&
    subset=Lat(50,51)&
    subset=t(2010-06-12)&
    format=image/geotiff
```

which selects the rectangular area between $15\,°E - 50\,°N$ and $16\,°E - 51\,°N$ from the time series of kriging error maps called "PM10-latlon-Europe_KRIGING_ERROR"

on the 12th June 2010, taking the result as a GeoTIFF image. Familiar geographic coordinates (latitude and longitude) could be used for convenient subsettings also in case the maps were stored in a projected Coordinate Reference System (CRS), like the commonly used Universal Transverse Mercator (UTM):

```
http://<host>[:<port>]/petascope?
    service=WCS&
    version=2.0.0&
    request=GetCoverage&
    coverageid=PM10−utm−Europe_KRIGING_MEAN&
    subset=x(15)&
    subset=y(45)&
    subset=t(2010−06−12)&
    subsettingcrs=http://<resolver>/def/crs/EPSG/0/4326&
    format=image/geotiff
```

By explicitly specifying the CRS used in the subsets, the Web servlet is able to transform them to native coordinates and, afterwards, to retrieve the data from the DBMS. Output reprojection is also foreseen by means of an additional parameter `outputcrs`, for example in case the output of two different models on the same area with possibly different CRS projections needs to be spatially synchronized for visual comparison.

It must be noted that subsettings could be exploited as well to temporarily retrieve a cutout of a wider remote dataset into local disk, for time and storage savings; moreover `R` still has no native memory handling for huge datasets, although the `raster` package can be installed for clever tiled access and management of raster images (Robert J. Hijmans & Jacob van Etten, 2012).

The URL notation of the CRS (instead of the classic *authority:code* notation), has been used: indeed, behind e.g. http://kahlua.eecs.jacobs-university.

`de:8080/def/crs/EPSG/0/4326` the server fetches a Geographic Markup Language (GML, OGC 2007) definition which describes a geographic (unprojected) 2-dimensional CRS over the WGS84 datum with unit of measure in degrees of latitude and longitude. The content of a CRS is thus always analysed by the server, so that customized or non-ordinary definitions can be used and binded with the data, such as for planetary datasets (Oosthoek et al., 2013). This way the server's database of metadata is more lightweight, being the CRS metadata moved away to the remote resolver of the definitions. Concatenation of different reference systems (beyond spatial) can be done, so that spatio-temporal datasets and n-dimensional cross-sections can be retrieved, in a seamless way. More details on this proposed architecture are found in Baumann et al. (2012) and Misev et al. (2012).

Extending the capabilities of WCS, which only relates to data visualization, one could also visualize a post-processed version of the output maps. It is the case for instance of retrieving exceedances map over a certain threshold and with arbitrary confidence intervals, or when either spatial or temporal averages are to be visualized. The Web Coverage Processing Service (WCPS, Baumann 2010 and OGC 2009) is a protocol-independent language for the extraction, processing, and analysis of multi-dimensional gridded coverages, similarly to the WCS service but with the additional capability to run some basic arithmetics on the available data. For instance, taking our spatio-temporal series of PM data again as an example, one might be interested in the average of the output values in January 2010 (temporal aggregation) over a specified location and read the values as comma-separated values:

```
for pm10 in (PM10−latlon−Europe_KRIGING_MEAN)
   return
      encode(
         avg( pm10[Long(17),Lat(49),
                  t("2010−01−01":"2010−01−31")] ),
      "csv")
```

By exploiting both the information in the kriged values and uncertainties, one could retrieve and visualize exceedances maps of the pollutant concentrations with an arbitrary confidence interval: these are generally required by local authorities. Indeed, interpolation always brings error on the unobserved locations, behind each predicted pixel there are whole distributions, whose width is proportional to its uncertainty: just looking at the mean values is not enough, and the error information needs to be taken into consideration. A WCPS query could compute this kind of maps on-the-fly from the raw data, hence without the need to store additional datasets. For instance, in case we want the maps of PM_{10} exceedances of the threshold 50 µg/m^3 with 95%[14] of confidence:

```
for pm10−value in (PM10−latlon−Europe_KRIGING_MEAN),
    pm10−error in (PM10−latlon−Europe_KRIGING_ERROR)
  return
    encode (
      (pm10−value + pm10−error∗1.644854) > 50,
    "png")
```

Which will return a black and white picture of map exceedances. Temporal aggregation, or spatial subsettings could be also combined, to set the focus on more specific features of the predicted maps.

This architecture is proposed in the outlook of going towards an automated on-line mapping systems. The amount of field and remotely sensed data is increasing. However, there is an increading need for systems that can reliably provide information to local authorities and decision makers, in real-time. Automating the production of environmental maps along with on-line availability is thus highly required as well to bring international groups together and start "piecing together a global jigsaw puzzle" to enable production of a global harmonized GIS of all environmental resources. A first step into this

---

[14]$\Phi(z) = P(Z \leq z) = (1 - \alpha) = 0.95 \longrightarrow z = \Phi^{-1}(z) = \sqrt{2} \cdot erf^{-1}(2 \cdot 0.95 - 1) \simeq 1.644854$

direction is for example the INTAMAP project (Pebesma et al., 2009); other projects are still in development (e.g. *auto-map.org*).

Chapter 4

Models Performance and Overall Achievements

This chapter will comment on the outcomes of the three different models of PM_{10} that were developed during this study, with special remarks on the actual advantages that were (or were not) brought by the AOT information from satellite. All the models focused on the proper exploitation of the AOT maps from PM MAPPER (see Sec. 2.1.3) at 1×1 km^2 of nominal resolution.

A first application has been carried out over the Po Valley in Italy, a flat area right next to the Appennini, which is notoriously characterized by bad air quality conditions associated with low wind intensities and large industrial emissions. The results obtained from this study are reported in Sec. 4.2.

In the second place, the geographic area of interest moved to Austria, where the highly rugged topography and complex wind profiles make it a challenging case for air quality modelling. Meteorological model-based maps were available in addition to the aerosols columnar information in this case. Two different models were developed over this area, and they are described in

Sec. 4.3: a first model explored the spatial patterns and cross-correlation between the meteorological phenomena, the atmospheric aerosols and the particulate matter; the second analysis aimed at comparing kriging predictions when exploiting inter-days correlation aomng the data.

All the model runs produced side statistics metadata along with real output predictions (and uncertainty) with same resolution as the AOT maps ($1\,\text{km}^2$), so to exploit the level of detail offered by the high resolution spaceborne maps and which can be enough PM_{10} local (though not intraurban) level monitoring[1]. For the monitoring of other pollutants like SO_2, NO_2, $PM_{0.1}$ or CO, then consider that smaller scale spatial gradients could be diluted in such a resolution instead (Jerrett et al., 2004).

Before proceeding, a preliminary section relative to the *validation* of the satellite maps must be undertaken.

4.1   Validation of $1{\times}1$ km^2 AOT products

While PM MAPPER maps at $3{\times}3$ km^2 of resolution were validated by Nguyen et al. (2010a), the availability of a new product at further increased resolution, namely 1 km^2, gave a promise for smaller scale monitoring.

Before using these maps, it was necessary to carry out a dedicated validation test, which involved the comparison with calibrated uplooking measurements of aerosol optical thickness, whose uncertainty is small (order of 10^{-3}, Sec. 2.1.1), up to the point that they can be considered the *truth*. In particular, the AERONET network sites were selected for a 3-year validation over Europe of the new AOT datasets.

---

[1]Due to computer memory limitations, the maps for the spatiotemporal model had to be at the coarser resolution of $10{\times}10$ km^2.
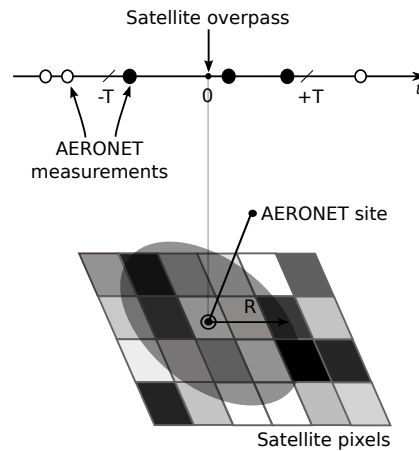
Fig. 4.1 – Matching a satellite map with a ground data segment: pixels near the ground station are cut out then averaged and compared with the temporal mean of the observations of the ground station itself, close in time to the satellite overpass time.

As pointed out by Ichoku et al. (2002), validation of satellite imagery with simple pixel-to-station comparison is not coherent: the pixel of AOT represents the spatial average[2] over the square of 1×1 km² of the PM MAPPER product and may not be legitimately equated with a sunphotometer. In case of an extremely high spatial resolution the pixel may well approximate a point (not our case), but still the two observations would have different axis of view and hence would rely on different atmospheric conditions. Furthermore, clouds may obscure a pixel directly over a sunphotometer site, but not nearby pixels. In addition, the satellite overpass times rarely coincide with the AERONET measurement. On average, several minutes separate the two acquisitions.

There are indeed several reasons for which it is far more appropriate to compare spatial averages from satellite pixels with temporal averages of AERONET ground truth: having airmasses constantly in motion, it is likely that the same airmass captured by a satellite over an AERONET site will be sampled by the sunphotometer during a certain time period. Fig. 4.1 gives a visual representation of the matching procedure.

---

[2]Actually, it is usually an approximation: some pixels in the box are discarded due to their extreme values and other non-ideal conditions, see Sec. 2.1.2.
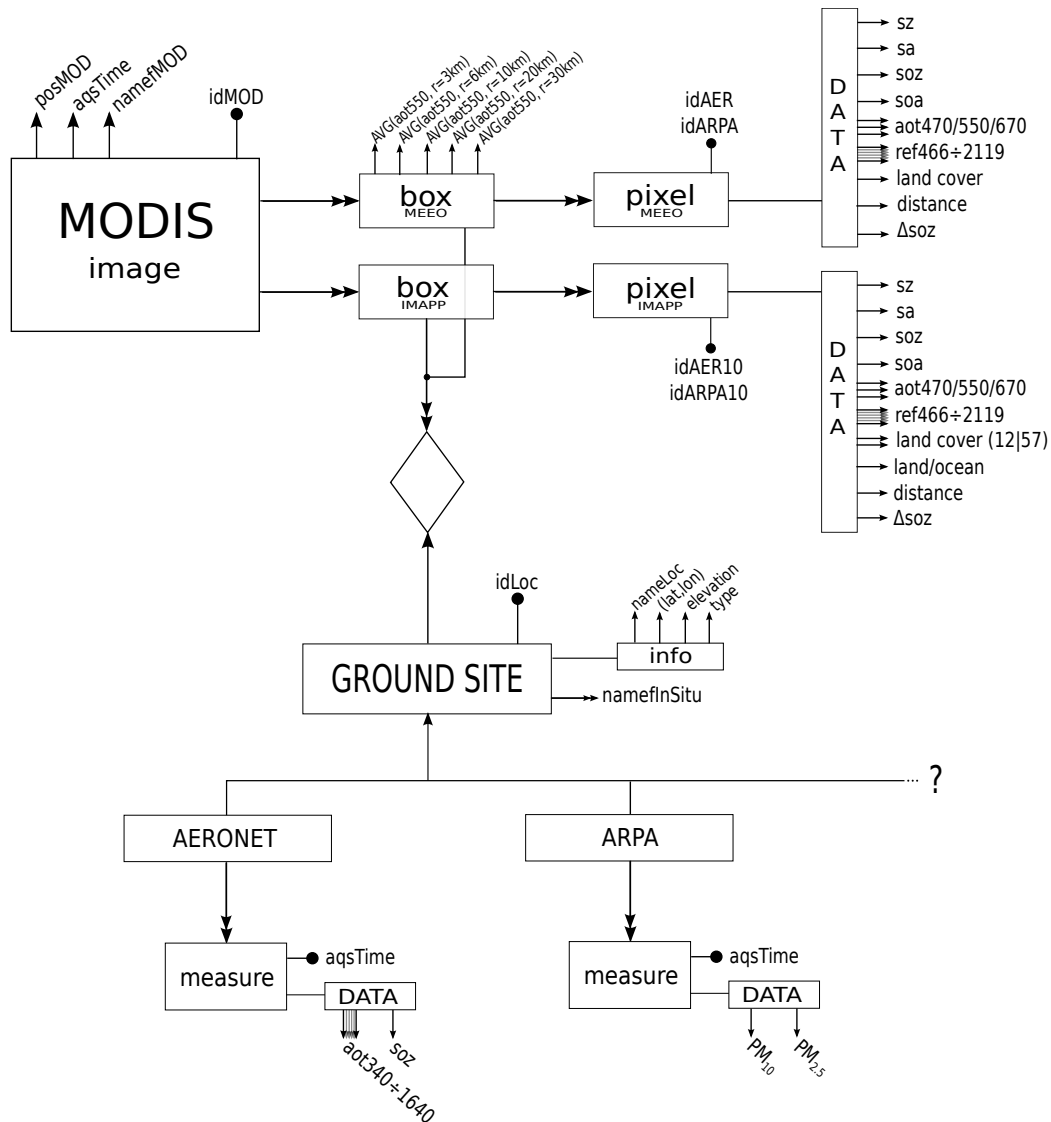
Fig. 4.2 – Entity-Relationship (ER) diagram of the database which was developed for the validation of the AOT products at 1 km². Detailed metadata of each pixel were also included for further analysis. PM$_{10}$ ground measurements from the ARPA air quality network were ingested for direct analysis on the AOT-PM relationship. Original MODIS AOT at $10{\times}10$ km² cutouts (IMAPP) were also stored, to compare the performances of the two spaceborne products.

Along with the validation, it was decided then to analyse the validation approach on different spatio-temporal averaging windows, trying to find an optimal match and to view the gradients of variability in the satellite-AERONET association through time and space. In order to do so, an ad-hoc database

was developed, with ground data linked to the circular cutouts of the satellite maps of AOT around each ground site. Fig. 4.2 shows the structure of this database.

With this underlying architecture, simple iterated SQL queries were required to evaluate the correlation of the spaceborne AOT averages with the ground AOT ones. The comparison was carried out on a discrete grid of spatial radii and temporal semi-intervals (see Fig. 4.3), then a 3D surface was fitted to it.
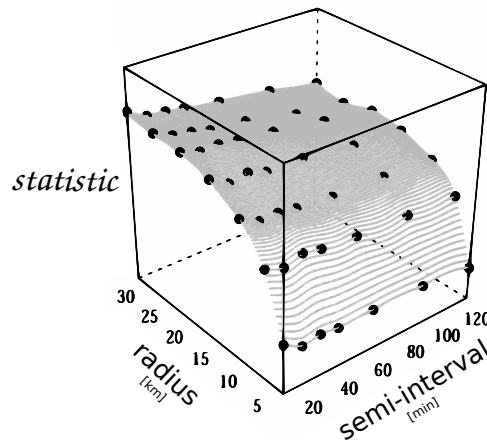
Fig. 4.3 – 3D surfaces template of validation statistics: fitting is done over the computed values (black points) obtained by varying the radius and semi-interval parameters of data selection.

The template figure shown in Fig. 4.3 was applied for analysis of precision, bias and correlation, for both IMAPP MODIS maps at 10×10 km² and PM MAPPER equivalents at increased resolution.

The evaluation of the produced validation surfaces (see Figs. 4.5, 4.6 and 4.7), revealed a best case scenario with regards to the coupling parameters to be chosen: matching the spaceborne pixels within 20 km from the uplooking photometer with ground measurements not later nor earlier than 10 min from the satellite overpass optimized the ground/space AOT match, with statistical significance (see 4.4).
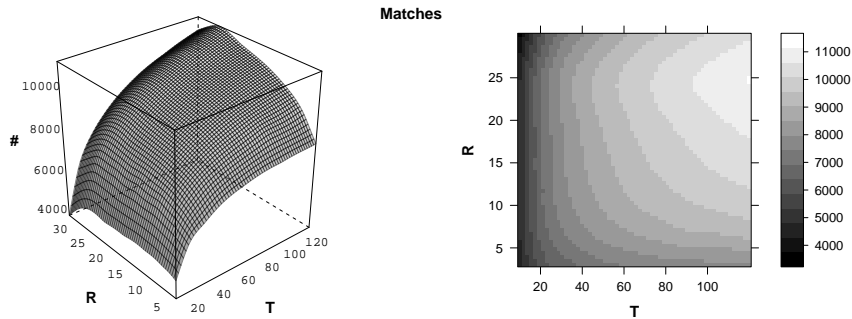
Fig. 4.4 – (Fitted) spaceborne AOT validation surfaces: horizontal axes composed of radius R of map cutout and semi-interval T for AERONET temporal series delimitation around satellite overpass; the number of satellite-sunphotometer matches on the z axis.
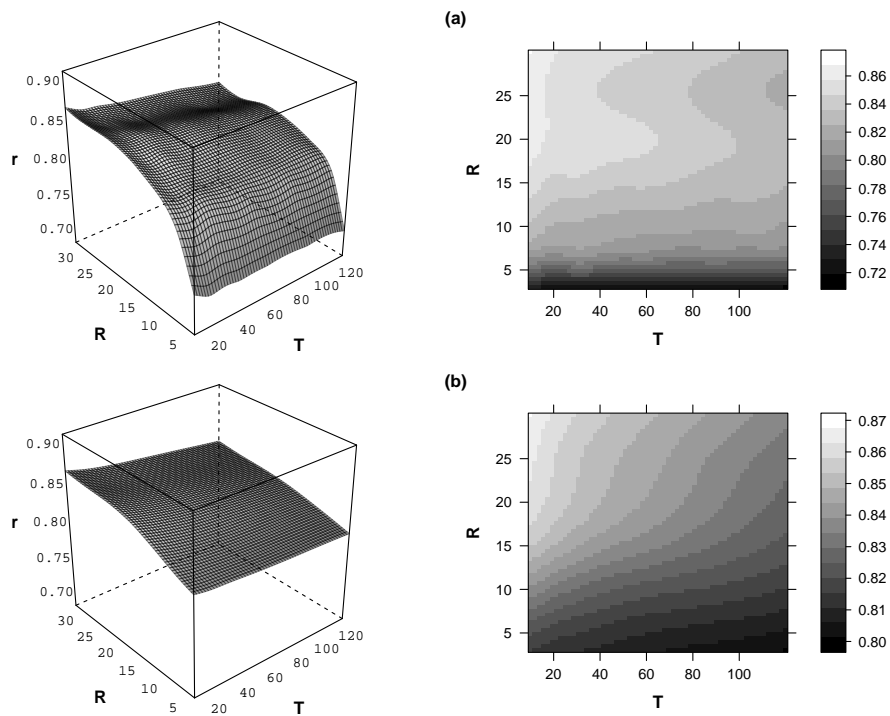
Fig. 4.5 – (Fitted) spaceborne AOT validation surfaces: horizontal axes composed of radius R of map cutout and semi-interval T for AERONET temporal series delimitation around satellite overpass; the Pearson's linear correlation coefficient on the z axis.

The details regarding this *best-case* validation are shown in Fig. 4.8: PM MAP-PER and IMAPP MODIS maps both show a stable correlation (> 0.86) with

Fig. 4.6 – (Fitted) spaceborne AOT validation surfaces: horizontal axes composed of radius R of map cutout and semi-interval T for AERONET temporal series delimitation around satellite overpass; the absolute mean error [µg/m³] on the z axis.

the ground truth. This was a fundamental result for the overall success of the validation, since the AOT outcomes of the former could be retained sufficiently in accordance with the observations from sunphotometers, and also not degrading the quality offered by the IMAPP retrieval algorithms.

An additional look to the result gave some more insight on the AOT inversions: the Quantile-Quantile plot reveals how AOT tends to be overestimated by MODIS for high values (> 0.5), while PM MAPPER seems to introduce a small positive bias for a wider range of AOT values (> 0.1). This is probably due to the higher noise which is inevitably added to pixels that base their AOT ratio on a smaller number of reflectance pixels.

Looking again at Fig. 4.8 one can catch that PM MAPPER retrievals are slightly more biased than MODIS (0.036 to 0.024), whereas the slope (0.97)
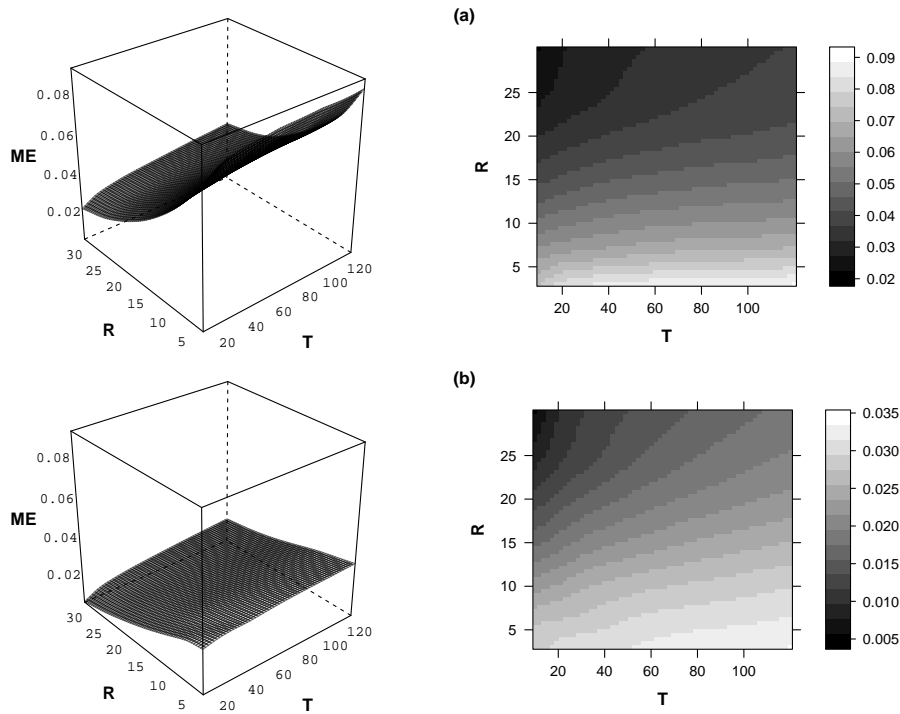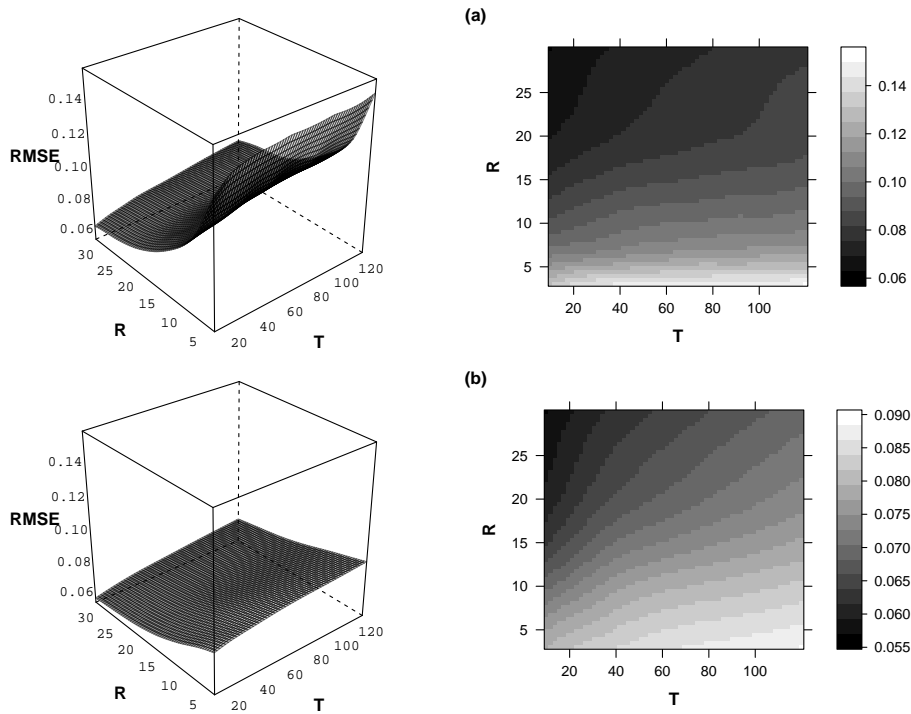
Fig. 4.7 – (Fitted) spaceborne AOT validation surfaces: horizontal axes composed of radius R of map cutout and semi-interval T for AERONET temporal series delimitation around satellite overpass; the root mean square deviations $[(\mu g/m^3)^2]$ on the z axis.

is quite closer to unity than the original M?D04 products (0.927). These differences are not very strong and it would be daring to draw clear conclusions from them.

Analytic details of the validation are also presented in Tab. 4.1, along with further results that were extracted to observe the inter-year variability, seasonality and land-cover affection: as expected (Prasad and Singh, 2007), AOT retrieval from satellite worked better over dark vegetated lands, where there is less uncertainty in the perceived reflectances (RMSE of 0.052, on rangelands was instead 0.076); better match with AERONET was also found during cold months, but a comparison of statistic might be compromised because of the exclusion of a lot of matches (reduced to less than the half of the matches in the Summer season), mainly caused by snow and cloudy pixels.
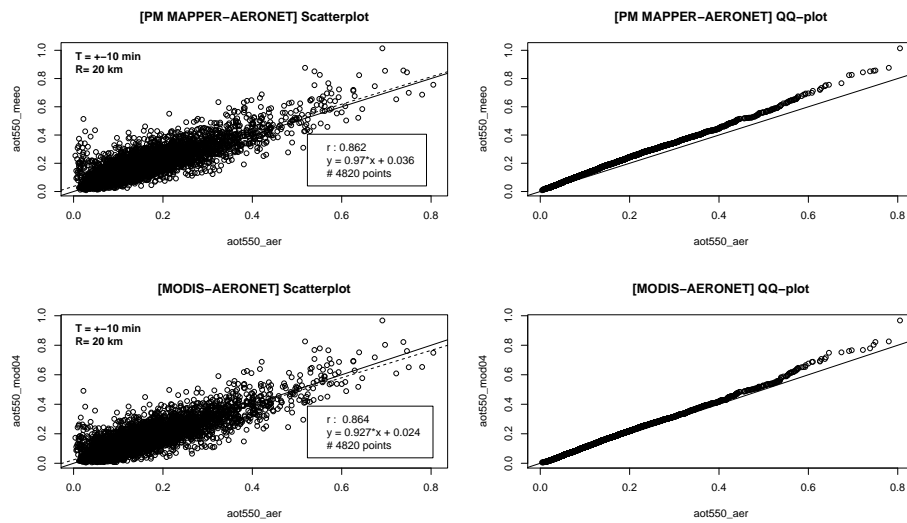
Fig. 4.8 – Scatterplot and Quantile-Quantile plot of AERONET AOT measurements against both PM MAPPER 1×1 km² (above) and MODIS (resampled) 10×10 km² AOT pixels (below) for a spatio-temporal window of ±10 min/20 km.

For further reading see Campalani et al. (2011a); for a technical report on the topic, refer to Campalani and Pasetti (2010a,b).

Table 4.1 – Best-case overall validation scores for both PM MAPPER 1×1 km² and MODIS 10×10 km² AOT, and for different filter options.

	PM MAP.	MODIS	
OVERALL # 4820	0.862 0.068 0.032	0.864 0.060 0.012	*r* **RMSE** **ME**
2007 # 1839	0.887 0.070 0.032	0.887 0.061 0.013	
2008 # 1637	0.833 0.074 0.037	0.837 0.063 0.017	
2009 # 1344	0.853 0.060 0.025	0.851 0.053 0.005	
Winter # 732	0.894 0.054 0.027	0.894 0.048 0.014	
Spring # 1444	0.855 0.075 0.037	0.858 0.064 0.014	
Summer # 1891	0.839 0.076 0.039	0.841 0.065 0.016	
Fall # 753	0.881 0.045 0.009	0.879 0.044 -0.001	
Vegetation # 3203	0.882 0.052 0.012	0.874 0.052 0.001	
Rangeland # 1110	0.868 0.076 0.032	0.875 0.066 0.012	
Dark Barren Land # 431	0.776 0.127 0.080	0.836 0.091 0.045	
Barren/ Built-Up # 384	0.681 0.097 0.018	0.759 0.079 0.003	

4.2 Study over Emilia Romagna

The validated spaceborne maps of AOT were firstly tested on a regional-scale model for air quality evaluation. The purpose of this study — funded by the SENSORER project (SENSORER Project, 2010) — was to evaluate a method for automatic prediction of PM_{10} concentrations by using previously validated PM MAPPER AOT maps as explanatory cross-correlated variable.

The analysis were performed with the data of 2007 over the Emilia Romagna region (Northern Italy) in the Po Valley, which is characterized by both a high level of anthropic pollution and stable air masses. The prediction methodology was then applied to yield daily continuous qualitative maps which were then published on-line on the Web platform Multi-sensor Evolution Analysis PM (MEA-PM) in an interactive GIS environment (Natali et al., 2011) where ground observation, satellite maps and gap-filled qualitative predictions could be analysed and overlaid, as shown in Fig. 4.9[3].

Specifically, the input datasets comprised PM_{10} daily averages of the ARPA-ER air quality network (Sec. 2.2.1), the available granules of AOT at 1 km² of resolution and two (static) auxiliary variables to account for the topography (via DEM) and the emissions (via spaceborne night lights observations). See Sec. 2.3 for details on these data.

As explained in Sec. 3.2.1, cokriging modelling offers the chance to include additional cross-correlated variables into the interpolation by structuring their spatial structure with both direct- and cross-variograms: for this reason cokriging was selected as stochastic model. The general workflow is depicted in Fig. 4.10.

Different variants on the cokriging assumptions were tested, namely:

---

[3]An updated version of MEA-PM is available at http://mea-pm.services.meeo.it/, but the kriged maps are not published yet.
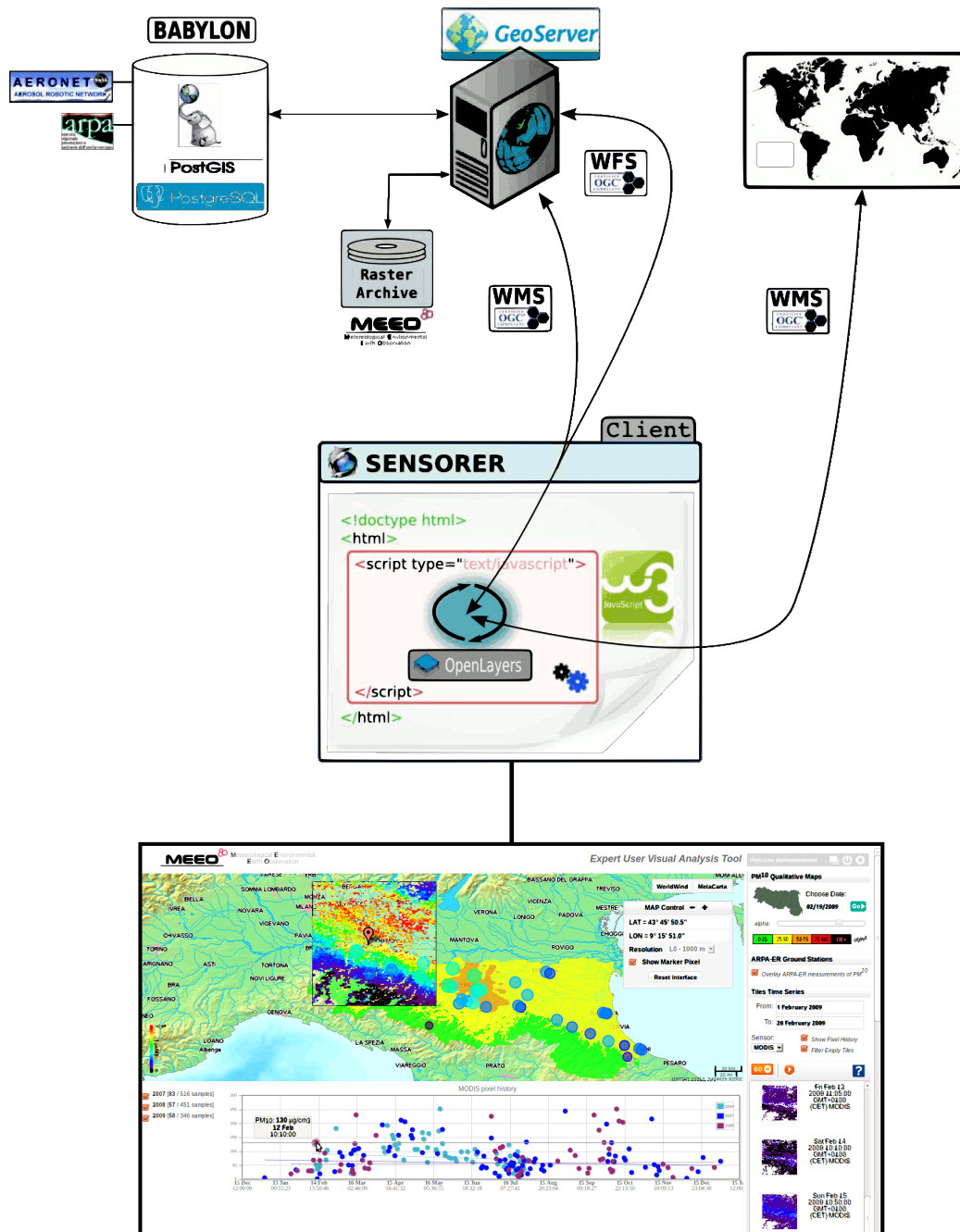
Fig. 4.9 – Internal workflow and Web interface of the MEA-PM platform: dynamic maps container is handled by OpenLayers javascript library, which fetches the raster and vector data requested by the end-user via OGC protocols (WMS and WFS) for visualization and basic analysis. On the server side, a GeoServer instance interfaces the data from filesystem storages and a PostGIS database.
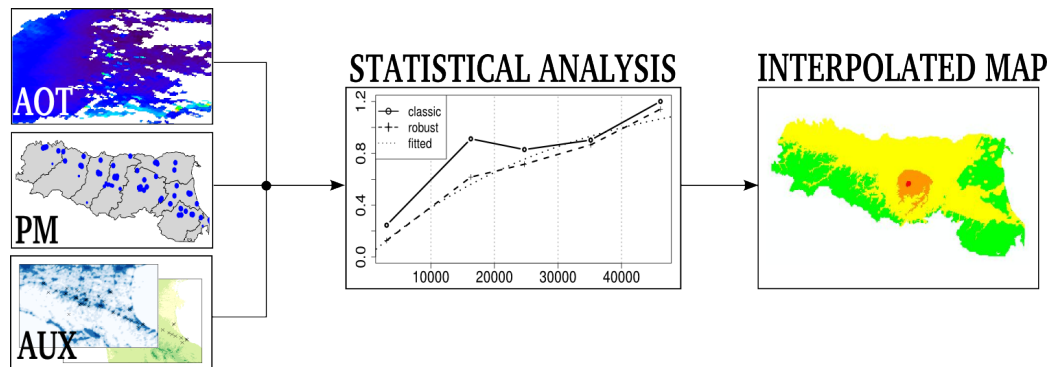
Fig. 4.10 – General workflow of the air quality models on Emilia Romagna: statistical analysis is carried out on the input data, namely ground measurements of PM_{10}, space-borne map(s) of AOT and auxiliary variables (a DEM and the yearly averages of night lights). Final predictions are published in the MEA-PM platform as qualitative air quality maps.

- 2-VARIATE ORDINARY COKRIGING (OCK).
  PM_{10} ground samples as primary target variable, and AOT satellite retrievals as unique covariate. Stationarity, i.e. constant mean, is assumed for both. Statistical model based on two direct- and one cross-variogram (Fig. 4.11a).

- 2-VARIATE UNIVERSAL COKRIGING (UCK).
  Constant mean assumed on PM_{10}, whereas a variable spatial trend is computed on AOT by regression with DEM and night lights as predictors. Statistical model based on two direct- and one cross-variogram, on the values of PM_{10} and the regression residuals of AOT linear model.

- 4-VARIATE ORDINARY COKRIGING.
  PM_{10}, AOT, DEM and night lights are treated as four independent stationary variables, each with a separate set of cokriging weights. Statistical model based on four direct- and six cross-variogram (Fig. 4.11b).

The selection of the neighbouring samples has been *localized* by constraining the search to 50 km around the unknown location, and anyway further limiting the search (logical OR) to the nearest 200 points. Further samples
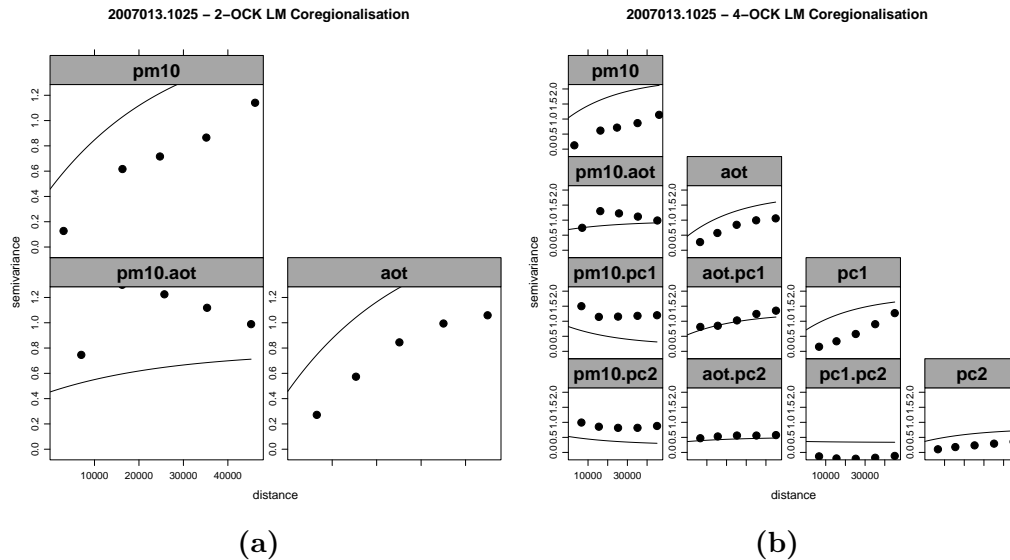
Fig. 4.11 – Different combination of direct- and cross-variograms that build the geostatistical model of ordinary cokriging, in case of two (a) and four (b) independent variables (PC1 and PC2 are the principal components extracted from DEM and night lights maps for orthogonalization).

were not taken into account and hence did not influence the prediction: this is commonly done by geostatisticians in order to reduce the computational efforts required. The stationarity assumptions were anyway more acceptable with localized kriging; moreover larger areas of neighbours search would introduce conceptual errors due to topographic or aerosol type heterogeneity (Ichoku et al., 2002).

The described variants were tested on the 365 days of available data by means of cross-validation scores on the ground measurements. Looking at the output statistics that were produced (Fig. 4.12), we could outline the following conclusions:

- firstly, the predictive precision of the different variants of cokriging did not show evident differences (see RMSE chart);

- despite the best performances were obtained with the 2-variate ordinary cokriging system (average RMSE of 10.511 $[\mu g/m^3]^2$) the prediction

gain was equivalent to that of a simple mechanic interpolator based on inverse distance weighting (average RMSE of 10.961 [µg/m^3]^2, see red line in the chart of RMSE);

- universal cokriging generated less biased estimations (-0.192 µg/m^3), whereas ordinary cokriging systems tended to underestimate the concentrations of PM$_{10}$ (see chart of Mean Error);

- performances were best during Summer (see chart of RMSE). This is related to the higher variance of the samples of PM$_{10}$ which is experienced during the colder months[4] because of higher pollutant emissions and lower boundary layer;

- relative performances were indeed independent of the season (see chart of R-squared).

If cokriging did not deteriorate the estimation with respect to an inverse distance interpolator, it did not generate a clear gain neither, which could justify such costly geostatistical analysis.

Trying to explain the unsuccessful results of cokriging, a first important remark is that the multiple mathematical constraints that ensure a positive-definite matrix system and the constraints of linear coregionalization generally shifted the fitted variograms models too far away from the experimental semi-variances, as can be clearly observed in Fig. 4.11. In addition, the spatial pattern of the ground PM$_{10}$ was not always clearly shaped by the variogram, sometimes because of the clustering in the stations' layout, or because of poor availability of samples.

For instance, Fig. 4.13 shows four different situations that were experienced

---

[4]Observed inter-quartile range of 30—40 µg/m^3 during Winter, and <10 µg/m^3 during Summer.
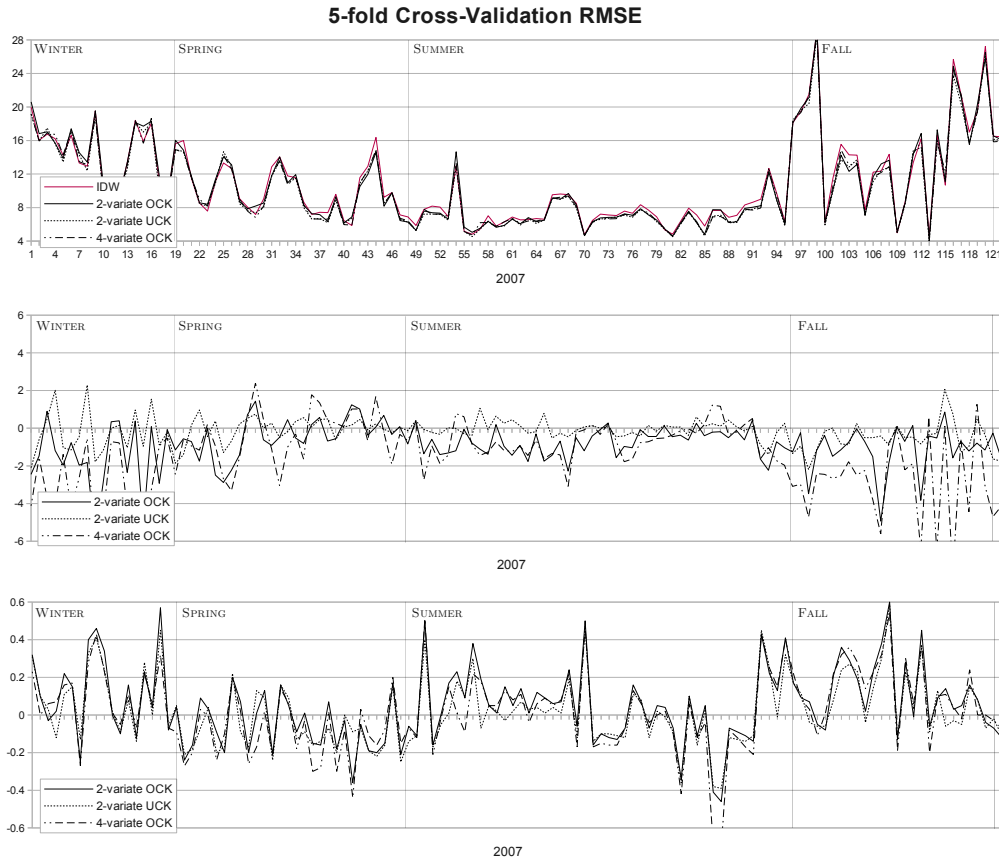
Fig. 4.12 – 5-fold averaged cross-validation statistics (RMSE, ME and R-squared, respectively) for each of the three tested cokriging solutions. RMSE for inverse distance weighting (IDW) interpolation is also highlighted in red. Vertical lines are plotted around equinoxes and solstices to identify the four seasons.

in the analysis. The high density of the pixels of AOT[5] could easily define the spatial autocorrelation and this is confirmed by the correspondent robust fitting which fairly follows the same line. This was not always true in the case of ground PM_{10} however. In case (a) we observe a good spatial structure in accordance with the sample variogram, while in case (b) the spatial structure is quite noisy and the fitted variogram does not reflect it faithfully; in case

---

[5]Only maps with a minimum of 20% of available pixels in at least 3 of the 4 quadrants were accepted.
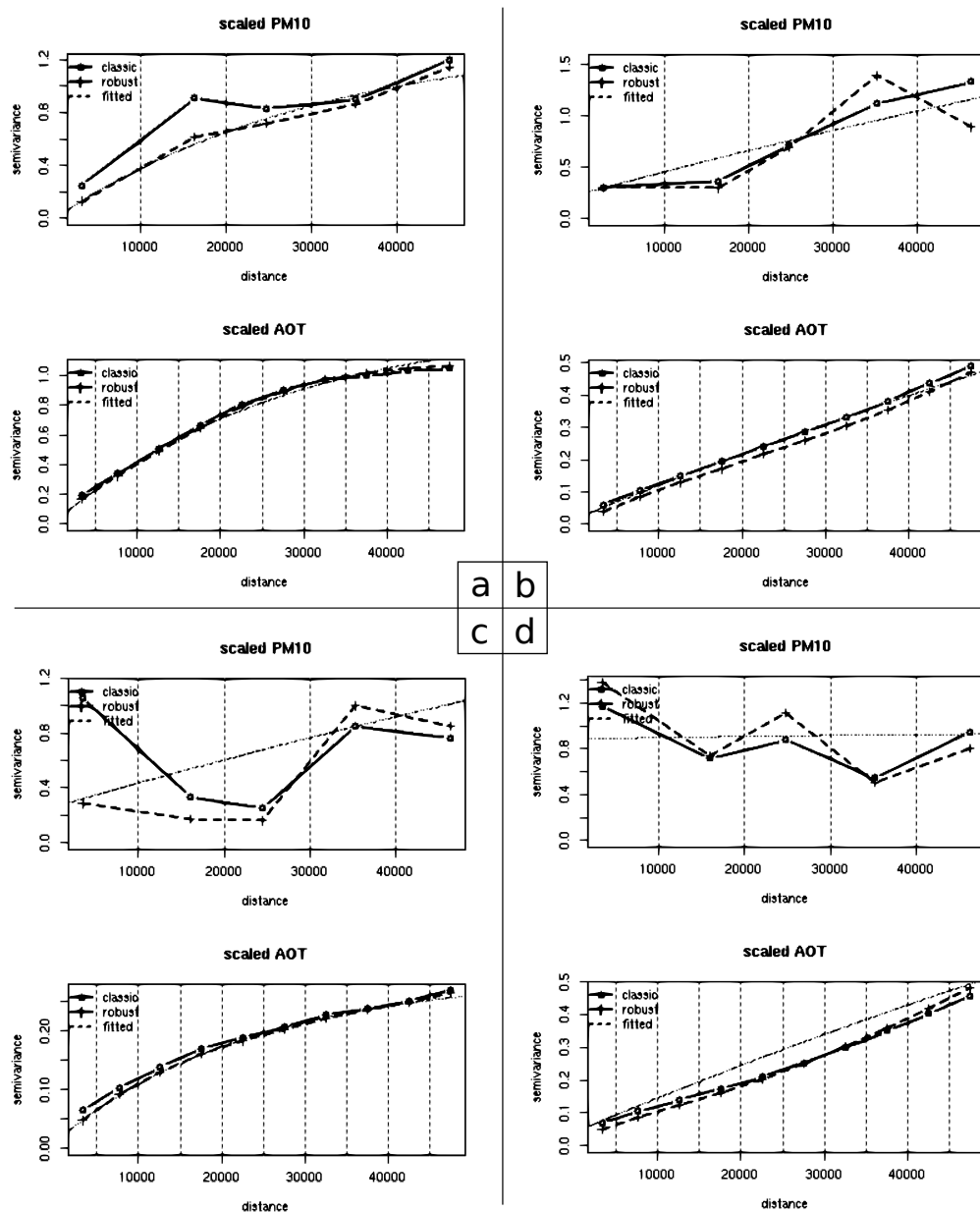
Fig. 4.13 – Examples of individual experimental and fitted variograms on four different days of the analysis (2007) for PM$_{10}$ gorund measurements and AOT pixels: (**-o-**) for the standard variogram estimation, (**-+-**) for robust estimation (Cressie and Hawkins, 1980), and fine-dashed line for model fitted on the robust sample variogram.

(c) there are probably several outliers due to high spots of pollution in the traffic stations which create a peak at short-distances: robust statistics can

actually handle this cases, as visible in the figure; finally in case (d) there is clearly no spatial autocorrelation in the measurements, which are then fitted as a pure nugget variogram.

Variogram modeling of the ground measurements is thus not always possible: there are days which are too noisy and would need either be replaced by some pooled model acting as default. The alternative is to extract some hints on the starting parameters from preceding variogram model(s) as historical base.

It is generally concluded that cokriging seems an improper method for an optimal application over the available datasets: the models are too far from what is expressed by experimental evidence, and much more care on the modelling phase should be taken by considering more complex non-linear coregionalization models or manual ad-hoc modelling, although they are not advantageous in the perspective of an automated system for near real-time air quality monitoring.

As a final remark, the lack of meteorological variables was probably critical in explaining the non-linear relationship between PM_{10} and AOT. Cross-variograms could hardly show a very sharp spatial structure and this implied that the information on the pixels of aerosols was not taken into account.

For further reading on the model, refer to Campalani et al. (2011b); for details on MEA-PM Web interface see Campalani and Pasetti (2010c).

4.3   Study over Austria

As underlined in the previous chapters (Sec. 1.3 and Sec. 3.1), the relationship between a spaceborne evaluation of the aerosols optical thickness and the dry-mass concentrations of particulate matter at the surface level is not defined by a simple linear scaling. There are several meteorological phenomena that
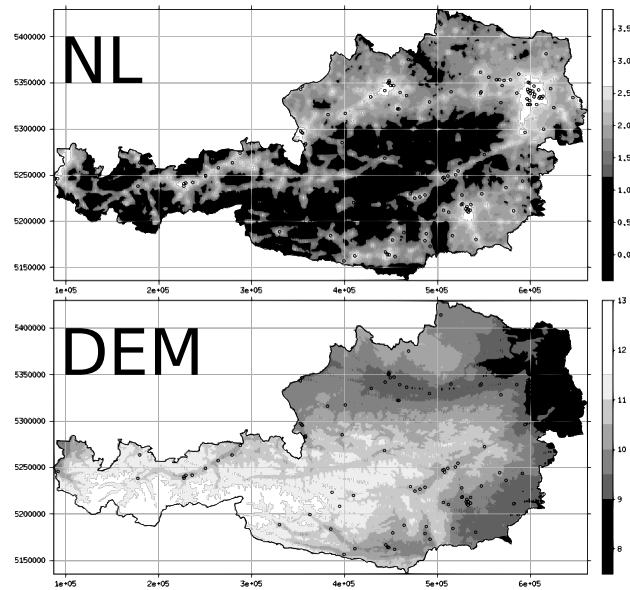
Fig. 4.14 – (Scaled) yearly average night lights and digital elevation model over Austria.

drive this relationship, above all the humidity, which increases the scattering ratio of the suspended aerosols, and the height of the boundary layer, which determines the volume of air where the particles are well mixed and confined.

Availability of three years of model-based forecasts of meteorological features over Europe (Sec. 2.3.1) and new PM_{10} assets from the Austrian air quality network (Sec. 2.2.2) gave unique chance for a new application of geostatistical interpolation for daily air quality predictions, this time with the help of the meteorological maps in explaining the PM_{10} and how AOT can be approximated to it.

Firstly, Fig. 4.14 depicts a spaceborne map of yearly averaged night lights (Sec. 2.3.3) and the DEM over Austria, to help figure out which areas have higher anthropic activity, and are the most populated.

Two different models were developed with these datasets: a first pure spatial one described in Sec. 4.3.1, then a spatio-temporal one described in Sec. 4.3.2.

4.3.1   Separate daily variograms

Cokriging showed several limitations in trying to proxy AOT and PM_{10} as demonstrated in the previous section, mainly because of important shifts in the fitted variogram model after coregionalization. The explanatory information of AOT could also not emerge clearly with cross-variograms.

A different approach was chosen for this new application: instead of modelling the spatial cross-correlation among the explanatory variables and PM_{10} in the variograms, we decided to use the independent variables to define the global *trend* of the PM_{10} by means of multivariable linear regression; in this case kriging was used to model the spatial structure of the residuals (which still would be usually present in case the linear model cannot explain the whole variability of PM_{10}). This estimation method, described in Sec. 3.2.2, is called kriging with external drift: the *drift*, i.e. the global trend, is driven by *external* variables.

Fig. 4.15 depicts the workflow of the developed method in more detail: the input of the model consists of the ground measurements of PM_{10}; the maps of meteorological features – namely pressure, wind 3D components, relative humidity and height of the mixing layer — and, in case there are enough available pixels, the interpolated composite of AOT information. All the meteorological maps were interpolated to 1 km^2, to meet the spatial resolution of the AOT granules from PM MAPPER. A preliminary study showed how the correlation between AOT and PM was best at this resolution.

In the first instance, the input data was included along with temperature forecasts, geographical coordinates, and the fixed covariates of elevation and night lights (Fig. 4.14). A preliminary analysis of multicollinearity among the input predictors was carried out, revealing how those were better left out to avoid redundancy in the data that would compromise the evaluation of the regression results, as well to reduce the degrees of freedom in the regression

as much as possible to remove the noise of unnecessary predictors (Faraway, 2002).

Regarding the selection of AOT, an empirical criteria was used to decide whether to keep or not a map of AOT, facing a trade-off between daily availability of AOT in the prediction system, and square kilometers of more uncertain interpolated pixels.

Table 4.2 shows the percentage of days where AOT could be accepted in the model, with different thresholds of AOT pixels availability, for the three years of analysis: because of the very high cloud and snow presence over Austria in the cold season, only ca. one third of the maps of AOT could pass even the threshold of 5%. This can be appreciated as well in Fig. 4.16. In order to accumulate a critical mass of AOT data, a threshold of 30% was chosen, this way collecting ∼100 days of PM_{10} modelling *with* the AOT in the prediction.
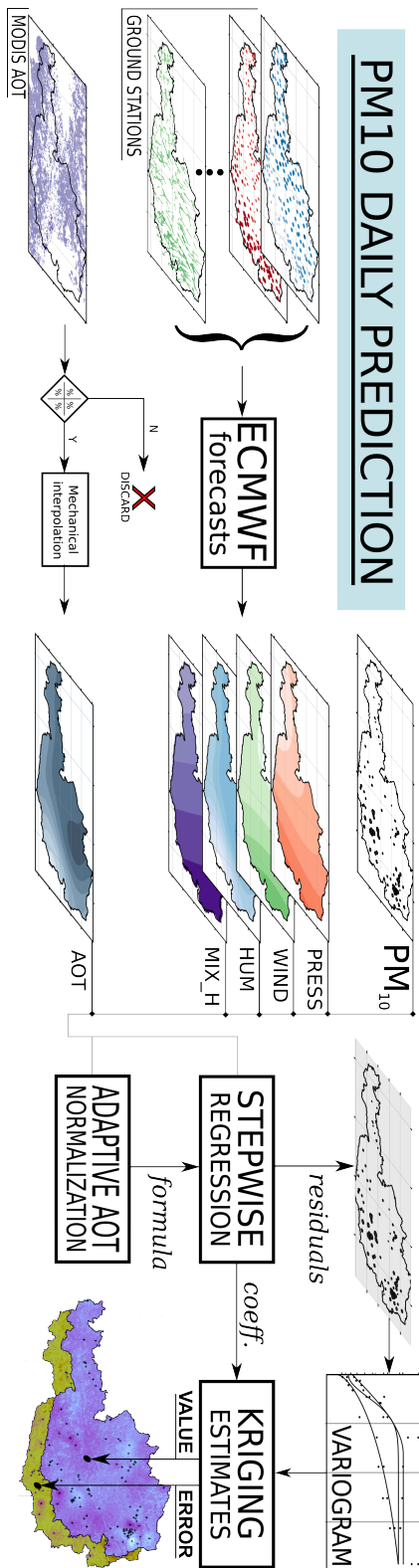
Fig. 4.15 – Workflow of the prediction of PM_{10} in Austria with regression-kriging: when a sufficient percentage of available pixels of aerosols are available, AOT is added to the covariates which define the regression, with ad-hoc normalization against the meteorological variables. Kriging adjusts the regression by modelling the spatial pattern of the residuals.

Table 4.2 – Percentage of AOT granules satisfying a minimum % of pixel availability over Austria for the three years of analysis and for different thresholds of percentage.

Threshold	2008	2009	2010
5%	33.4	37.8	20.4
10%	24.1	29.4	14.5
20%	16.5	19.0	9.4
30%	11.1	12.9	6.8
40%	6.9	10.1	4.2
50%	3.2	6.9	3.0
60%	1.4	3.0	2.0
70%	0.2	1.7	1.1
80%	0	0.5	0.4
90%	0	0	0

Looking back again at Fig. 4.15, after the input data are overlaid, an ad-hoc formula would feed the regression trend: this was done to choose the daily best option that would convert the AOT columnar averages to ground particulate matter. Indeed, in some preliminary analysis it was observed how there was no clear trend in which meteorological variables were helping define the AOT-PM_{10} relationship (RH and PBLH were the best case respectively in the 28% and 23% of the days).

All the available meteorological variables were involved in this analysis. Not only the height of the boundary layer and humidity can be a candidate for AOT normalization: at lower pressure levels (higher altitudes) the atmospheric mixing volume is more compressed and hence there is probably a higher agreement between columnar and surface-level aerosols; low wind in-
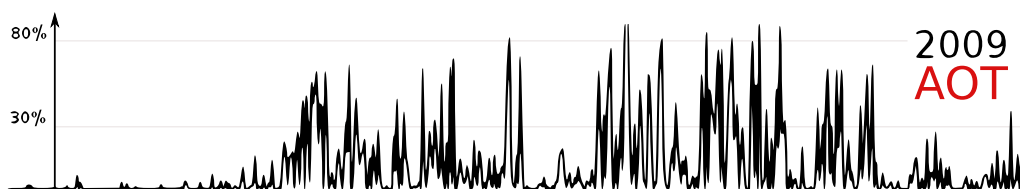
Fig. 4.16 – Percentage of available AOT pixels at 1×1 km^2 from PM MAPPER within Austrian borders in 2009.
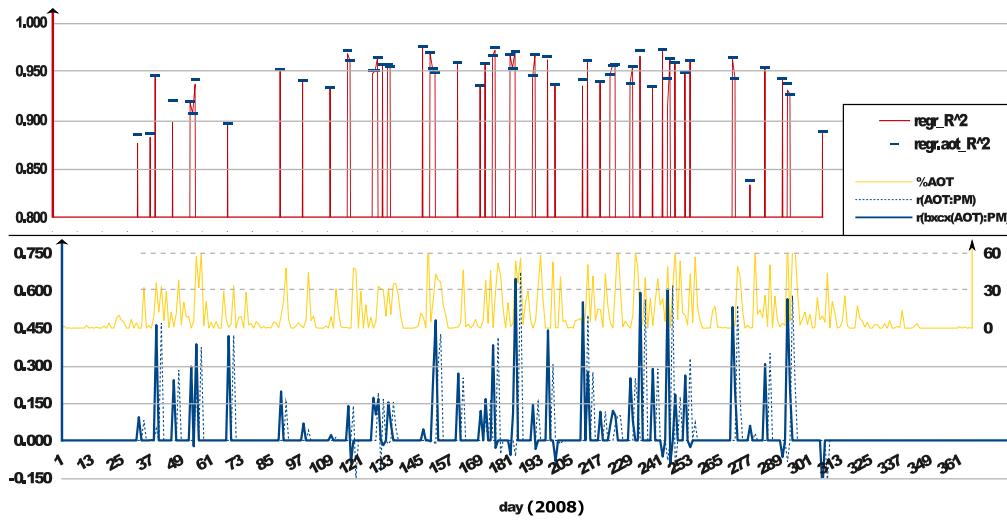
Fig. 4.17 – Charts of AOT-PM$_{10}$ relationship for the year 2008: above, the regression goodness-of-fit with (blue segments) and without (red lines) the contribute of AOT; below, the correspondent AOT-PM$_{10}$ linear correlation with both raw (blue line) and Box-Cox transformed (dashed blue line) AOT, along with the availability of non-interpolated AOT pixels (yellow line).

tensities imply instead a closer relationship between an instantaneous observation and the daily-averaged measurements done by the ground sites.

The adaptive regression formula was then used as input for the stepwise linear regression, to keep only the significant predictors. The final regression residuals were then modeled by a variogram through automatic selection over a finite set of functions, and then added back to the regression surface, so as to fix misspecifications in the linear model and to be aware of the relative geographic position of the inputs.

A key analysis was carried out on the regression results, with the aim of understanding the role of AOT. Looking at Fig. 4.17, it became clear how the fit of the regression was almost completely independent of the presence of aerosol information (see red chart), probably due to:

- the high predictive power of the meteorological variables alone (pressure above all), which could explain a very high percentage of variability of

the ground concentrations of PM_{10} (a median adjusted R^2 of 0.93 was observed in the three years), keeping out the AOT from having a leading role in the regression;

- the unstable correlation of the pixels of AOT with PM_{10} (see blue chart), which varied from totally uncorrelated values ($r \sim 0$) to moderately high association ($r \sim 0.6$), with no visible dependency on the original percentage of data pixels (yellow chart);

- the increased error introduced by the intermediary interpolation of AOT, which was needed to fill the output grid of prediction with required AOT information.

Analysis of the residual variograms showed a clear prevalence of the Matern model (M. Stein's parametrization, Stein 1999), chosen in the 70% of the days in the three years. This has a moderately high slope at the origin, hinting some spatial variability at proximate locations of the regression residuals, and so some misspecification to be balanced by kriging. The sample variograms of the remaining days were fitted with Gaussian and spherical models (15% each) instead. The range was of 40 km on average, though with a high variability on the different days.

This was also confirmed by the relevant nugget component in the models, 0.4 on average (over scaled residuals), with a higher trend in the warm months (0.55). In the warm season the higher nugget effect was associated with lower values of the partial sill, hence resulting in close-to pure nugget variogram models: in these cases the kriging adjustments on the regression would not be relevant. A stronger spatial pattern was shown during the cold season instead, may be caused by the lack of AOT information as a stronger predictor.

A posteriori analysis of the cross-validation results (Tab. 4.3) showed that, independently of the actual role of AOT, the kriging model could minimize

Table 4.3 – Leave-One-Out (LOO) cross-validation median statistics for daily PM_{10} predictions using Inverse Distance Weighting (IDW), Linear Model (LM) and External-Drift Kriging (KED), for the three years of analysis.

	RMSE $[(\mu g/m^3)^2]$			**ME** $[(\mu g/m^3)]$			**Pearson's** r		
	IDW	LM	KED	IDW	LM	KED	IDW	LM	KED
2008	6.076	5.620	5.498	-0.7	-2e-3	-0.06	0.611	0.878	0.796
2009	5.988	5.268	5.210	-0.7	-2e-3	-0.05	0.630	0.884	0.821
2010	6.653	6.276	6.008	-0.5	-1e-3	-0.05	0.614	0.873	0.798

Table 4.4 – Leave-One-Out (LOO) cross-validation median RMSE errors for daily PM_{10} predictions using with External-Drift Kriging (KED) estimator for different periods of the year.

	Jan-Apr	**May-Aug**	**Sep-Dec**
2008	7.588	3.926	6.375
2009	6.624	4.019	5.531
2010	7.496	4.398	6.631

the square error (5.57 [µg/m³]²) with respect to an inverse distance interpolator, with an increased prediction power of 11%. Although the linear regression alone maximized the linear correlation and could yield less biased predictions, the kriging corrections were necessary to account for the relative distances of the observations and thus to have a real *geo*-statistical model.

Tab. 4.4 shows the variations in the cross-validation statistics for different periods of the year: similarly to the performances of the regression drift, the kriging predictions were closer to the actual PM_{10} measurements during Summer, as it was observed in the previous model over Emilia Romagna. Although the mixed layer is usually higher during the warm season for solar heating, this could be explained by the higher variances in the PM_{10} concentrations during these months, which gives way to more hardly predictable outliers.

Fig. 4.18 shows an example of daily output predictions for the three tested approaches. The kriging effect can be appreciated when comparing the linear model to the KED prediction, especially in the areas with high concentra-

tion of ground stations (note the agglomerate in the area of Vienna): the linear regression is completely unaware of the relative positions of the data, whereas the variogram model can correct this behaviour and thus produce more realistic estimations. Gaussian simulations are anyway suggested at the operational stage of a model for more realistic predictions.

Detailed results on this case study are presented in Campalani et al. (2012).
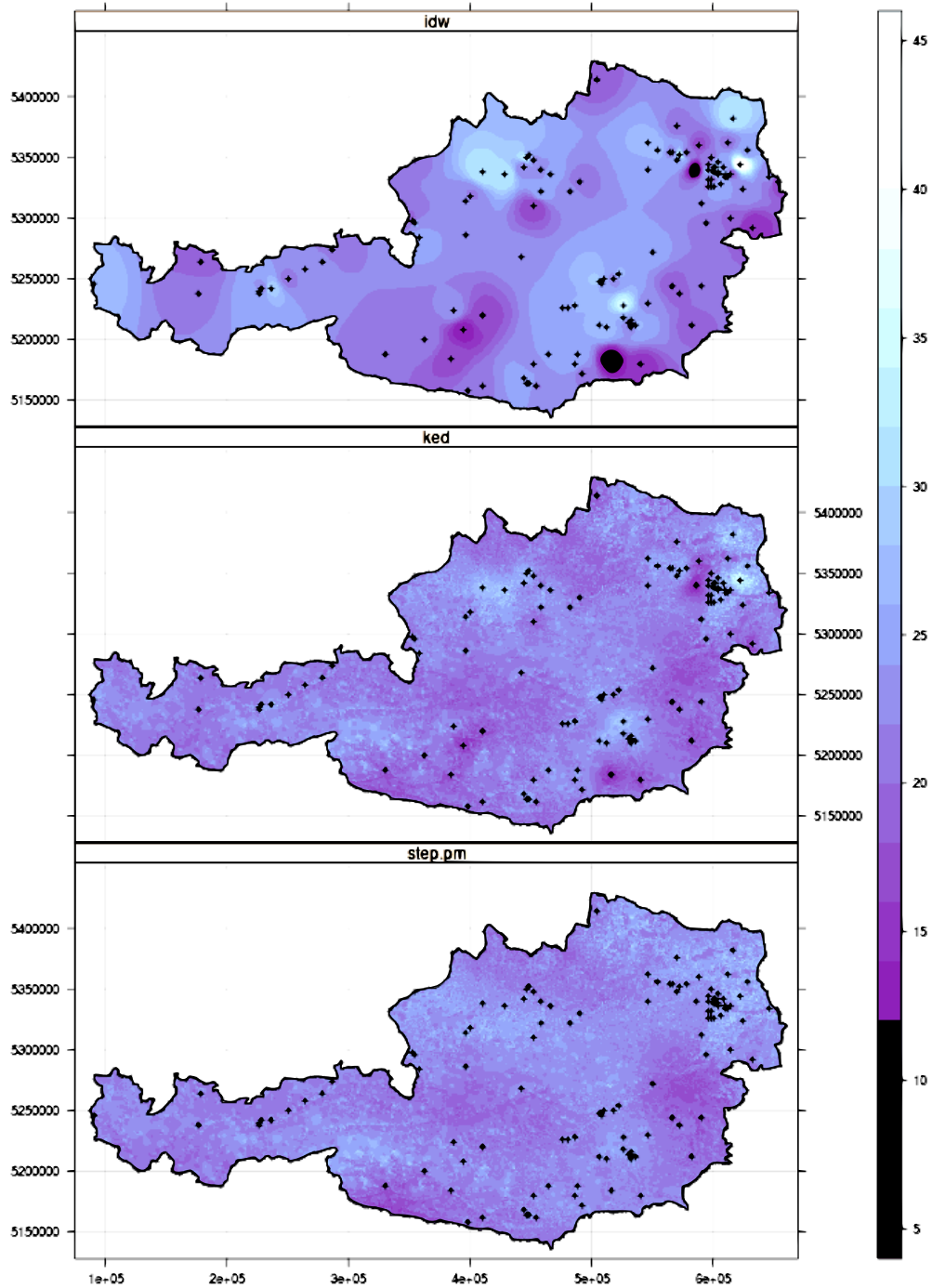
Fig. 4.18 – Example of daily gap-filling of PM_{10} over Austria for the three tested interpolation methods: mechanical inverse distance weighting above; kriging with external drift in the middle; drift (linear regression model) without kriging below.

4.3.2   Spatio-temporal interactions

After evaluating the predictive power of kriging with regression, the question was whether the additional temporal autocorrelation of the input data could further help deducing the values of PM_{10}.

In the previous analysis, an estimation of PM could was not constrained by the availability of AOT amongst the predictors (see again Fig.4.15). Now the prediction of PM_{10} over an unknown location selects measurements and covariates in the close distances but across several days of aggregated dataset. Aggregating the data in time to partially fill the holes of AOT was also not considered since, as will be shown in this section, the memory of PM in time usually does not go beyond the single preceding day.

A regression analysis was carried out on both AOT and PM_{10} with a selection of meteorological features. The former could be predicted with appreciable accuracy by means of the three wind components (U,V,W) and pressure (PRESS), yielding an average adjusted goodness-of-fit of ~ 0.779 over the three years: the same performance was obtained when involving the whole set of meteorological variables in the regression. The remaining ones, i.e. the height of the planetary boundary layer (PBLH) and the relative humidity (RH), were then used together with the AOT to predict the surface particulate matter.

The average results, divided into three trimester per year to account for seasonality, were then hard-wired in the model to help filling the missing values of AOT in days of almost total absence of aerosol information.

Pressure had a main role in the prediction of AOT over Austria, due to the relevant inverse proportionality between emissions and elevation. A bivariate analysis between AOT and the meteorological fields confirmed this. Moreover no significant differences were found between the linear Pearson's

correlation and the correspondent Spearman rank one correlation for all the covariates: no further transforms on the data seemed then necessary.

A second preliminary analysis focuses on which formula to use in the regression of PM_{10}. As turned out in the previous section (Sec. 4.3.1), PBLH and RH were the best explaining the association of AOT to PM. Different models of regression were thus possible and tested, respectively:

(a) $PM_{10} \sim AOT^* + PBLH + RH$

(b) $PM_{10} \sim \frac{AOT^*}{PBLH} + RH$

(c) $PM_{10} \sim \frac{AOT^*}{RH} + PBLH$

(d) $PM_{10} \sim \frac{AOT^*}{PBLH \cdot RH}$

where AOT^* is starred because it is spatialised via regression with pressure and wind where missing. An ANOVA analysis revealed that the first model was often the most explanatory, although 0.05 significance was not always ensured ($\sim 70\%$ of the days). Normalization by PBLH or RH could never help to better match with PM_{10}, whereas normalization by both did not help resolving the surface particulate. This is also explained by the intermediate interpolation of AOT and the absence of RH modulation.

As done in several other studies on the topic (Randriamiarisoa et al. 2006, Koelemeijer et al. 2006, Wang et al. 2010), humidity fields could be pre-processed by means of a so-called aerosol scattering growth factor $f(RH)$, which is the ratio between wet and dry scattering cross-sections of atmospheric aerosols. Different approximations are possible to account for increased scattering under wet conditions (e.g. Hanel parametrization, Hänel 1976), however each model is only suitable for certain chemical compositions of the aerosols, hence specific experiments in the region of interest are preferred. Otherwise using the wrong growth factors might add uncertainty to the model. Having no experimental values of $f(RH)$ over Austria, it was decided to keep the raw (scaled) humidity pixels.
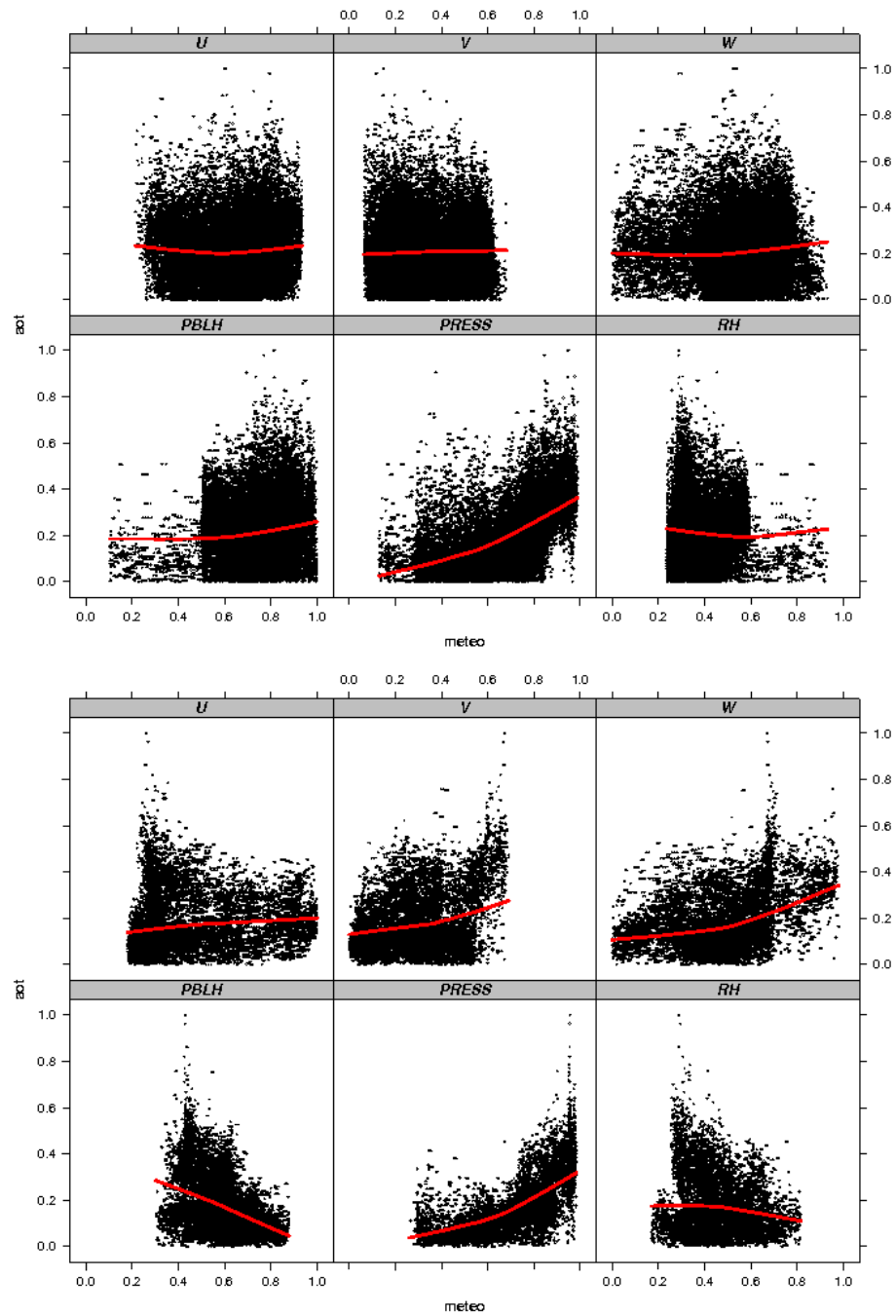
Fig. 4.19 – Examples of bivariate analysis scatterplots between satellite AOT and meteorological features for two different days (14 June in the plots above and 26 August below, 2009): pressure (PRESS) revealed to be in stable accordance with the levels of atmospheric aerosols over Austria.

Preprocessing steps that were used in the purely spatial model of KED, were kept in this analysis as well: i) declustering of the ground stations, ii) union of consecutive MODIS granules, iii) power transform of AOT for normalization of its distribution, iv) $[0, 1]$ scaling of all dependent and independent variables, and v) geographic warping to a common UTM projection.

In Sec. 3.2.3 a list of possible uses of time series of spatial data were listed. Here the model tried to shape the spatio-temporal PM process by means of a *separable* model of covariance. This way the estimator needs one 2D variogram for the spatial autocorrelation of the residuals of the PM regression, and a second 2D variogram to model the temporal autocorrelations.

Beforehand, a variogram analysis on the three years of data was carried out to understand the sensibility of the variogram fit and stability for different scales in both time and space. Analysing the results — one example is proposed in Fig. 4.20 — it could be observed how *spatial* pooling was bringing in too much noise into the variogram cloud, which very often resulted in plain models, even just for one week of measurements. PM_{10} revealed instead a slower variability in *time*, and temporal pooling was usually possible although often with a range of 2 days only, so that only the information of the previous day could be exploited to correct the kriging estimations. In order to have stable temporal variograms, a windows of 1 month was chosen for pooling, whereas single-day spatial variograms were selected for each day.

Fig. 4.21 shows the experimental data from which variograms could be pooled in time for the same month: it can be observed how cross-sections at certain spatial lags are showing a temporal pure-nugget shape, hence no statistically relevant memory in time was registered.

Cross-validation statistics are listed in Tab. 4.5. A direct comparison between a regression-kriging model with (ST-KED) and without (KED) temporal modelling of the semi-variances is highlighted, and it is clear how temporal autocorrelation of the drift residuals could not bring the expected gain, as
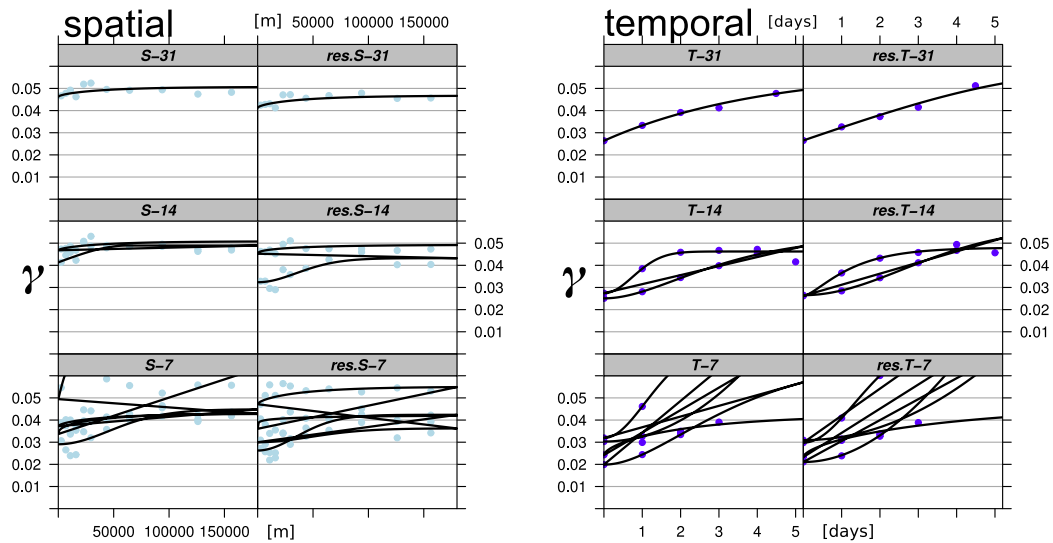
Fig. 4.20 – Examples of variograms for both spatial and temporal pooling of scaled PM_{10} (December 2010). For each table: the first column is for the direct variogram of PM_{10} and right column is for the residual variograms; rows are respectively for 1-month, 2-weeks and 1-week pooling intervals.

far as the cross-validation can tell.

In addition to a more pronounced (negative) bias — ~ 0.01 against ~ 0.001 —, the precision of the estimator seemed to degrade systematically of $\sim 5\%$ when additional measurements from previous days were taken into account.

Despite the performances seemed better then the previously described KED model (see again Tab. 4.3 in Sec. 4.3.1), this was due to the different PM_{10} input data, which were taken from the hourly (and not daily) averages including the MODIS overpass time: as a confirmation, the IDW performances were also computed and confirmed worse, but proportional, statistics.

The results obtained are not extremely surprising. The large amount of data feeding the predictor were probably pushing the model far away from real world interactions. In this case the additional data was also carrying an excessive amount of uncertainty, concentrated in a) the gap-filling of AOT data through multiple regression models, b) the separable-covariance model
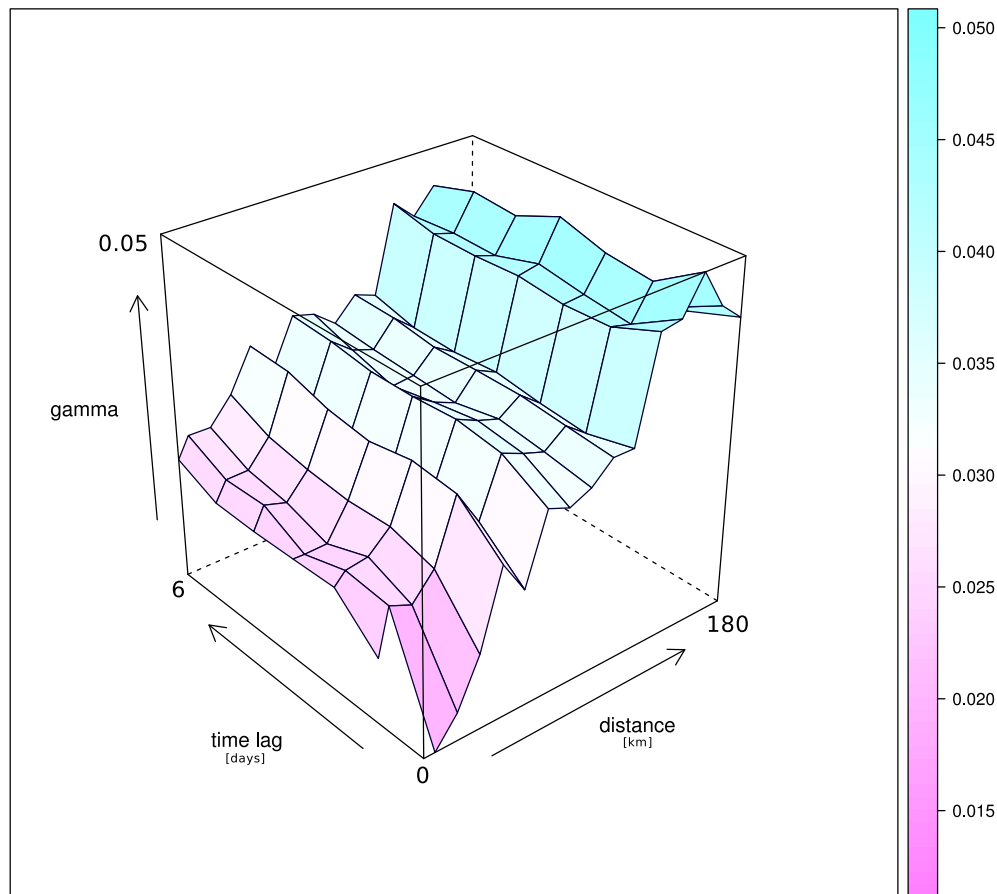
Fig. 4.21 – Example of experimental direct variogram for January 2008 of scaled PM_{10}: lags couple days in between observations and spatial distance for a whole month of measurements from ground stations.

requiring pooled temporal variograms which might not be representative of the whole month, c) the model-based interpolated maps of meteorological covariates themselves. This is in addition to inherent uncertainties in the ground monitoring assessment and of course that inherent important uncertainty that can lie in the AOT pixels, especially over Austria where many border-pixels (cloud and snow masks) are present.

Fig. 4.22 shows the values of RMSE scores for the year 2010: it is fairly clear how the magnitude of the errors is proportional to the range of the feature space of the PM measurements. On one side the plot shows that no seasonal

Table 4.5 – Leave-One-Out (LOO) cross-validation median statistics for daily PM$_{10}$ predictions using pure spatial External-Drift Kriging (KED), and spatio-temporal modelling with separable covariance and monthly pooling of variograms (ST-KED), for the three years of analysis. A loss of predictive power (%) is also reported (considering absolute values for the mean errors).

	RMSE $[(\mu g/m^3)^2]$			**ME** $[(\mu g/m^3)]$		
	KED	ST-KED	%	KED	ST-KED	%
2008	1.965	2.041	3.9	0.009	-0.059	556
2009	1.864	1.954	4.8	-0.013	-0.048	269
2010	1.835	1.927	5.0	0.002	-0.053	2550

trend exists in the load of particles on average over Austria; secondly it shows a clear proportionality of the predictors' performances with the daily standard deviation of PM$_{10}$, as supposed in the previous analysis over Emilia Romagna.

Analysing the pooled temporal variograms that were fitted on the monthly segments of inputs (Fig. 4.23), we can observe how generally it was pretty rare to have a valuable inter-correlation in time of the PM$_{10}$ residuals: often the sill was reached already in the first temporal lag, and having a daily resolution in the input, no inherent correlations of data at fractional temporal intervals could be exploited.
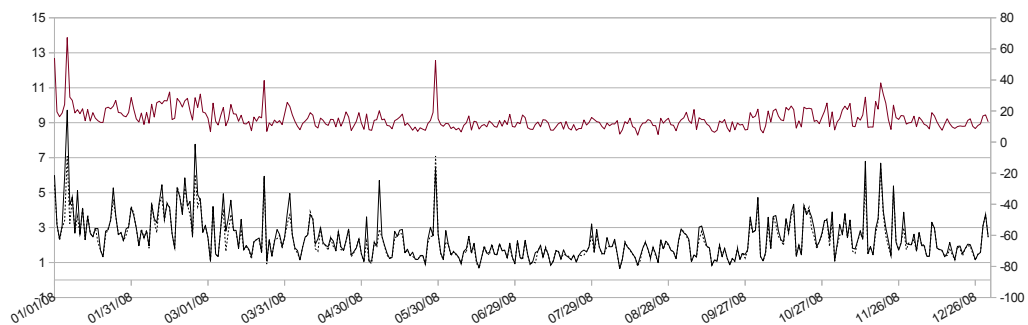
Fig. 4.22 – Leave-One-Out (LOO) cross-validation chart of RMSE for the year 2008: black line and dashed black line are for ST-KED and KED estimators, and refer to the left-side Y axis $([(\mu g/m^3)^2])$; the red line represent the standard deviation of the hourly means of ground PM$_{10}$.
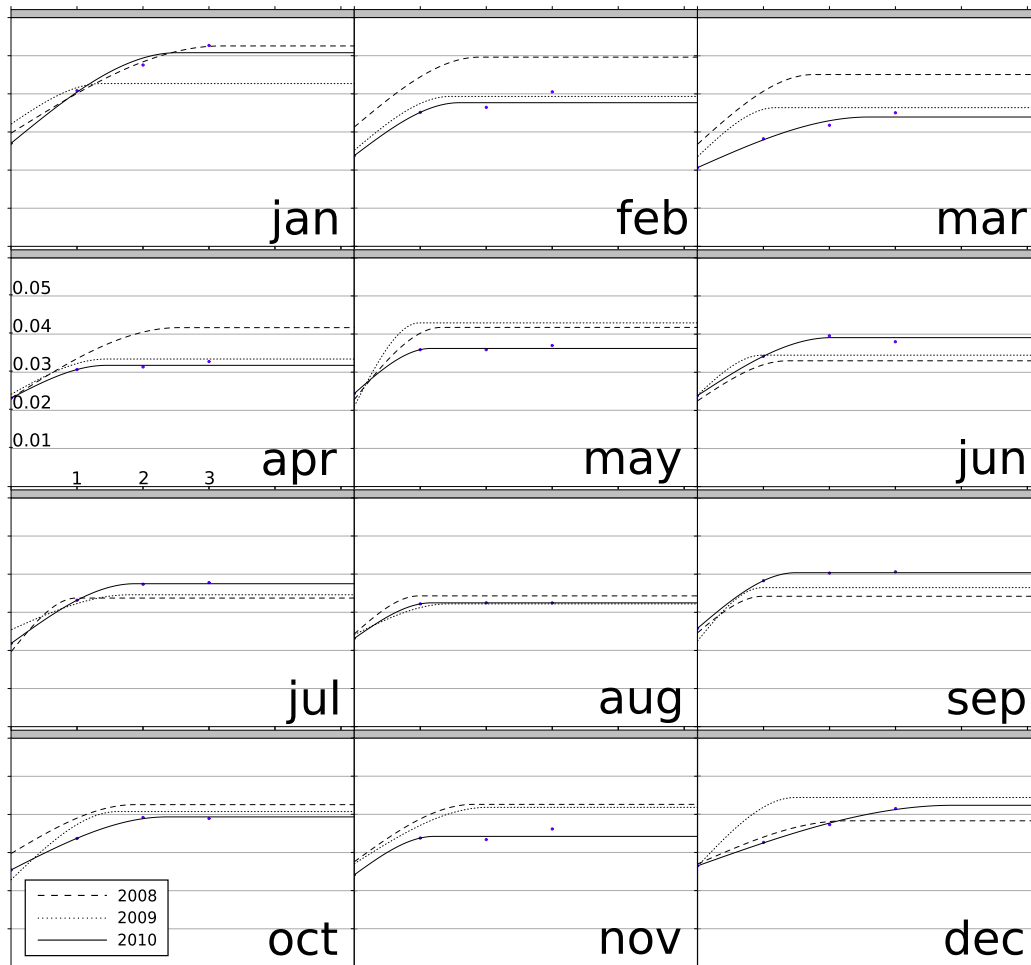
Fig. 4.23 – Residual variogram models for each month of the three years of analysis that were used in the separable-covariance predictor.

Even in cases where the data of the previous day seemed to show covariance over a certain month (see for instance the model for January 2008 or June 2010 in Fig. 4.23), this did not translate into better cross-validation scores.

Considering all these results, time was included in the geostatistical prediction with no predicting gain; the requirements that came along a spatiotemporal kriging with external covariates forced the inclusion of a critical amount of noise (interpolated data) in the inputs, which inevitably compromised the performance.

Additionally, specifically for the Austrian region, particularly strong memory of exposures was not observed: the high variability in the values of PM_{10} (and as well on the regression residuals) is probably due to complex wind profiles, although the rugged alpine topography could let foresee some sort of stability in time.

Pooling in time for each month was applied in order to have a sufficiently wide temporal interval where to compute semi-variances. This, however, forced the use of the same pooled temporal variogram for each day of the month. A moving window with daily re-computation of variogram models, preferably with inseparable covariance model, might have better represented the spatiotemporal interactions actually taking place. Regardless, there were no visible indicators of a real valuable usability of the MODIS data for this task.

Finally, predicted maps of PM_{10} were loaded into the `rasdaman` Array DBMS for analysis and Web-based processing of the resulting maps, as discussed in detail in Sec. 3.3. Tab. 4.6 presents a list of examples of functionalities that could be exploited by geostatisticians for a posteriori visualization of the interpolated maps via OGC WCPS protocol. Fig. 4.24 shows instead the monthly pollution means for the year 2008 that were retrieved via WCPS, showing how emissions were higher on average in the cold months probably due to more intense traffic and home heating.

Table 4.6 – Examples of WCPS responses for analysis of time-series of kriged maps. The images were loaded in `rasdaman` as a 3D regular temporal series of daily 2-bands 63×36 Float32 GTiff images, named `STKrigingAustria`. One band (*prediction*) hosting the estimations of PM_{10} mass concentrations; the other band (*variance*), representing the pixels of associated kriging error. Austria borders were manually overlaid.
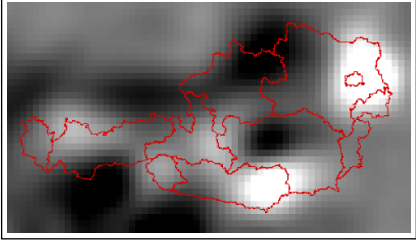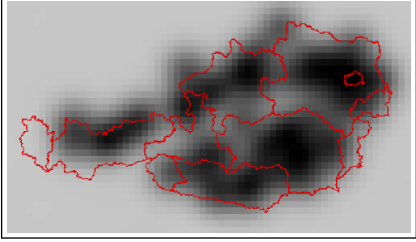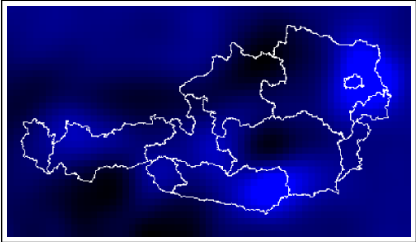
Daily estimates (greyscale):
 	
``for map in (STKrigingAustria) return
  encode(255 *
        (map[t("2008-01-02")]).prediction /
    max((map[t("2008-01-02")]).prediction),
  "png")```	

Daily estimates uncertainty (greyscale):
 	
``for map in (STKrigingAustria) return
  encode(255 *
        (map[t("2008-01-02")]).variance /
    max((map[t("2008-01-02")]).variance),
  "png")```	

Daily estimates (shades of blue):
 	
``for map in (STKrigingAustria) return
  encode({
    red: (char)(0);
    green: (char)(0);
    blue: (char)(255 *
        (map[t("2008-01-02")]).prediction /
     max((map[t("2008-01-02")]).prediction))},
  "png")```	

	Continued on next page

Table 4.6 – continued from previous page
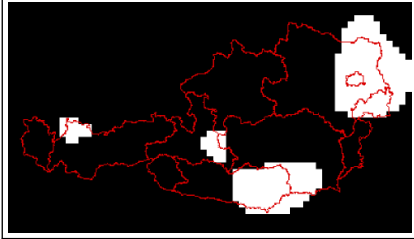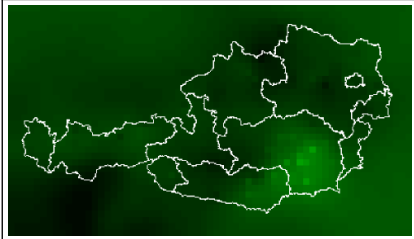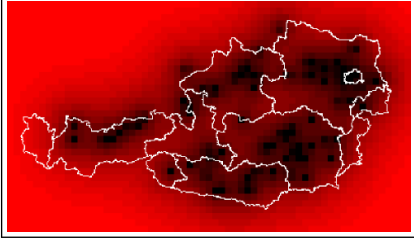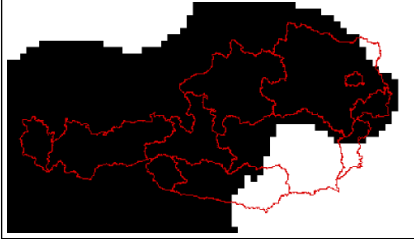
10μg/m³ 95%-confidence exceedance map of single day: ```for map in (STKrigingAustria) return` ` encode(` ` ((map[t("2008-01-02")]).prediction +` ` (map[t("2008-01-02")]).variance *` ` 1.644854) > 10 ,` ` "png")```	
Monthly average of estimated concentrations: ```for map in (STKrigingAustria) return` ` encode(` ` coverage monthly_average` ` over $Lon x (0:62),` ` $Lat y (0:35)` ` values {` ` red: (char)(0);` ` green: (char)((float)255 *` ` (float)avg((map[` ` x($Lon), y($Lat),` ` t("2008-01-01":"2008-01-31")]` `).prediction) /` ` (float)max((map[` ` t("2008-01-01":"2008-01-31")]` `).prediction));` ` blue: (char)(0)},` ` "png")```	
	Continued on next page

Table 4.6 – continued from previous page

Monthly average of estimates uncertainty:
 	
``
for map in (STKrigingAustria) return
  encode(
    coverage monthly_average
    over $Lon x (0:62),
        $Lat y (0:35)
    values {
      red: (char)((float)255 *
        (float)avg((map[
          x($Lon), y($Lat),
          t("2008-01-01":"2008-01-31")]
).prediction) /
        (float)max((map[
          t("2008-01-01":"2008-01-31")]
).prediction));
      green: (char)(0);
      blue: (char)(0)},
  "png")
``	

$20\mu g/m^3$ 99%-confidence exceedance map of a month:
 	
``
for map in (STKrigingAustria) return
  encode(
    coverage monthly_average
    over $Lon x (0:62),
        $Lat y (0:35)
    values (avg((map[
        x($Lon),y($Lat),
        t("2008-01-01":"2008-01-31")]
).prediction) +
      avg((map[
        x($Lon),y($Lat),
        t("2008-01-01":"2008-01-31")]
).variance) * 2.326348) > 20,
  "png")
``	

(a) January **(b)** February **(c)** March

(d) April **(e)** May **(f)** June

(g) July **(h)** August **(i)** September

(j) October **(k)** November **(l)** December

0 µg/m³   19 µg/m³   38 µg/m³   57 µg/m³
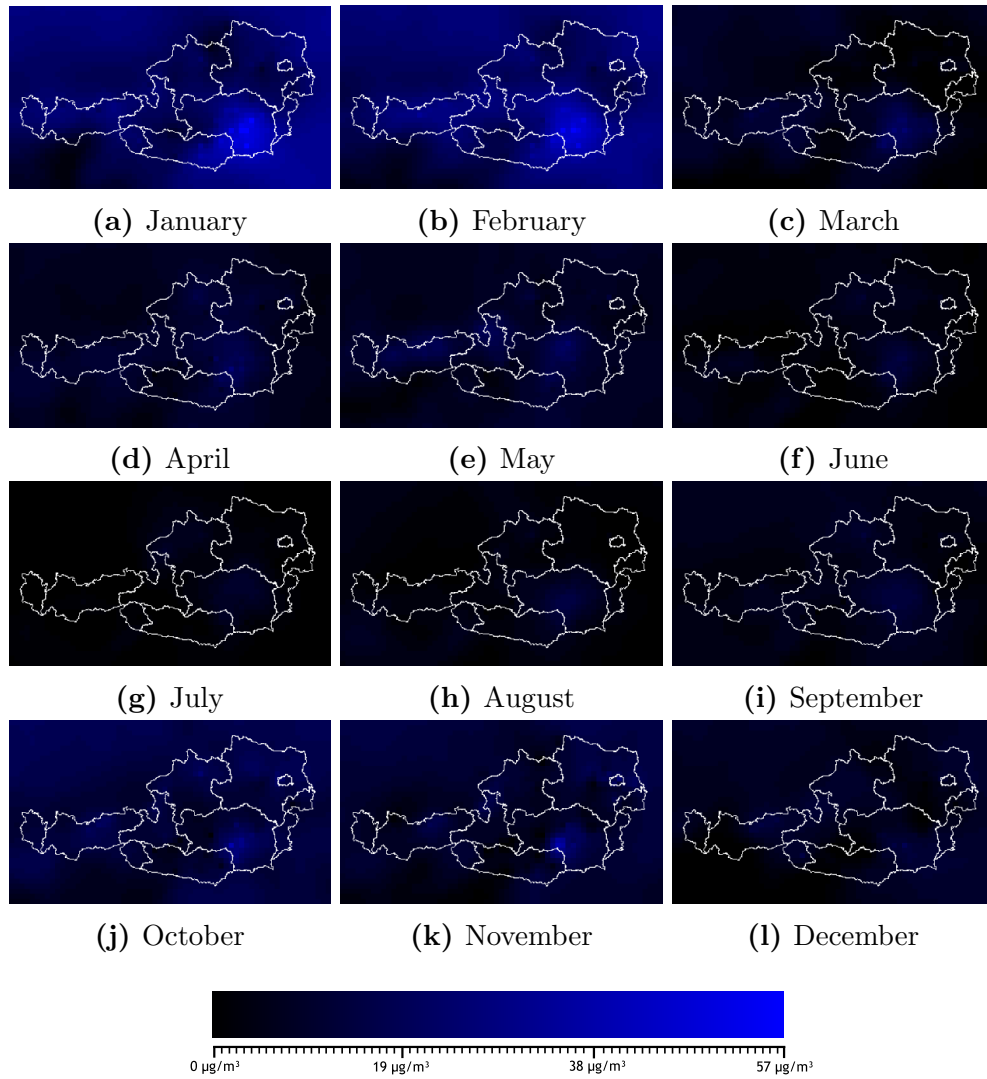
Fig. 4.24 – Monthly averages of PM_{10} estimates over Austria collected from raw daily maps via WCPS Web analysis.

Chapter 5

Conclusions

Can space-based MODIS AOT observations be used in regulatory applications for air quality determinations? This whole thesis revolved on this question, trying to get the scientific community closer to a well-aware and legitimate answer.

The increased role of air quality models for complex, large-scale environmental characterization brought high anticipation on the remotely sensed imagery, and a vast and rapidly increasing amount of scientific works have been published on the topic in recent years.

In the literature there are still varying opinions about the value of satellite observations not only for air quality management, but even for enhancing the spatial and temporal coverage of surface-based measurements. Some even point out the inherent important limitations of aerosol retrievals from top of the atmosphere that would prevent any valuable contribution of AOT. Despite that, remote-sensing is an integral part of several systems of observations and models to address air quality issues, across the world.

This work focused its attention to the prediction of air pollution at locations with no fixed ground monitoring stations. Large availability of data segments of PM_{10} from Emilia Romagna (Italy) and Austria air quality networks inevitably constrained the analysis over these two regions, the former being a notorious critically polluted area, the latter being an extreme case for particles prediction, due to highly rugged topography with high presence of snow and cloud covers.

Availability of years of polar-orbiting MODIS-derived spectral aerosols granules over Europe offered the opportunity to investigate the complex relationship between top-of-atmosphere columnar aerosols loadings and surface dry-mass particulate matter and use it to predict PM at unobserved locations (gap-filling).

While satellite observations can provide valuable knowledge to concentration distribution with long-term records of data (seasonal to yearly), the need for fine-grained monitoring in both time and space especially for urban areas where high peaks of pollution are observed, narrowed down the resolution of our analysis to the single day. The availability of increased-resolution MODIS spectral data (1×1 km^2) from the PM-MAPPER software gave the possibility to analyze the problem at the small scales.

Geostatistical filling of missing values over 2D geographical areas was implemented by means of techniques from the *kriging* estimators suite, which allow for simple univariate to more advanced multivariate interpolations with minimization of the statistical model error.

Kriging represented an optimal trade-off between requirements of complexity, implementation learning curve, hardware costs and FOSS software implementations. Although its applicability highly depends on the geographic area of analysis, and consequently no universal models can be effectively proposed, kriging was chosen for its relative simplicity of implementation through high-level programming languages, low CPU burdens and valuable

predicting power.

In parallel to the modelling research work for daily gap-filling of PM_{10}, efforts were put for the management of Web-based GIS access and on-line processing of the model inputs and outputs. A Web interface (MEA-PM) was implemented in the context of the *SENSORER* project (SENSORER Project, 2010) for the visualization of archives of spaceborne raster and vectorial geo-data of air quality, with custom temporal intervals and spatial area of analysis.

Additionally, in the context of the European *EarthServer* project (The Earth-Server Initiative, 2011), Array DBMS technology was used for a more flexible and scalable access to raster-based geo-images. OGC standard protocols were used and actively shaped for the processing of N-dimensional datasets in a spatiotemporal GIS domain. In the Model Web, and particularly in the scope of air quality modelling, online algebra capabilities on rasters give the chance to compute thresholds exceedance maps with custom intervals of confidence, with no duplication of source data. Interconnected standard-compliant services are in general key assets towards interoperable, intercomparable Web-based applications for Earth observation.

A preliminary mandatory validation process of the AOT maps at new increased resolution from PM MAPPER which was successfully achieved via comparison with temporal segments of measures from uplooking photometers of the AERONET network. A first PM_{10} estimator was then implemented over Emilia Romagna (Italy) with the multivariate cokriging technique, which can model covariances between variables which i) are not necessarily colocated, and ii) are not necessarily known at each prediction location in the output grid.

This seemed the best option for the usability of spaceborne AOT maps, notoriously suffering from their clear-sky conditions requirements. Some fundamental problems however arose: the connection between AOT and PM_{10}

was often not easily caught by the cross-variogram, minimizing the impact of any additional information from satellite on many days in the analysis; secondly the strong constraints on the linear coregionalization of the cross and direct variogram models were shifting away the fitted functions from the experimental observations. Probably these reasons prevented an advantageous use of MODIS data which could justify the statistical modelling with respect to other faster and simpler mechanical predictors (like an inverse distance estimation).

After discarding the cokriging estimator, the more widely used kriging with external drift (KED) technique was chosen as seemingly more prone to raster inputs and nominally as powerful as cokriging can be. A second test case was selected over the Austrian region. Over this region available meteorological forecasts were used to help translating the AOT values into particulate matter information.

An important requirements of KED is that the drift — a multivariate regression surface — must be known at every single output location. Being AOT necessarily amongst the independent variables in the model, it must be ubiquitous, and that force some intermediate interpolation step in order to achieve this. This meant the exclusion AOT data from many days of the analysis because of lack of a sufficient number of pixels.

For this second test case the cross-validation scores showed however a more significant improvement in the spatial prediction of PM_{10}. Despite this, the high unavailability of valid pixels of AOT over Austria could only offer a small percentage of predictions which effectively made use of AOT data. Intensive intermediate gap-filling of AOT was adding further large uncertainty. When sufficient data were available, the role of AOT in the regression model was not very relevant when compared to the role played by the meteorological fields. The study showed that pressure was instead a much more important indicator of particulate matter, at least for the Austrian specific case.

Although daily predictions with daily ad-hoc models were keeping into account the (high) temporal variability of air emissions, they did not account for their interactions. In the third approach implemented the knowledge of temporal memory was included into the geostatistical predictor. After grouping all the input data monthly, variogram analysis on the temporal axis was additionally carried out, building up a 3D model though a separable covariance model.

A direct comparison of the developed KED interpolator was attempted with and without temporal modelling. The addition of data from previous days was unable to increase the capability to predict PM at the ground level. Moreover the days with higher percentage of AOT pixels did not affect the performance. Presumably, the uncertainty in the input data was translated into noise as more datasets where grouped together for prediction. In many cases, no significant temporal memory of PM_{10} levels was measured, even within two consecutive days.

Overall, the contribution of the satellite imagery of AOT for the tested applications did not yield highly convincing results in any of the implemented models.

Kriging estimators can ensure optimal interpolation with geostatistical underlying modelling of the available datasets, but still more sophisticated stochastic models are available, which could better extract the overlapping information between independent variable and covariates. Despite this, a lot of side analysis showed a weak connection between the observations from top of atmosphere and the ground monitoring assessments, even with the bridging of meteorological maps of several key fields like boundary layer height, humidity, pressure and wind. This can either mean that:

- the quality and availability of aerosols data were not high enough to be valuable for air quality predictions;

- the atmospheric profiles of the analysed regions were so complex that TOA aerosols could not be linearly converted to surface masses without vertical profiles;

- the uncertainty in the atmospheric and meteorological inputs was too high for reliable surface PM assessments;

- the variety of different spatial and temporal supports of the involved datasets made them hardly work together into a unique estimator, and more refined data fusion techniques might be needed;

- there was an insufficient temporal resolution of available ground/satellite matches compared to the variability of the fine particles that can be high also during the course of a single day;

- there was an insufficient spatial resolution of the raster-based datasets, so that even the averaging over 1×1 km^2 can still be too coarse for comparison with the punctual PM measurements, whose weight can change even at short distances ($\sim$100 meters).

While the reason(s) behind the unconvincing performances of the proposed models can only be listed, with no absolute certainty of the role of each, several paths forward in the research can be suggested.

Spaceborne AOT (τ) products have a relatively significant uncertainty by nature ($\pm 0.05 \pm 0.15\tau$ for the 0.55µm MODIS channel over land) and subsequent AOT interpolation stages are probably causing a huge increase in the overall uncertainty itself. It is suggested then to investigate on geostatistical methods which do *not* require ubiquitous availability of covariates of the dependent PM variable. Among these, cokriging with linear coregionalization unfortunately revealed some inherent problems in modelling the input data and some experts deem it is not a good option when handling raster-based data.

If there is the chance to reliably proxy the columnar aerosols to surface-level optical depths, e.g. by means of LIDAR-based vertical profiles, then probably cokriging can work better, although sophisticated non-linear coregionalization techniques should be preferred.

Due to the (usually) quick fluctuations of the fine atmospheric particles, the resolution of a polar-orbiting sensor might not be enough at all, although MODIS can provide daily overpasses almost throughout the world. For air quality monitoring, probably a more frequent input of satellite images is recommended. Geostationary satellite data can be averaged to hourly or daily values because of the many observations made for each point in the ground, and are the only ones who can provide detailed insight into the evolution and extent of air pollution. By 2015 the new NOAA series of GOES-R satellites will be launched, providing MODIS-like channels and retrievals each 5—30 min.

Even with proper spatial and temporal resolutions, the AOT as a measure for mass concentrations has skill in some regions and less in others. The need for a reliable physical model to invert the multispectral reflectances is challenging in the case of aerosols since its intrinsic properties are not constant due to the different composition, sizes and hygroscopicity.

Furthermore, even with good input datasets and stable aerosols intrinsic properties, the significant limitation of clouds, especially in the cold season at mid latitudes or during rain months in the tropics, cannot be overcome.

In addition to clear-sky constraints, the extreme reflectivities of bright surfaces (like with snow or deserts) are a further element that can significantly reduce availability of retrieval, like it was directly experienced in the models over Austria.

Surely, a combination of several sources of data is the only way to yield accurate predictions for the air quality system; satellite-based aerosols re-

trievals still have a dominant uncertainty, which is higher when translated into ground PM_{10} and for now remote sensing might be used to catch only very significant exceedances with statistical confidence, and this is still not sufficient for regulatory use.

Unique values of satellite measurements are surely event identification, aerosols transport and atmospheric composition determination (also far from surface); they can fill the gaps where no ground station is available and provide daily maps of data that can feed and support models with auxiliary information. Although the current lack of highly accurate precision in the statistical and physical models that use satellite imagery is not yet enough to drive air quality policies, remote sensing will certainly need to be considered for the cause.

Bibliography

Aiordăchioaie, A. and Baumann, P. (2010). PetaScope: An open-source implementation of the OGC WCS geo service standards suite. In *Scientific and Statistical Database Management*, pages 160–168. Springer. 56

Armstrong, M. and Jabin, R. (1981). Variogram models must be positive-definite. *Mathematical Geology*, 13(5):455–459. 47

ARPA Emilia Romagna (1995). Qualità dell'aria. `http://www.arpa.emr.it/aria/index.asp`. 29

Baumann, P. (2010). The OGC web coverage processing service (WCPS) standard. *Geoinformatica*, 14(4):447–479. 59

Baumann, P. (2011). Boosting scalability of OGC standards on massive data sets through database technology. 56

Baumann, P., Dehmel, A., Furtado, P., Ritsch, R., and Widmann, N. (1998). The multidimensional database system rasdaman. In *ACM SIGMOD Record*, volume 27, pages 575–577. ACM. 2

Biggar, S., Gellman, D., and Slater, P. (1990). Improved evaluation of optical depth components from langley plot data. *Remote Sensing of Environment*, 32(2-3):91–101. 12

Bock, M., Bohner, J., Conrad, O., Kothe, R., and Ringeler, A. (2008). SAGA: System for the automated geoscientific analysis. *Dept. of Physical Geography, Hamburg, Germany. URL //(last verified 19 April 2009).* 2

Brauer, M., Hoek, G., van Vliet, P., Meliefste, K., Fischer, P., Gehring, U., Heinrich, J., Cyrys, J., Bellander, T., Lewne, M., et al. (2003). Estimating long-term average particulate air pollution concentrations: application of traffic indicators and geographic information systems. *Epidemiology*, 14(2):228–239. 37

Breslow, L. (2002). Encyclopedia of Public Health. New York: Gale Group. 9

Caldeweyher, D. (2011). Open source GIS: a GRASS GIS approach. The international series in engineering and computer science. *International Journal of Geographical Information Science*, 25(2):330–331. 2

Chu, D., Kaufman, Y., Zibordi, G., Chern, J., Mao, J., Li, C., and Holben, B. (2003). Global monitoring of air pollution over land from the earth observing system-terra moderate resolution imaging spectroradiometer (MODIS). *Journal of Geophysical Research*, 108(D21):4661. 38

Cressie, N. (1985). Fitting variogram models by weighted least squares. *Mathematical geology*, 17(5):563–586. 47

Cressie, N. and Hawkins, D. (1980). Robust estimation of the variogram: I. *Mathematical geology*, 12(2):115–125. 79

Cressie, N. and Wikle, C. (1998). The variance-based cross-variogram: you can add apples and oranges. *Mathematical Geology*, 30(7):789–799. 49

Davis, C., Bunker, S., and Mutschlecner, J. (1984). Atmospheric transport models for complex terrain. *Journal of climate and applied meteorology*, 23(2):235–238. 37

de Kassteele, J. V. and Velders, G. J. (2006). Uncertainty assessment of local concentrations derived from error-in-variable external drift kriging and its relationship to the 2010 air quality standard. *Atmospheric Environment*, 40(14):2583 – 2595. 41

Denby, B., Schaap, M., Segers, A., Builtjes, P., and Horálek, J. (2008). Comparison of two data assimilation methods for assessing PM_{10} exceedances on the European scale. *Atmospheric Environment*, 42(30):7122–7134. 41

Diggle, P., Tawn, J., and Moyeed, R. (2002). Model-based geostatistics. *Journal of the Royal Statistical Society: Series C (Applied Statistics)*, 47(3):299–350. 48

Dockery, D., Pope, C., Xu, X., Spengler, J., Ware, J., Fay, M., Ferris Jr, B., and Speizer, F. (1993). An association between air pollution and mortality in six US cities. *New England journal of medicine*, 329(24):1753–1759. 16

Emili, E., Popp, C., Petitta, M., Riffler, M., Wunderle, S., and Zebisch, M. (2010). PM_{10} remote sensing from geostationary SEVIRI and polar-orbiting MODIS sensors over the complex terrain of the European Alpine region. *Remote sensing of environment*, 114(11):2485–2499. 40

Emili, E., Popp, C., Wunderle, S., Zebisch, M., and Petitta, M. (2011). Mapping particulate matter in alpine regions with satellite and ground-based measurements: An exploratory study for data assimilation. *Atmospheric Environment*. 40

Engel-Cox, J., Holloman, C., Coutant, B., and Hoff, R. (2004). Qualitative and quantitative evaluation of MODIS satellite sensor data for regional and urban scale air quality. *Atmospheric Environment*, 38(16):2495–2509. 12, 38

European Commission (2012). Air Quality — Existing Legislation. http://ec.europa.eu/environment/air/quality/legislation/existing_leg.htm. Accessed on September 25, 2012. 17

European Environment Agency (EEA) and European Commission Joint Research Centre (JRC) (2008). Forum for AIR quality MODelling in Europe (FAIRMODE). http://fairmode.ew.eea.europa.eu/. Accessed on September 25, 2012. 17

Ezzati, M., Lopez, A., Rodgers, A., and Murray, C. (2004). *Comparative quantification of health risks: global and regional burden of diseases attributable to selected major risk factors*, volume 1. World Health Organization. 17

Faraway, J. (2002). Practical regression and ANOVA using R. 83

Fassò, A., Finazzi, F., and D'Ariano, C. (2009). Integrating satellite and ground level data for air quality monitoring and dynamical mapping. http://hdl.handle.net/10446/954. 40

Garcia, V., Kondragunta, S., Holland, D., Dimmick, F., Boothe, V., Szykman, J., Chu, A., Kittaka, C., Al-Saadi, J., Engel-Cox, J., et al. (2006). Integration of satellite, modeled, and ground based aerosol data for use in air quality and public health applications. In *AGU Spring Meeting Abstracts*, volume 1, page 06. 40

Genton, M. (1998). Highly robust variogram estimation. *Mathematical Geology*, 30(2):213–221. 43

Gotway, C. and Young, L. (2002). Combining incompatible spatial data. *Journal of the American Statistical Association*, 97(458):632–648. 53

Gräler, B., Gerharz, L., and Pebesma, E. (2012). Spatio-temporal analysis and interpolation of PM_{10} measurements in Europe. Technical report, ETC ACM Technical Paper 2011 10. 53

Grell, G., Dudhia, J., Stauffer, D., et al. (1994). A description of the fifth-generation Penn State/NCAR mesoscale model (MM5). 37

Gupta, P. and Christopher, S. (2009a). Particulate matter air quality assessment using integrated surface, satellite, and meteorological products: 2. A neural network approach. *Journal of geophysical research*, 114(D20):D20205. 40

Gupta, P. and Christopher, S. (2009b). Particulate matter air quality assessment using integrated surface, satellite, and meteorological prod-

ucts: Mutliple regression approach. *Journal of geophysical research*, 114(D14):D14205. 15

Gupta, P., Christopher, S., Box, M., and Box, G. (2007). Multi year satellite remote sensing of particulate matter air quality over Sydney, Australia. *International Journal of Remote Sensing*, 28(20):4483–4498. 38

Gupta, P., Christopher, S., et al. (2008). Seven year particulate matter air quality assessment from surface and satellite measurements. *Atmospheric Chemistry and Physics Discussions*, 8(1):327–365. 38

Gupta, P., Christopher, S., Wang, J., Gehrig, R., Lee, Y., and Kumar, N. (2006). Satellite remote sensing of particulate matter and air quality assessment over global cities. *Atmospheric Environment*, 40(30):5880–5892. 12, 38

Hänel, G. (1976). The properties of atmospheric aerosol particles as functions of the relative humidity at thermodynamic equilibrium with the surrounding moist air. *Adv. Geophys*, 19(1):73–188. 92

Hansen, J. and Travis, L. (1974). Light scattering in planetary atmospheres. *Space Science Reviews*, 16(4):527–610. 14

Hengl, T. (2009). *A practical guide to geostatistical mapping.* Hengl. 52

Hengl, T., Heuvelink, G., Perčec Tadić, M., and Pebesma, E. (2012). Spatio-temporal prediction of daily temperatures using time-series of MODIS LST images. *Theoretical and applied climatology*, 107(1):265–277. 54

Hengl, T., Heuvelink, G., and Stein, A. (2003). Comparison of kriging with external drift and regression-kriging. *Technical note, ITC.* 51

Hengl, T., Heuvelink, G., and Stein, A. (2004). A generic framework for spatial prediction of soil variables based on regression-kriging. *Geoderma*, 120(1):75–93. 52

Hidy, G., Brook, J., Chow, J., Green, M., Husar, R., Lee, C., Scheffe, R., Swanson, A., and Watson, J. (2009). Remote sensing of particulate

pollution from space: Have we reached the promised land? *Journal of the Air & Waste Management Association*, 59(10):1130–1139. 9

Hoff, R. and Christopher, S. (2009). Remote sensing of particulate pollution from space: have we reached the promised land. *J. Air & Waste Manage. Assoc*, 59:645–675. 5, 41

Hsu, N., Tsay, S., King, M., and Herman, J. (2004). Aerosol properties over bright-reflecting source regions. *Geoscience and Remote Sensing, IEEE Transactions on*, 42(3):557–569. 25

Hsu, N., Tsay, S., King, M., and Herman, J. (2006). Deep blue retrievals of Asian aerosol properties during ACE-Asia. *Geoscience and Remote Sensing, IEEE Transactions on*, 44(11):3180–3195. 25

HUANG, B., Gumley, L., Strabala, K., Li, J., Weisz, E., Rink, T., Baggett, K., Davies, J., Smith, W., and Dodge, J. (2004). International MODIS and Airs Processing Package (IMAPP). *Bulletin of the American Meteorological Society*, 85(2):159–161. 25

Hutchison, K. (2003). Applications of MODIS satellite data and products for monitoring air quality in the state of Texas. *Atmospheric Environment*, 37(17):2403–2412. 39

Hutchison, K., Faruqui, S., and Smith, S. (2008). Improving correlations between MODIS aerosol optical thickness and ground-based $PM_{2.5}$ observations through 3D spatial analyses. *Atmospheric Environment*, 42(3):530–543. 39

Hutchison, K., Smith, S., and Faruqui, S. (2004). The use of MODIS data and aerosol products for air quality prediction. *Atmospheric Environment*, 38(30):5057–5070. 39

Hutchison, K., Smith, S., and Faruqui, S. (2005). Correlating MODIS aerosol optical thickness data with ground-based $PM_{2.5}$ observations across Texas for use in a real-time air quality prediction system. *Atmospheric Environment*, 39(37):7190–7203. 39

Ichoku, C., Chu, D., Mattoo, S., Kaufman, Y., Remer, L., Tanré, D., Slutsker, I., and Holben, B. (2002). A spatio-temporal approach for global validation and analysis of MODIS aerosol products. *Geophysical Research Letters*, 29(12):8006. 65, 76

Ignatov, A., Minnis, P., Loeb, N., Wielicki, B., Miller, W., Sun-Mack, S., Tanré, D., Remer, L., Laszlo, I., and Geier, E. (2005). Two MODIS aerosol products over ocean on the Terra and Aqua CERES SSF datasets. *Journal of the atmospheric sciences*, 62(4):1008–1031. 22

Isaaks, E. and Srivastava, R. (1989). *An introduction to applied geostatistics*. Oxford University Press, New York. 48

Jerrett, M., Arain, A., Kanaroglou, P., Beckerman, B., Potoglou, D., Sahsuvaroglu, T., Morrison, J., and Giovis, C. (2004). A review and evaluation of intraurban air pollution exposure models. *Journal of Exposure Science and Environmental Epidemiology*, 15(2):185–204. 36, 37, 41, 64

Jerrett, M., Burnett, R., Ma, R., Pope III, C., Krewski, D., Newbold, K., Thurston, G., Shi, Y., Finkelstein, N., Calle, E., et al. (2005). Spatial analysis of air pollution and mortality in Los Angeles. *Epidemiology*, 16(6):727–736. 16

Kacenelenbogen, M., Léon, J., Chiapello, I., Tanré, D., et al. (2006). Characterization of aerosol pollution events in France using ground-based and POLDER-2 satellite data. *Atmospheric Chemistry and Physics*, 6(12). 38

Katsouyanni, K., Touloumi, G., Samoli, E., Gryparis, A., Le Tertre, A., Monopolis, Y., Rossi, G., Zmirou, D., Ballester, F., Boumghar, A., et al. (2001). Confounding and effect modification in the short-term effects of ambient particles on total mortality: results from 29 European cities within the APHEA2 project. *Epidemiology*, 12(5):521–531. 17

Kloog, I., Koutrakis, P., Coull, B., Lee, H., and Schwartz, J. (2011). Assessing temporally and spatially resolved $PM_{2.5}$ exposures for epidemiological

studies using satellite aerosol optical depth measurements. *Atmospheric Environment*, 45(35):6267–6275. 41

Knotters, M., Brus, D., and Oude Voshaar, J. (1995). A comparison of kriging, co-kriging and kriging combined with regression for spatial interpolation of horizon depth with censored observations. *Geoderma*, 67(3):227–246. 51

Koelemeijer, R., Homan, C., and Matthijsen, J. (2006). Comparison of spatial and temporal variations of aerosol optical thickness and particulate matter over Europe. *Atmospheric Environment*, 40(27):5304–5315. 13, 14, 92

Kulkarni, P., Baron, P., and Willeke, K. (2011). *Aerosol measurement: principles, techniques, and applications.* Wiley. 9

Kumar, N. (2010). What can affect AOD-PM$_{2.5}$ association? *Environmental health perspectives*, 118(3):A109. 41

Langholz, B., Ebi, K., Thomas, D., Peters, J., and London, S. (2002). Traffic density and the risk of childhood leukemia in a Los Angeles case-control study. *Annals of epidemiology*, 12(7):482–487. 36

Lebret, E., Briggs, D., Van Reeuwijk, H., Fischer, P., Smallbone, K., Harssema, H., Kriz, B., Gorynski, P., and Elliott, P. (2000). Small area variations in ambient NO$_2$ concentrations in four European areas. *Atmospheric Environment*, 34(2):177–185. 37

Levy, R., Remer, L., Tanré, D., Mattoo, S., and Kaufman, Y. (2009). Algorithm for remote sensing of tropospheric aerosol over dark targets from MODIS: Collections 005 and 051: Revision 2, February 2009, MODIS algorithm theoretical basis document. *MODIS Algorithm Theoretical Basis Document.* 1, 23

Lippmann, M. and Albert, R. (1969). The effect of particle size on the regional deposition of inhaled aerosols in the human respiratory tract. *American Industrial Hygiene Association Journal*, 30(3):257–275. 11

Liu, L., Delfino, R., and Koutrakis, P. (1997). Ozone exposure assessment in a southern California community. *Environmental health perspectives*, 105(1):58. 36

Liu, Y., Franklin, M., Kahn, R., and Koutrakis, P. (2007a). Using aerosol optical thickness to predict ground-level PM$_{2.5}$ concentrations in the St. Louis area: a comparison between MISR and MODIS. *Remote sensing of environment*, 107(1-2):33–44. 4

Liu, Y., Koutrakis, P., Kahn, R., Turquety, S., and Yantosca, R. (2007b). Estimating fine particulate matter component concentrations and size distributions using satellite-retrieved fractional aerosol optical depth: part 2a case study. *Journal of the Air & Waste Management Association*, 57(11):1360–1369. 4, 39

Liu, Y., Paciorek, C. J., and Koutrakis, P. (2009). Estimating regional spatial and temporal variability of PM$_{2.5}$ concentrations using satellite data, meteorology, and land use information. *Environmental health perspectives*, 117(6):886. 40, 55

Maheswaran, R. and Elliott, P. (2003). Stroke mortality associated with living near main roads in England and Wales a geographical study. *Stroke*, 34(12):2776–2780. 36

Matheron, G. (1969). *Le krigeage universel*. École nationale supérieure des mines de Paris. 43

MEEO Srl (2009). PM MAPPER system description, issue 1.1. Internal report, unpublished. If requested, can be delivered upon agreement from the sponsor of the project. 26

Misev, D., Rusu, M., and Baumann, P. (2012). A semantic resolver for coordinate reference systems. *Web and Wireless Geographical Information Systems*, pages 47–56. 59

Mukala, K., Alm, S., Tiittanen, P., En, R., Jantunen, M., and Pekkanen, J. (2000). Nitrogen dioxide exposure assessment and cough among

preschool children. *Archives of Environmental Health: An International Journal*, 55(6):431–438. 36

Mulugeta, G. (1996). Manual and automated interpolation of climatic and geomorphic statistical surfaces: An evaluation. *Annals of the Association of American Geographers*, 86(2):324–342. 43

Myers, D. (1982). Matrix formulation of co-kriging. *Mathematical Geology*, 14(3):249–257. 50

NASA (1993). AERONET Aerosol Robotic Network. http://aeronet.gsfc.nasa.gov/. 21

NASA (1999). MODIS. http://modis.gsfc.nasa.gov/. 25

NASA (2008). J-track 3-d satellite tracking. http://science.nasa.gov/realtime/jtrack/3d/JTrack3D.html/. Accessed on September 13, 2012. 3

NASA Earth Observatory (2010). Aerosols: Tiny particles, big impact. http://earthobservatory.nasa.gov/Features/Aerosols/. Accessed on September 14, 2012. 10

Nel, A. (2005). Air pollution-related illness: effects of particles. *Science*, 308(5723):804–806. 11

Nguyen, T. (2012). *Downscaling Aerosol Optical Thickness from Satellite Observations: Physics and Machine Learning Approaches*. PhD thesis, Università degli Studi di Ferrara. 25

Nguyen, T., Bottoni, M., and Mantovani, S. (2010a). PM MAPPER: an air quality monitoring system with fine spatial resolution product and integrated surface information. In *Hyperspectral Workshop. Frascati, Italy*. 25, 64

Nguyen, T., Mantovani, S., and Bottoni, M. (2010b). Estimation of aerosol and air quality fields with PM MAPPER - an optical multispectral data

processing package. In *ISPRS Commission VII Symposium, Vienna, Austria.* 25

NOAA – Earth Observation Group (1970). Nighttime lights time series. http://www.ngdc.noaa.gov/dmsp/downloadV4composites.html. 34

OGC (2007). OGC Geography Markup Language (GML) Encoding Standard. 59

OGC (2009). OGC Web Coverage Processing Service (WCPS) Language Interface Standard. 59

OGC (2010). OGC Web Coverage Service (WCS) - Core . 57

Oosthoek, J., Flahaut, J., Rossi, A., Baumann, P., Misev, D., Campalani, P., and Unnithan, V. (2013). PlanetServer: Innovative approaches for the online analysis of hyperspectral satellite data from Mars. *Advances in Space Research.* To appear. 59

Paciorek, C., Liu, Y., Moreno-Macias, H., and Kondragunta, S. (2008). Spatiotemporal associations between GOES aerosol optical depth retrievals and ground-level $PM_{2.5}$. *Environmental science & technology*, 42(15):5800–5806. 5, 39

Pearce, J., Rathbun, S., Aguilar-Villalobos, M., and Naeher, L. (2009). Characterizing the spatiotemporal variability of $PM_{2.5}$ in Cusco, Peru using kriging with external drift. *Atmospheric Environment*, 43(12):2060–2069. 41

Pebesma, E. (2012). *spacetime: classes and methods for spatio-temporal data.* R package version 0.8-0. 55

Pebesma, E., Cornford, D., Dubois, G., Heuvelink, G., Hristopoulos, D., Pilz, J., Stoehlker, U., and Skoien, J. (2009). INTAMAP: an interoperable automated interpolation web service. *Proceedings of StatGIS09: GeoInformatics for Environmental Surveillance, Milos, Greece*, pages 17–19. 61

Pebesma, E. J. (2004). Multivariable geostatistics in S: the gstat package. *Computers & Geosciences*, 30:683–691. 42, 48

Pelletier, B., Santer, R., and Vidot, J. (2007). Retrieving of particulate matter from optical measurements: A semiparametric approach. *Journal of geophysical research*, 112(D6):D06208. 13

Pope III, C., Burnett, R., Thun, M., Calle, E., Krewski, D., Ito, K., and Thurston, G. (2002). Lung cancer, cardiopulmonary mortality, and long-term exposure to fine particulate air pollution. *JAMA: the journal of the American Medical Association*, 287(9):1132–1141. 16

Popp, C., Hauser, A., Foppa, N., and Wunderle, S. (2007). Remote sensing of aerosol optical depth over central Europe from MSG-SEVIRI data and accuracy assessment with ground-based AERONET measurements. *Journal of Geophysical Research*, 112(D24):D24S11. 5

Porter, P., Szykman, J., Rao, S., Gégo, E., Hogrefe, C., and Garcia, V. (2012). Integrating $PM_{2.5}$ observations, model estimates and satellite signals for the Eastern United States by projection onto latent structures. *Air Pollution Modeling and its Application XXI*, pages 353–358. 40

Potoglou, D. and Kanaroglou, P. (2005). Carbon monoxide emissions from passenger vehicles: predictive mapping with an application to Hamilton, Canada. *Transportation Research Part D: Transport and Environment*, 10(2):97–109. 37

Prasad, A. and Singh, R. (2007). Comparison of MISR-MODIS aerosol optical depth over the Indo-Gangetic basin during the winter and summer seasons (2000–2005). *Remote Sensing of Environment*, 107(1):109–119. 70

R Development Core Team (2011). *R: A Language and Environment for Statistical Computing*. R Foundation for Statistical Computing, Vienna, Austria. ISBN 3-900051-07-0. 2

Randriamiarisoa, H., Chazette, P., Couvert, P., Sanak, J., Mégie, G., et al. (2006). Relative humidity impact on aerosol parameters in a Paris suburban area. *Atmospheric Chemistry and Physics*, 6(5). 92

RASter DAta MANager (rasdaman) (2009). `www.rasdaman.org`. Accessed on October 12, 2012. 56

Remer, L., Kaufman, Y., Tanré, D., Mattoo, S., Chu, D., Martins, J., Li, R., Ichoku, C., Levy, R., Kleidman, R., et al. (2005). The MODIS aerosol algorithm, products, and validation. *Journal of the Atmospheric Sciences*, 62(4):947–973. 2, 24

Remer, L., Tanré, D., and Kaufman, Y. (2006). Algorithm for remote sensing of tropospheric aerosol from MODIS: collection 5. MODIS algorithm theoretical basis document. 25

Ribeiro Jr, P. J. and Diggle, P. J. (2001). geoR: a package for geostatistical analysis. *R-NEWS*, 1(2):14–18. ISSN 1609-3631. 42

Robert J. Hijmans & Jacob van Etten (2012). *raster: Geographic analysis and modeling with raster data.* R package version 2.0-12. 58

Rossiter, D. (2007). Technical note: Co-kriging with the gstat package of the R environment for statistical computing. 50

Samet, J., Zeger, S., Dominici, F., Curriero, F., Coursac, I., Dockery, D., Schwartz, J., and Zanobetti, A. (2000). The national morbidity, mortality, and air pollution study. *Part II: morbidity and mortality from air pollution in the United States Res Rep Health Eff Inst*, 94(pt 2):5–79. 17

Satheesh, S., Torres, O., Remer, L., Babu, S., Vinoj, V., Eck, T., Kleidman, R., and Holben, B. (2009). Improved assessment of aerosol absorption using OMI-MODIS joint retrieval. *J. Geophys. Res*, 114:D05209. 4

Scire, J., Robe, F., Fernau, M., and Yamartino, R. (2000). A user's guide for the CALMET meteorological model. *Earth Tech, USA*. 37

SENSORER Project (2010). http://www.meeo.it/index.php?action=view_gallery&id=21&module=imagegallerymodule&src=@random483811eaaa25asection=2&lang=e. Accessed on October 12, 2012. 73, 107

Slanina, S. (1997). *Biosphere-Atmosphere Exchange of Pollutants and Trace Substances: Experimental and Theoretical Studies of Biogenic Emissions and Pollutant Deposition*, volume 4. Springer. 11

Stein, A. and Corsten, L. (1991). Universal kriging and cokriging as a regression procedure. *Biometrics*, pages 575–587. 49

Stein, M. L. (1999). *Interpolation of spatial data: some theory for kriging*. Springer Verlag. 87

Tanré, D., Kaufman, Y., Herman, M., and Mattoo, S. (1997). Remote sensing of aerosol properties over oceans using the MODIS/EOS spectral radiances. *J. Geophys. Res*, 102(D14):16. 23

The CGAR Consortium for Spatial Information (1999). SRTM digital elevation data. http://srtm.csi.cgiar.org/. 32

The EarthServer Initiative (2011). http://www.earthserver.eu/. Accessed on January 21, 2013. 107

The World Data Center For Remote Sensing Of The Atmosphere (2002). SCIAMACHY mission. http://wdc.dlr.de/sensors/. Accessed on September 13, 2012. 4

Thomas, G. and Stamnes, K. (2002). *Radiative transfer in the atmosphere and ocean*. Cambridge Univ Pr. 8

Tie, X., Madronich, S., Walters, S., Edwards, D., Ginoux, P., Mahowald, N., Zhang, R., Lou, C., and Brasseur, G. (2005). Assessment of the global impact of aerosols on tropospheric oxidants. *Journal of Geophysical Research*, 110(D3):D03204. 9

Tsai, T., Jeng, Y., Chu, D., Chen, J., and Chang, S. (2011). Analysis of the relationship between MODIS aerosol optical depth and particulate matter from 2006 to 2008. *Atmospheric Environment*, 45(27):4777–4788. 39

Turner, J. and Allen, D. (2008). Transport of atmospheric fine particulate matter: Part 2 – Findings from recent field programs on the intraurban variability in fine particulate matter. *Journal of the Air & Waste Management Association*, 58(2):196–215. 53

Umweltbundesamt (1999). State of the environment reports. http://www.umweltbundesamt.at/en_ukb. Accessed on October 15, 2012. 30

Van Donkelaar, A., Martin, R., Kahn, R., and Levy, R. (2009). Global climatology of fine particulate matter concentrations estimated from remote-sensed aerosol optical depth. In *AGU Fall Meeting Abstracts*, volume 1, page 07. 15

Van Donkelaar, A., Martin, R., Levy, R., da Silva, A., Krzyzanowski, M., Chubarova, N., Semutnikova, E., and Cohen, A. (2011). Satellite-based estimates of ground-level fine particulate matter during extreme events: A case study of the Moscow fires in 2010. *Atmospheric Environment*, 45(34):6225–6232. 39

Ver Hoef, J. and Barry, R. (1998). Constructing and fitting models for cokriging and multivariable spatial prediction. *Journal of Statistical Planning and Inference*, 69(2):275–294. 48

Wackernagel, H. (1996). Multivariate geostatistics: an introduction with applications. In *International Journal of Rock Mechanics and Mining Sciences and Geomechanics Abstracts*, volume 33, pages 363A–363A. Elsevier. 51

Walker, E., Slørdal, L., Guerreiro, C., Gram, F., and Grønskei, K. (1999). Air pollution exposure monitoring and estimation. Part II. Model evaluation and population exposure. *J. Environ. Monit.*, 1(4):321–326. 37

Wang, J. and Christopher, S. (2003). Intercomparison between satellite-derived aerosol optical thickness and $PM_{2.5}$ mass: Implications for air quality studies. *Geophys. Res. Lett*, 30(21):2095. 12, 38

Wang, Z., Chen, L., Tao, J., Zhang, Y., and Su, L. (2010). Satellite-based estimation of regional particulate matter (PM) in Beijing using vertical-and-RH correcting method. *Remote Sensing of Environment*, 114(1):50–63. 92

Watson, J., Green, M., and Chow, J. (2012). Evaluation of satellite MODIS aerosol optical depth measurements for prediction of $PM_{2.5}$ at Fresno, California. *J. Air & Waste Manage. Assoc.* submitted for publication. 13

Winker, D., Vaughan, M., and Hunt, B. (2006). The CALIPSO mission and initial results from CALIOP. In *Asia-Pacific Remote Sensing Symposium*, pages 640902–640902. International Society for Optics and Photonics. 39

World Health Organization (2006). WHO air quality guidelines for particulate matter, ozone, nitrogen dioxide and sulfur dioxide. Global update 2005, summary of risk assessment. *Geneva: WHO.* 17

Yahi, H., Santer, R., Weill, A., Crepon, M., and Thiria, S. (2011). Exploratory study for estimating atmospheric low level particle pollution based on vertical integrated optical measurements. *Atmospheric Environment*, 45(23):3891–3902. 13

Own work

Baumann, P., Campalani, P., Misev, D., and Yu, J. (2012). Finding my CRS: A systematic way of identifying CRSs. In *ACM SIGSPATIAL*.

Campalani, P., Mantovani, S., Hirtl, M., Caglienzi, M., and Mazzini, G. (2012). Daily spatial prediction of PM_{10} mass concentrations with geostatistics: an Austrian case study. In *Universidad Politecnica de Valencia Editorial*.

Campalani, P., Nguyen, T. N. T., Mantovani, S., Bottoni, M., and Mazzini, G. (2011a). Validation of PM MAPPER aerosol optical thickness retrievals at 1×1 km^2 of spatial resolution. In *Software, Telecommunications and Computer Networks (SoftCOM), 2011 19th International Conference on*. 26

Campalani, P., Nguyen, T. N. T., Mantovani, S., and Mazzini, G. (2011b). On the automatic prediction of PM_{10} with in-situ measurements, satellite AOT retrievals and ancillary data. In *ISSPIT*, pages 93–98.

Campalani, P. and Pasetti, S. (2010a). SENSORER – 0152 project technical note OR2: Mixed data collection. Internal report, unpublished. If requested, can be delivered upon agreement from the sponsor of the project. 29

Campalani, P. and Pasetti, S. (2010b). SENSORER – 0153 project technical note OR2: Ground data validation. Internal report, unpublished. If requested, can be delivered upon agreement from the sponsor of the project.

Campalani, P. and Pasetti, S. (2010c). SENSORER – 0154 project technical note OR2: User interface. Internal report, unpublished. If requested, can be delivered upon agreement from the sponsor of the project.

Natali, S., Beccati, A., D'Elia, S., Veratelli, M., Campalani, P., Folegani, M., and Mantovani, S. (2011). Multitemporal data management and exploitation infrastructure. In *MultiTemp*, Trento.

Submitted work

Campalani, P. and Baumann, P. (2013). A posteriori analysis of model-based maps. Presentation abstract submitted for conference proceedings.

Campalani, P., Beccati, A., and Baumann, P. (2013a). Addressing verbosity in GML 3.3 ReferenceableGrid geometries for practical use cases. Article submitted for conference proceedings.

Campalani, P., Mantovani, S., and Baumann, P. (2013b). Spatio-temporal interactions for daily mapping of PM_{10} with MODIS and meteorological data. Abstract submitted for conference proceedings.

Campalani, P., Misev, D., Beccati, A., and Baumann, P. (2013c). Integration of the temporal dimension for gridded coverages. Article submitted for conference proceedings.